

DEVELOPMENT OF MoSi₂ MATRIX COMPOSITES FOR HIGH
TEMPERATURE STRUCTURAL APPLICATIONS

BY

LINGANG XIAO

A DISSERTATION PRESENTED TO THE GRADUATE SCHOOL
OF UNIVERSITY OF FLORIDA IN PARTIAL FULFILLMENT
OF THE REQUIREMENTS FOR THE DEGREE OF
DOCTOR OF PHILOSOPHY

UNIVERSITY OF FLORIDA

1992

UNIVERSITY OF FLORIDA LIBRARIES

ACKNOWLEDGMENTS

I would like to express my sincerest gratitude to Dr. R. Abbaschian, my supervisory committee chairman, for his invaluable guidance, support and encouragement throughout the research portion of this project, and for his numerous suggestions and corrections during the preparation of this dissertation. I am also thankful to the rest of my committee members, Dr. R. T. DeHoff, Dr. M. J. Kaufman, Dr. J. Mecholsky and Dr. B. V. Sankar, for their encouragement and advice throughout the research of this project. The author would also like to acknowledge the support of this project from the DARPA and ONR through grant N00014-91-J-4075.

I would also like to extend my thanks to my colleagues, Dr. A. B. Gokhale, Dr. Y. S. Kim, Mr. I. H. Hwang and Mr. L. Lu, with whom I had many fruitful discussions on various aspects of this research. Special thanks must also be given to Mr. Wayne Acree for his helpful discussions on electron microscopy analyses. Thanks are also due to Dr. D. E. Clark and Ms. D. C. Folz for helping me to start the sol-gel coating technique.

Finally, I am deeply indebted to my parents for their love and encouragement throughout my entire life, and to my loving wife and daughter for their patience, understanding, inspiration and support during the course of this work.

TABLE OF CONTENTS

	Pages
ACKNOWLEDGMENT	ii
ABSTRACT	v
CHAPTER	
1. INTRODUCTION	1
2. LITERATURE SURVEY	6
2.1 Theoretical Background	6
2.2 Toughening Mechanisms in Brittle Matrix Composites	9
2.3 Ductile Phase Toughening	22
2.4 Physical and Chemical Properties of MoSi ₂ matrix	28
3. EXPERIMENTAL PROCEDURE	31
3.1 Microstructural Characterization and Raw Materials	31
3.2 Fiber and Foil Coating Techniques	33
3.3 Fabrication of MoSi ₂ Matrix Composites	35
3.4 Measurement of Intrinsic Properties of the Ductile Phase	36
3.5 Measurement of Fracture Energy of Matrix/Reinforcement Interface	38
3.6 Measurement of Toughness of the Composites	38
4. RESULTS AND DISCUSSION	41
4.1 Microstructures of the Composites	41
4.1.1 Monolithic MoSi ₂	41
4.1.2 MoSi ₂ /uncoated Nb Interface	44
4.1.3 Chemical Compatibility of Coating Materials with Nb and MoSi ₂	53
4.1.4 Effectiveness of the Inert Coatings as a Diffusion Barrier	55
4.2 Optimization of Coating Processes	61
4.2.1 Coating via Sol-Gel Technique	62
4.2.2 Coating via Physical Vapor Deposition	66
4.2.3 Coating via Hot Dipping and Anodizing Technique	69
4.3 Fracture Energy of the Matrix/Reinforcement Interfaces	74
4.3.1 MoSi ₂ /Uncoated Nb Interface	74

4.3.2 MoSi ₂ /Al ₂ O ₃ coated Nb interface	75
4.3.3 MoSi ₂ /ZrO ₂ coated Nb interface	85
4.4 Interactions between Cracks and Ductile Reinforcements	86
4.4.1 Relation between the External Load and Crack Propagation in MoSi ₂ /Nb composites	88
4.4.2 Behaviors of Cracks at the Interface	94
4.4.3 Fracture Surface Observation on MoSi ₂ Matrix	105
4.5 Flow Behavior of Constrained Niobium	107
4.5.1 Intrinsic Properties of the Processed Nb	110
4.5.2 Failure Mechanism and Related Observation on Constrained Niobium	114
4.5.3 Stress-Displacement Curves of Constrained Niobium	120
4.5.4 Modeling of Flow Behavior of the Constrained Niobium	123
4.5.5 Comparison between the Model and Experiments	128
4.6 Effects of Interface, Size and Orientation of Ductile Phases on Toughness	137
4.6.1 Dual-Effects of the Matrix/Reinforcement Interface on the Toughness of the Composites	137
4.6.2 Effects of Niobium Size on the Toughness	141
4.6.3 Effects of Orientation of Niobium Lamina on the Toughness	146
4.6.4 Stress Analysis of Chevron Notched Specimens of the MoSi ₂ /Nb Laminated Composites	151
4.6.5 Comparison between the Experiments and Analytical Results	156
4.7 Modeling of Ductile Phase Toughening --- Large Scale Bridging	159
4.7.1 Basic Model	160
4.7.2 Computation of the Crack Growth Resistance	163
4.7.3 Typical R-Curve Behavior of Ductile-Phase- Toughened Composites	164
4.7.4 Prediction of the Effects of Matrix/Reinforcement Interface on Toughness	170
4.7.5 Prediction of the Effects of Size of Ductile Phases on Toughness	170
4.7.6 Prediction of the Effects of Intrinsic Properties of Ductile Phases on Toughness	174
4.7.7 Prediction of the Effects of Volume Fraction of Ductile Phases on Toughness	174
4.7.8 Prediction of the Effects of Properties of Matrix on Toughness	177
5. CONCLUSIONS	185
APPENDIX	189
REFERENCES	192
BIOGRAPHICAL SKETCH	204

Abstract of Dissertation Presented to the Graduate School of the University of Florida
in Partial Fulfillment of the Requirements for the Degree of Doctor of Philosophy

DEVELOPMENT OF MoSi₂ MATRIX COMPOSITES FOR HIGH TEMPERATURE
STRUCTURAL APPLICATIONS

By
Lingang Xiao

December 1992

Chairman: Dr. Reza Abbaschian

Major Department: Materials Science and Engineering

Ductile phase toughening of MoSi₂ matrix reinforced with Nb filaments or laminae for high temperature structural applications has been investigated. To improve the high temperature stability of the composites, Al₂O₃ coating between the matrix and reinforcements was identified as an effective diffusion barrier and thermomechanically compatible with both the matrix and the reinforcements. The techniques investigated for producing the Al₂O₃ coating on the surfaces of niobium reinforcements included sol-gel processing, physical vapor deposition, and hot dipping in a molten aluminum followed by anodizing to form alumina. The optimization of these coating techniques was conducted and the results indicated that the best coating was provided with physical vapor deposition, followed by the sol-gel technique.

In order to optimize the ductile phase toughening, the interactions between cracks and ductile reinforcements were examined. The effects of various material parameters, such as size of the ductile phase, bonding strength of the matrix/reinforcement interface, and orientation of the ductile laminae on the toughening were also explored. The experimental results indicated that the ductile phase toughening

in the present system was large-scale bridging in nature; the crack growth resistance increased with size of ductile phases for large initial cracks; ductile-laminae-reinforced composites provided a two-dimensional toughening; and the matrix/reinforcement interface exhibited a dual-effect on the toughness, that is, a strong interface would give rise to a high damage tolerance and low work of fracture, while a weak interface would provide a high work of fracture and low damage tolerance.

Based on the experimental observation, a rigorous analytical model was proposed to describe the large-scale-bridging (LSB) of the ductile phase toughening. The LSB model allowed for the prediction of the typical R-curve behavior of the composites, encompassing the effects of the bonding strength of the matrix/reinforcement interface, the size of ductile phases, and the intrinsic mechanical properties of the reinforcement and matrix. The LSB model, which was found to be consistent with the experimental results, provides a guideline for the design of ductile-phase-toughened composites.

CHAPTER 1 INTRODUCTION

The need to increase the operating temperature of heat engines to improve their efficiency has provided a large impetus in recent years for the development of high temperature structural materials such as carbides, nitrides, aluminides and silicides. These ceramics and intermetallics have very high melting temperatures, high elastic moduli, low densities, and can withstand hostile environments. Their structural application, however, is currently limited by their tendency to fail catastrophically from small surface and/or internal flaws, and by thermal shock.

Accordingly, much effort has been made to improve the toughness of these materials. Two general approaches have received a great deal of attention: (1) increasing toughness through composite approaches (e.g., introduction of a second phase in the form of particles, flakes, whiskers, fibers, or even voids to produce a ceramic matrix composite or intermetallic matrix composite); (2) reducing flaw size and population through improved processing (e.g., elimination of agglomerates, pressure sintering, etc.). Although significant improvements in minimizing strength-degrading defects have been achieved through improved processing in recent years, this approach is reaching its limitation since the critical-sized flaws cannot be eliminated entirely. In contrast, composite approaches have proved to be effective in improving the toughness and have increased the apparent fracture toughness of brittle materials to useful levels (about $20 \text{ MPa.m}^{1/2}$). However, further advances are needed to develop ceramics and intermetallics with the desired level of reliability for structural applications.

It has been established that the mechanisms responsible for composite toughening consist of crack deflection, crack bowing, crack bridging, crack blunting and crack shielding (i.e., phase transformation toughening and microcracking toughening). Among these mechanisms, crack bridging has been shown to be the most effective toughening mechanism in the sense that it could increase the toughness of composites to a useful level and provide such toughening at ambient temperatures as well as at elevated temperatures. Crack bridging is achieved generally by the incorporation of ceramic whiskers or fibers, or ductile fibers or particles. Much exploration has been made in the area of ceramic fiber- or whisker-reinforced composites. For example, SiC whiskers have been used to reinforce alumina [1], mullite[2], silicon nitride [3-6], glass [7,8], magnesia-alumina spinel [9], zirconia [10,11], and mullite-zirconia [12,13]. Continuous SiC fibers have also been used to reinforce silicon carbide [14-17], silicon nitride [18] and glass [19]. One of the most important findings in the brittle-fiber- or whisker-reinforced brittle matrix composites is that a brittle matrix bonded to a brittle reinforcement by a brittle interface results in a tough material, a result defying intuition. Another finding is that the toughness of fiber- or whisker-reinforced composites is flaw-size independent. In contrast, investigation on ductile phase toughening has received relatively less attention than ceramic fiber or whisker toughening. To obtain an optimal ductile phase toughening, it is necessary to consider the following effects on the toughness: (1) matrix/reinforcement interface, (2) morphology of ductile phases, (3) size of ductile phases, and (4) intrinsic mechanical properties of ductile phases. Besides, most of the theories of ductile phase toughening [20-26] are based on fracture mechanics of small-scale bridging which is usually not representative of ductile phase toughening. Therefore, more accurate models (i.e., models of large-scale bridging) are needed to predict the overall mechanical performance of the composite from the properties of the constituents (matrix, reinforcement, interface). Finally, there are often deleterious interactions between

ductile reinforcements and intermetallic matrices during the processing and/or at elevated service temperature. Thus, it is necessary to establish a coating technique to prevent the interactions and maintain the integrity of the reinforcement.

It is the goal of this research to explore ductile phase toughening in brittle matrices for structural applications above 1200°C. Owing to the projected use temperatures, the composites must exhibit adequate mechanical properties--high specific strength, toughness, good thermal shock resistance, creep resistance, fatigue resistance--as well as stability in oxidizing atmospheres. Thus, molybdenum disilicide (MoSi_2) has been chosen as the matrix material in the present study, because of its excellent oxidation resistance, high melting point (2020°C) and relatively low density (6.31 g/cm³). Similarly, the suitable ductile reinforcements are limited to the refractory metals, notably W, Ta, Mo and Nb. Nb is of particular interest because its thermal expansion coefficient is closest to that of MoSi_2 , reducing the potential for matrix cracking upon thermal cycling during processing and in service. The work presented in this dissertation consists of four major elements:

- (1) establishment of a processing technique and the process control parameters for producing a diffusion barrier between the MoSi_2 matrix and Nb reinforcement;
- (2) study of the flow behavior of the constrained Nb and the effects on the toughening;
- (3) investigation of the effects of various material parameters, e.g., size of the ductile phase, bonding strength of the matrix/reinforcement interface, and orientation of the ductile laminae on the toughening;
- (4) development of models of the bridging micromechanics and guidelines for the design of ductile-phase-reinforced composites.

For controlling the matrix/reinforcement interaction, chemical compatibilities of various potential coating materials (mullite, Al_2O_3 , and ZrO_2) with MoSi_2 and Nb were conducted via microstructural and compositional analyses. Based on these

analyses, Al₂O₃ was chosen as the final diffusion barrier coating because it was chemically compatible with both MoSi₂ and Nb plus it also had a thermal expansion coefficient close to those of both the matrix and reinforcement. The techniques used for producing the Al₂O₃ coating on the Nb surfaces included (1) sol-gel processing; (2) physical vapor deposition; (3) hot dipping the reinforcement in molten aluminum, followed by anodizing to form Al₂O₃. The process control parameters for the techniques and the effectiveness of the coatings as a diffusion barrier were evaluated.

Study of the flow behavior of the constrained Nb was conducted using a tensile test on a single Nb lamina imbedded in an MoSi₂ matrix. The effects of the matrix/reinforcement interface, the mechanical properties (yield strength and work hardening rate) and size of the ductile phase on the flow behavior were evaluated. Based on the observations from the tensile tests, an approximate model was proposed which gave insight into the influence of yield strength, work hardening, matrix/reinforcement interfacial bonding strength and size of the ductile reinforcement on the flow behavior. The stress-displacement function developed was used to calculate the bridging stress across the crack surface in the large-scale-bridging model proposed in this study.

The role of the matrix/reinforcement interface in the fracture toughness of MoSi₂/Nb composites was assessed via four-point bend tests on chevron notched specimens. Variation of the interfacial bonding was obtained by depositing different oxide coatings (Al₂O₃ and ZrO₂) or by the development of a reaction product layer between the matrix and reinforcement. Measurement of fracture energy (bond toughness) of the interfaces was carried out on a chevron notched short bar specimen. It was established that whether or not a strong interfacial bonding was conducive to toughness depended on the criterion used to describe the toughness of the composites. Four-point bend tests were also used to evaluate the effects of the size and orientation of ductile laminae on the toughness of the composites. The results indicated that the

toughness of the composites increased with increasing size of the Nb laminae and ductile laminae offered two dimensional toughening.

All the toughness evaluations and examinations of the interaction of cracks with ductile reinforcements indicated that (1) ductile phase toughening involved large-scale bridging, i.e., the bridging-length was at the same magnitude as the crack length, the specimen size or the distance from the crack to the specimen boundaries; and (2) the toughening of the brittle MoSi₂ matrix with Nb could be described by the equilibrium stress distribution across the crack surface. According to these observations, a general approach was proposed to compute the ductile phase toughening in the case of large-scale bridging. The approach, which allowed for the prediction of the typical R-curve behaviors of ductile-phase-toughened composites, encompassed the effects of the bonding strength of the matrix/reinforcement interface, the size of ductile phases and the intrinsic mechanical properties of the ductile phases and matrix.

CHAPTER 2 LITERATURE SURVEY

2.1 Theoretical Background

The basis for toughening brittle materials can be best presented using a fracture mechanics approach for crack propagation within the materials. Using this approach, the stress state near a sharp crack is related to the size of the crack and the applied load, and is described in terms of a stress intensity factor. The relation between these three parameters is given in the following form [27]

$$K = \beta \sigma \sqrt{\pi a} \quad (2.1)$$

where K is the stress intensity factor ($\text{MPa.m}^{1/2}$), $\beta = \beta\left(\frac{a}{L}\right)$ is a dimensionless number depending on the geometry of the cracked part, a is the characteristic dimension of a crack (m), L is a unified length dimension describing the geometry of the cracked part (m), and σ is the applied load (MPa).

A cracked part will fracture when the remotely applied load increases to a critical level (σ_f) at which the stress intensity factor, K , reaches a critical value (K_c). The critical stress intensity factor, K_c , is defined from eq. (2.1) as the value of K at which a failure stress, σ_f , causes a crack of size $2a$ to propagate, leading to failure of the cracked part. According to this definition, a material fractures when the following condition is satisfied [27]

$$K > K_c \quad (2.2)$$

K_c is a material property and is commonly referred to as the material's fracture toughness. The fracture toughness of a material is directly related to the fracture surface energy. Based on the conservation of energy, an equation describing the

relation between failure stress, σ_f , and the fracture surface energy, γ , for brittle materials can be derived from Griffith's theory which takes the form of [28,29]

$$\sigma_f = \sqrt{\frac{2 E \gamma}{(1 - \nu^2) \pi a}} \quad (2.3)$$

where E and ν are Young's modulus and Poisson's ratio of the material, respectively. Comparing eqs. (2.1) and (2.3), it is evident that fracture toughness increases with increasing fracture surface energy. Fracture toughness is also related to the plasticity of the material. Plastic deformation at the crack tip blunts the crack, cutting off the elastic singular peak of the stress distribution near the crack tip [30,31]. Therefore, much higher external stress has to be applied to fracture the material.

The J-integral proposed by Rice [32,33] provides a convenient way to handle fracture of materials with plasticity. The J-integral is an energy line integral defined for two-dimensional problems (Fig. 1) and is given by [32,33]

$$J = \int_{\tau} \left[\phi dx_2 - T_i \frac{\partial U_i}{\partial x_i} dS \right] \quad (2.4)$$

where τ is any contour surrounding the crack tip and traversing in the counterclockwise sense as shown in the figure, S is the arc length of the curve, ϕ is the strain energy density, T_i is the traction vectors defined by the outward normal n along τ and equals $\sigma_{ij} n$, U_i is the displacement vectors, and x_i is the axes of the coordinate as defined in Fig. 2.1.

The relation between the J-integral and the critical stress intensity factor for mode I crack propagation is [34]

$$J = \frac{C}{E} K_I^2 \quad (2.5)$$

where $C = 1$ and $(1 - \nu)$ for plane stress and plane strain, respectively. Because the J-integral is independent of the chosen path [32,33], it can be evaluated along a path chosen to give the greatest computational advantage. Thus, either the stress analysis or

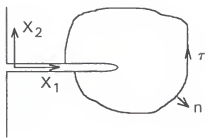


Fig. 2.1 Flat surface notch in two-dimensional deformation field. τ denotes any curve surrounding the tip [32].

energy approach can be used to analyze fracture of materials, depending on the problem in hand.

2.2 Toughening Mechanisms in Brittle Matrix Composites

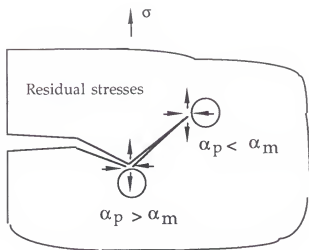
From eqs. (2.1) and (2.2), it is clear that in order to increase the failure stress of materials, several approaches may be taken: reduce the size of the existing critical-sized flaws, or increase the fracture toughness of the material, or introduce a compressive stress on the surfaces of the material. In practical terms, the first approach has limitations. Even if machining flaws and inclusions are eliminated, many flaws can be introduced on the surface during handling and in service. The latters can be achieved by microalloying the intermetallics to improve their plasticity, or by tempering and ion-exchange strengthening, or by compositing approaches.

Any composite approach will utilize one or more of the following means to improve the toughness of brittle materials:

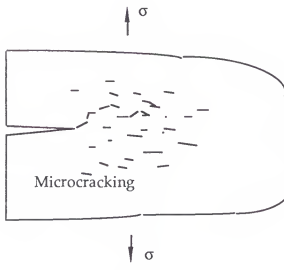
1. Increase the fracture surface area.
2. Create an irreversible process zone near the crack tip to enhance energy absorption.
3. Change the fracture mode, i.e., mode I to mode II or III.
4. Reduce the stress intensity at the crack tip.

In the following few pages the mechanisms utilizing the above means to improve the fracture toughness of brittle materials will be reviewed. The mechanisms usually fall into several overlapping categories and may be highly interactive. However, the discussion of these mechanisms will be carried out in separate categories for convenience.

Crack Deflection. Crack deflection involves out of plane bending (tilting and twisting) of a crack front. The process is pictured schematically in Fig. 2.2. The



(a)



(b)

Fig. 2.2 Caption overleaf.

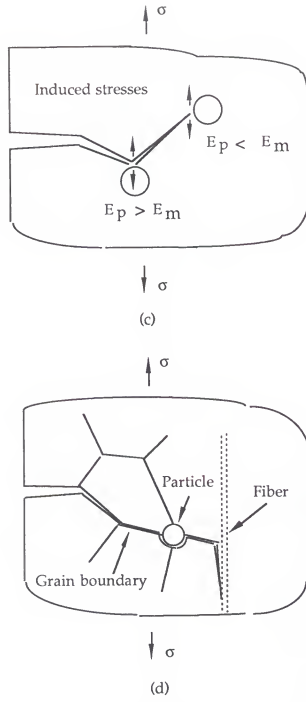


Fig. 2.2 Mechanisms for producing crack deflection. (a) Residual stresses from thermal expansion mismatches. (b) Microcracking, leading to crack branching and deflection. (c) Elastic mismatches between phases, leading to induced stresses and crack deflection. (d) Weak interfaces, which deflect crack.

approaches for ensuring crack-microstructure interaction and thus producing crack deflection include the introduction of residual stresses from thermal expansion anisotropy and/or thermal expansion mismatches, Fig. 2.2(a); stress induced microcracking at second-phase particles, Fig. 2.2(b); induced stresses from elastic mismatches, Fig. 2.2(c), and weak interface between phases, Fig. 2.2(d). The toughness increase due to crack deflection comes not only from the increase in the fracture surface area, but also from the change of the fracture mode from pure mode I to a mixture of mode I and mode II (tilted crack) or mode I and mode III (twisted crack). As the fracture mode changes from mode I to a mixed mode, the primary driving force (i.e., the K_I) decreases, and the crack must also be driven by the shear components of the stress field. In addition, the typically larger values of K_{IIC} and K_{IIIC} relative to K_{Ic} are also contributed to the increased toughness.

Effects of crack deflection on material toughness have been examined theoretically by Faber and Evans [35] for composites containing dispersions of spheres, discs and rods. In their treatment, the local stress intensity factors at crack front, K_1 , K_2 and K_3 , as a function of deflection angle were assessed and the driving force for the crack advance was assumed governed by the average strain energy release rate across the crack front which contained planar portion as well as tilted and twisted portions. Of particular interest in their results is the prediction that toughening is invariant with particle size, and depends only on particle shape, distribution and volume fraction. The most effective morphology for toughening is the rod with a high aspect ratio. As high as four-fold increases in fracture toughness has been predicted for rods with an aspect ratio of 12. Additional important results from their analysis are that toughening comes almost entirely from crack twist and is volume fraction invariant above ~ 0.2 for all three morphologies studied.

Experimentally, several investigators have observed evidence of crack deflection and toughening by this mechanism. Faber and Evans [36], in a companion study to the

one discussed above, verified the independence of deflection toughening on particle size and the morphology effects predicted by their model. They also observed [37] the existence of crack deflection toughening in SiC/Al₂O₃ and SiC/ZrO₂ composites. About 60% and 100% increases in toughness over the sintered SiC matrix were reported for the SiC/Al₂O₃ and SiC/ZrO₂ composites, respectively. Swareengen et al. [38] observed deflection toughening in composites of a low expansion borosilicate glass containing alumina spheres and as high as a three-fold increase in toughness was achieved. Carter and Hurley [39] reported that crack deflection was an important toughening mechanism in SiC-whisker-reinforced MoSi₂, and a toughness increase of 50% over the unreinforced matrix was obtained. All in all, increases of 2 - 4 times in fracture toughness over that of the matrix are possible by the crack deflection mechanism.

Crack Bowing. Crack bowing is a process of in-plane bending of a crack front whereby a propagating crack is momentarily pinned at discrete locations by appropriate dispersed second-phase inhomogeneities. Figure 2.3 is a schematic of this process, which shows that a crack front interacts with an array of second-phase inclusions, i.e., the crack front bows out between the inclusions. This phenomenon could be achieved by, for example, dispersion of second phase particles, fibers or voids.

Direct observation of crack bowing has been made using ultrasonic fractography techniques [38,40-42], which leaves a permanent record of crack front advancement on the fracture surface in the form of rib mark. Other investigators also reported crack bowing produced by voids in NaCl [43,44], MgO [45] and Al₂O₃ [46], by whiskers or fibers in MgO [47] and in glasses [48], by brittle particles in a brittle epoxy [49] and glass [50] and by ductile particles in glasses [41,42,51,52].

Toughening by crack bowing is attributed to a line tension effect at the crack front, a concept first postulated by Lange [53]. In his and other subsequent analyses [54-56], it was assumed that the increment of energy absorbed for an increment of

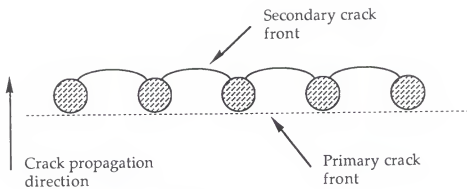


Fig. 2.3 Schematic of crack bowing.

crack extension consisted of two parts, i.e., one part associated with the energy to form new surface area and the other part associated with the energy to form the increased length of crack front. The localized pinning of cracks would result in an increase in the energy associated with the crack front (line tension effect) since the length of the crack front was increased due to crack bowing. Their analyses [54-56] suggested that a substantial increases in toughness and strength could be achieved by a high volume fraction of a dispersed phase of small size. However, a high volume fraction of small size particles is difficult to achieve because of uniformity of dispersion and chemical reactivity problems. In addition to these difficulties, there must be some effective mechanisms for ensuring that the crack front intersects the particles, rather than bypassing them. As noted in the discussion of crack deflection, this would require significant residual stresses. With this condition satisfied, the composites would also exhibit crack deflection toughening and toughening by other mechanisms (for instance, crack bridging and/or crack shielding), and the contribution of the crack bowing would probably be negligible. Due to the aforementioned limitations, only about 20% - 100% increase by crack bowing in toughness over the basic matrix have been reported.

Crack Shielding. Crack shielding, as it is usually considered, is a toughening mechanism involving a process zone in which the microstructure changes due to the stress field in the near vicinity of crack tip. The process zone shields the crack from the applied stresses, hence reducing the stress intensity at the crack tip. Approaches to achieve crack shielding consist of (1) phase transformation in the process zone, Fig. 2.4(a), such as martensitic transformation of zirconia in alumina-zirconia [57-59] and mullite-zirconia composites [60-64]; and (2) stress-induced microcracking in the process zone, Fig. 2.4(b), as observed in rock [65], Al₂O₃/ZrO₂ composites [66] and ceramic-glass materials [67,68].

Transformation toughening in ZrO₂ containing materials is related to the diffusionless transformation of metastable tetragonal ZrO₂ into a stable monoclinic

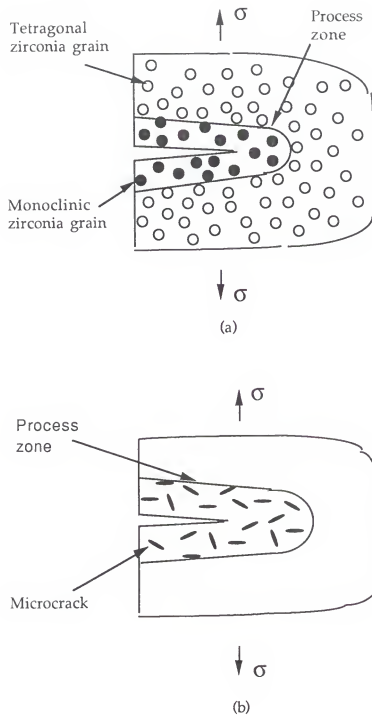


Fig. 2.4 Microstructural features of ceramics toughened by crack shielding.
 (a) crack shielding arising from phase transformation; (b) crack shielding resulting from microcracking.

phase with a higher specific volume. This increase in specific volume effectively reduces the stress intensity at the crack tip by load transfer from the crack tip to the near-by region, as occurs in the yield region at the front of a crack tip in a metal. Thus, additional load must be applied to cause the crack to propagate. The contribution of the transformation to toughness has been treated theoretically by several investigators [69-73]. In all analyses, the fracture toughness of the composites was treated as the sum of the matrix toughness and the transformation toughening contribution. The contribution from the transformation toughening was related to the chemical free-energy change for the transformation of tetragonal ZrO_2 to monoclinic ZrO_2 , to the change in strain energy and the excess surface energy associated with the transformation, and to the size of the transformation zone and volume fraction of the metastable phase in the composites. All analyses lead to the following conclusions: toughness can be increased by (1) decreasing the service temperature, (2) decreasing the alloy content in ZrO_2 , (3) increasing the volume fraction of the metastable phase, and (4) increasing the size of the transformation zone.

Phase transformation toughening has been observed in many other systems. Moya and Osendi [60] reported an increase of K_{Ic} from 2 to 3 MPa.m^{1/2} for a mullite/ ZrO_2 composite. For ZrO_2 -toughened alumina, K_{Ic} values of ~ 12 [70] and 16 MPa.m^{1/2} [71] were reported. Transformation toughening was also found in single crystal and polycrystal zirconia materials containing metastable precipitates (partially stabilized zirconia) or consisting of only tetragonal phase (fully stabilized zirconia). Toughnesses as high as 9 MPa.m^{1/2} have been reported for tetragonal polycrystals [74], while ~ 12 MPa.m^{1/2} was observed in MgO-partially-stabilized zirconia [75]. Transformation toughening to date is one of the most successful toughening approaches used. However, it is highly temperature dependent. As temperature increases, toughening decreases, going to zero when temperature reaches a point where the

decrease of Gibbs free energy due to the transformation is offset by the increase of strain energy associated with the transformation.

Microcracking in a process zone around macrocrack tips is a result of the combination of the residual stresses and the stress field associated with the crack. Opening of the microcracks requires the contribution of energy from the applied loads. Thus, additional load must be applied to make the crack propagate. For microcracking to occur, there should be property mismatches. Mismatches in thermal expansion are the most common source [76], but mismatches due to phase transformation [77-79] and differences in elastic modulus [78] can also be important. It is the combination of such residual stresses with the applied stress field that causes microcracking.

The contribution of microcracking to toughness has been analyzed theoretically by Hoagland and Embury [80], Evans and Cannon [71], Evans and Faber [81], and Hutchinson [82]. In all treatments, microcrack toughening was assessed in terms of the change of elastic energy associated with the release of residual stresses on the microcrack plane and reduction in the elastic moduli of the process zone, and the increase of surface energy arising from the formation of the microcracks. Their results showed that the net increase of toughness was a function of the microcrack density (number/unit volume), the size of the process zone, the contributions from the residual stress field and from the increase of the compliance of the process zone, and the surface area of the microcracks. Microcrack toughening is strongly particle size dependent [68,78,81,83]. At relatively small particle sizes, particles are stable even in the near-tip field and therefore, microcracking does not occur. As the particle size increases, a zone of microcracks is formed, resulting in an increase in toughness. At some critical particle size, spontaneous microcracking occurs on cooling, leading to no toughening for the materials. Thus, toughening only occurs with median size of particles.

Experimentally, microcrack toughening has been observed in many systems. Claussen et al. [84] observed an increase of K_{Ic} from ~ 5 to 10 MPa.m^{1/2} for ZrO₂

toughened Al_2O_3 composite. Fu and Evans [83] reported a toughness increase in three single phase polycrystal materials, i.e., Al_2O_3 , BaTiO_3 and Nb_2O_5 . Although it is possible to utilize microcracking to toughen brittle materials, the toughening increments due to microcracking are relatively small, compared with transformation toughening, because transformation-related dilatation is substantially larger than microcracking dilatation. Another problem with microcrack toughening is the concern of the coalescence of microcracks to form strength-limiting macrocracks. To date, there is little experimental evidence in the way of microcracking effects on strength.

An additional mechanism which may be classified under the stress-induced microcracking is crack branching. A few ceramics have been demonstrated to have intricate crack bifurcations [85]. The crack opening associated with the branched cracks provides volume expansion in the process zone and should result in toughening [86].

Crack Blunting. Crack blunting occurs when the sharp crack tip is blunted via limited plasticity or viscous flow at the crack tip or when the sharp crack intercepts a void or a ductile phase inclusion. Blunting of the crack reduces crack tip stress intensity, and therefore improves the fracture toughness.

Viscous flow would normally be associated with glassy phases and high temperatures. Thus, the toughening effect via viscous flow is very limited because such flow may indeed be the source of failure through gross viscous flow. Similarly, the effects of crack tip blunting through microplasticity are very limited because of the high Peierl's stresses and limited slip systems available in typical ceramics and intermetallics. Introduction of ductile second phases should provide a seemingly effective blunting mechanism. However, other toughening mechanisms (crack bridging, crack bowing and crack deflection) would operate with the introduction of the ductile phases and the contribution of the crack tip blunting process would probably become negligible.

Incorporation of porosity has been shown to improve toughness. An example was lead zirconate titanate material containing an array of ordered voids, which showed 1-2 fold increases in the work of fracture and 100% increase in strength of the ceramic [87]. The toughening was attributed to crack bowing, blunting and shielding, the latter through the local changes in compliance associated with the voids. Another example is provided by Passmore et al. [50] with porosity in Al_2O_3 .

Crack Bridging. Crack bridging refers to a phenomenon where unbroken ligaments behind a crack's wake "bridge" across the crack faces and hold them together to some extent, thus reducing the stress intensity at the crack tip. These ligaments can be coarse grains in noncubic monolithic materials such as alumina [88,89], a ductile metal [20,21,90-95], strong whiskers [96-101], and/or fibers [102-104].

The effects of crack bridging on material's toughness have been the focus of several theoretical treatments [20-26,92,93,105-107]. In these analyses, the action of the bridging ligaments is treated in terms of a zone of tractive forces in the crack wake which tend to hold the crack faces together and reduce the stress intensity seen at the crack tip, as shown in Fig. 2.5. Thus, the total stress intensity acting at the crack tip is assumed to be a superposition of an opening mode stress intensity caused by the external stress and a stress intensity of opposite sign caused by the clamping forces of the bridging ligaments. The key to analyzing the toughening effect of the bridging lies in the estimation of the clamping forces which in turn depends on the nature of the ligaments, i. e., ductile phases or ceramic fibers, and the characteristics of the matrix/reinforcement interface, viz., frictional bridging or strong particle bridging. For ceramic reinforcements, the magnitude of the clamping forces is treated according to the characteristics of the interface in terms of frictional bridging [20,108] or strong bonding bridging [20], or simplified spring bridging [25,106,107]. These analyses lead to two important conclusions: (1) the toughness increases as the strength of the

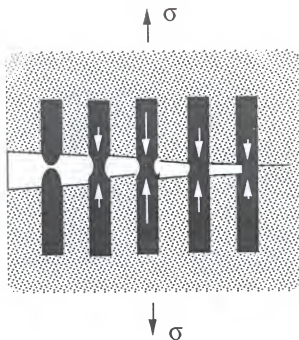


Fig. 2.5 Crack bridging by ductile ligaments. Note that the clamping forces of the bridging ligaments are a function of the distance away from the crack tip. The length of the arrows indicates the magnitude of the clamping forces.

Table 2.1 Ceramics with Enhanced Toughness [112]

Toughening Mechanism	Material	Maximum Toughness MPa.m ^{1/2}
Fiber reinforced	LAS/SiC	~ 20
	Glass/C	~ 20
	SiC/SiC	~ 20
Whisker reinforced	Al ₂ O ₃ /SiC (0.2) Si ₃ N ₄ /SiC (0.2)	10 14
Ductile network	Al ₂ O ₃ /Al (0.2) B ₄ C/Al (0.2) WC/Co (0.2)	12 14 20
Transformation toughened	PSZ TZP ZTA	18 16 10
Microcrack toughened	ZTA Si ₃ N ₄ /SiC	7 7

reinforcement increases, and (2) the stress required to propagate a matrix crack is almost independent of the crack length, as contrasted with the behavior of cracks in unreinforced brittle materials, for which the strength decreases with a $-1/2$.

Evidence of crack bridging by ceramic whiskers or fibers were reported in several composites. A K_{Ic} of 25 MPa.m $^{1/2}$ was achieved in SiC-fiber-reinforced ZrTiO₄ [109], and an increase of K_{Ic} from 6 to 12 MPa.m $^{1/2}$ was observed in SiC-whisker-reinforced zirconia [110]. MoSi₂ was also toughened with SiC whiskers and an increase of 50% in toughness was reported [111]. An important conclusion from these experiments is that a weak interface leads to a higher toughness than a strong interface. The debonding at the matrix/reinforcement interface guarantees that the matrix crack bypasses the fiber or whisker, leaving them intact. Otherwise, the crack propagates through the reinforcement, and there would be little improvement in toughness.

Bridging by ductile phases also provide an effective means to improving toughness. This will be detailed separately in the next section because the topic is the focus of the present study.

Finally, it would be useful to finish this section using a table (Table 2.1) from Evans [112], which summarizes the maximum toughness achieved using different toughening mechanisms. From the table and the above discussion, it is clear that crack bridging and phase transformation to date are the most effective mechanisms. However, phase transformation toughening is limited to relatively low temperatures. In contrast, crack bridging can provide toughening at ambient temperatures as well as at elevated temperatures. Thus, it appears that crack bridging is the most important toughening mechanism at elevated temperatures.

2.3 Ductile Phase Toughening

The primary mechanism responsible for ductile phase toughening is the bridging of ductile ligaments behind the advancing crack tip, although other effects

such as crack deflection [46,113,114], crack bowing [44,45,54,55] and crack shielding [23] also contribute. The physical mechanism of the bridging is shown in Fig. 2.5. The ductile ligaments spanning the advancing crack must stretch as the crack opens until they fracture or decohere. The work of stretching and fracturing the bridging ligaments contributes to the toughness of the composite. When the size of the bridging zone in the wake of the crack tip is small relative to the crack length and the specimen dimension (i.e., small-scale bridging), the steady-state toughness of the composite, K_{com} , can be related to the fracture energy increase due to the bridging, ΔG , with the aid of the equation (2.4) by taking the contour τ as shown in Fig. 2.6. The final relation takes the form of [25,115]

$$\frac{(1 - v_{com}^2) K_{com}^2}{E_{com}} = \frac{(1 - v_m^2) K_m^2}{E_m} + \Delta G \quad (2.6)$$

where v , E and K are Poisson's ratio, the elastic modulus and fracture toughness, respectively. The subscripts 'com' and 'm' refer to the composite and matrix, respectively. The fracture energy increase, ΔG , is related to the work of stretching and fracturing ductile ligaments as follows [20,23]

$$\Delta G = V_f \int_0^{u^*} \sigma(u) du \quad (2.7)$$

where $\sigma(u)$ is the nominal stress carried by the constrained ductile reinforcement for a given crack opening u , V_f is the volume fraction of the reinforcement and u^* is the crack opening at the point when the ductile reinforcement fails. The integral in eq. (2.7) is commonly referred to as the work of rupture of the ductile reinforcement.

From eqs. (2.6) and (2.7), it is evident that the key to predict the increased fracture toughness is to find the stress-displacement function, $\sigma(u)$, of the constrained ductile phase. Since $\sigma(u)$ is different from that measured in a simple tensile test, several investigators have attempted to relate $\sigma(u)$ to the uniaxial stress-strain properties of the ductile phase. The methods used included a slip line field analysis

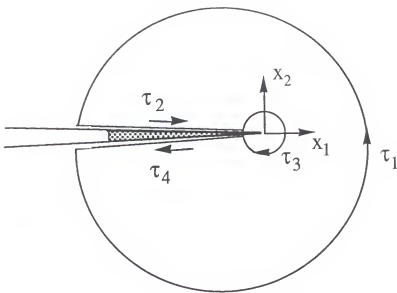


Fig. 2.6 J-integral path for bridging toughening. The shaded area indicates the bridging zone. Contour $\tau = \tau_1 + \tau_2 + \tau_3 + \tau_4$, where τ_1 is far from the crack tip, τ_3 is right at the tip, τ_2 & τ_4 are the upper and lower surfaces of the bridging zone.

[20,23], finite element methods [23,24], spring models [25,106,107] and geometric models [21,23,24,26]. These analyses conclude that the work of rupture increases with increasing strength of the ductile reinforcement and decohesion at the matrix/reinforcement interface.

Experimental determination of the $\sigma(u)$ has also been initiated by Ashby et al [26]. Their test specimen consisted of one ductile reinforcement (Pb) imbedded in a precracked brittle matrix (glass), and a tensile test is conducted to evaluate the stress-displacement function, $\sigma(u)$. They found that the work of rupture was enhanced by limited decohesion at the interface. They also found that the work of rupture normalized with the yield strength and size of the ductile phase was constant for different sizes of lead in glass. Other investigators have also conducted similar tests on other systems such as Nb in TiAl and TiNb in TiAl [116, 117], and Nb in MoSi₂ [118, 119-121]. Working with TiAl/TiNb systems, Deve et al. [117] found that whether or not extensive decohesion was desirable for a high work of rupture depended on the work hardening capability of the ductile phase. For MoSi₂/Nb system [120,121], it was found that the normalized work of rupture depended on the size of the niobium rather than being a constant, and varied from 5.3 to 2.8 when the half thickness, a_0 , of the niobium changed from 0.5 to 0.125 mm. These results indicated that the effects of decohesion and size of ductile phase on the toughness were complicated and interdependent with other material properties.

Evidence of ductile phase toughening has been presented by several investigators. Khaund and Nicholson [46] observed a maximum composite toughness of greater than fifty times that of the glass matrix for composites containing 20 vol.% of aluminum. Krstic et al. [122] reported a similar increase in fracture toughness in a similar composite. A K_{IC} of about 5 MPa.m^{1/2} was achieved in borosilicate toughened with Fe-Ni-Co alloy particles [113,114]. Improvement of toughness was also found in composites reinforced with continuous ductile phase network [95,123-125]. An increase

of K_{Ic} from ~ 1.4 to 4.5 MPa.m^{1/2} was observed for FeO/Fe network [125] and ZrO₂/ZrO network composites [124]. In WC/Co network composites, a K_{Ic} of 20 MPa.m^{1/2} has been achieved [95]. Toughening of TiAl with pancake-shaped Nb has raised K_{Ic} from 8 to 20 MPa.m^{1/2} [126].

Parameters affecting ductile phase toughening include (1) the morphology of the ductile phase, (2) the nature of the matrix/reinforcement interface, (3) size of the ductile phase, and (4) intrinsic mechanical properties of the ductile phase. Thus far, the morphologies studied include particles [46,113,114,122], continuous boundary networks [95,123-125], fibers [91,127], and pancakes [126]. For particle-reinforced composites, some systems have shown an increase in toughness [46,122], some have not [46,122,128]. A common observation in these studies was that whenever matrix cracks were attracted to ductile particles, a large improvement in toughness was obtained. Otherwise, little improvement was gained. In contrast, toughening effect was observed in all continuous network, fiber, and pancake reinforced composites. The reason for this is that the special geometric shapes of continuous network, fibers, and pancake guarantee the crack/ductile phase interactions, therefore the inherent toughness of ductile phase is utilized.

Theoretical analyses of the stress field [122,129] indicated that crack could be attracted to or pass ductile particle indiscriminately only when the following criteria are satisfied simultaneously: (1) Young's moduli of matrix E_m and ductile particle E_p are the same or $E_m > E_p$, and (2) thermal expansion coefficients of matrix α_m and particle α_p are the same or α_p is slightly lower than α_m . This prediction, which has been substantiated by experiments [46,122,128], provides a guidance for the designing of particulate reinforced composites.

It seems that different shapes of ductile phases also require different matrix/reinforcement interfaces. As mentioned before, weak interfaces enhance decohesion at the interface, and therefore enhance the work of rupture of ductile phases

if the crack bridging mechanism operates [23,24,26]. For particulate toughened composites, the scenario may be different, i.e., cracks tends to travel along the weak interface instead of utilizing the inherent toughness of the ductile particles, and therefore strong interfaces aid the operation of the bridging mechanism, leading to the utilization of the toughness of the ductile particles [46,122].

Effects of the size of ductile phases have been examined experimentally by several investigators. The systems examined were Al₂O₃/Ni laminate [130], WC-Co/W particle [131], and NiAl/Nb fibers [132]. In the size ranges tested, all of the results exhibited that large size ductile phases had better toughening effects than smaller ones. These results are in agreement with the theoretical analysis [26].

So far, the effect of the intrinsic properties of ductile phases has not been studied experimentally and systematically. However, theoretical analyses indicate that toughness increases with increasing strength and work hardening rate of ductile phases [23,24,26,120,121].

Finally, it should be pointed out that the modeling work mentioned above [20,21,23,24,26] analyzed the effects of ductile phase constitutive behavior on toughness quantitatively based on the assumptions of small scale bridging of an infinite crack in an infinite specimen. However, in cases of potential toughening, the bridging zone is often a significant fraction of crack length [91,116,133] and toughening is likely to be sensitive to the specimen geometry and crack length. Recognizing this situation, Ravichandran [134,135], Cox [136], and Cox and Low [137] have recently proposed models describing large scale bridging to take the effects of the specimen geometry and crack length into account. In their treatments [134,135], it is assumed that the effective stress intensity acting at the crack tip, K_{tip} , is a superimposition of an opening mode stress intensity caused by the external stress, K_{inf} , and a stress intensity of opposite sign caused by the clamping forces of the bridging ligaments, K_{bridge} , i.e.,

$$K_{tip} = K_{inf} - K_{bridge} \quad (2.8)$$

By using appropriate Green's function, K_{tip} can be related to the external stress, σ_{inf} , and the bridging stress, σ_{bridge} , with the following equation [134,135]

$$K_{tip} = \int_0^a (\sigma_{inf} - \sigma_{bridge}(x,a)) h(x,a) dx \quad (2.9)$$

where a is the length of the crack, x is the position along the crack face, and $h(x,a)$ is the Green's function which is a function of specimen and crack configuration and can be found in handbooks for some standard specimen geometries. Bridging stress is arrived at iteratively [138]. However, a knowledge of stress-displacement function, $\sigma(u)$, of the constrained ductile phase is necessary for the iteration, which imposes a demand for determining $\sigma(u)$, a situation similar to the small-scale-bridging analysis..

2.4 Physical and Chemical Properties of MoSi₂ matrix

Molybdenum disilicide is an extremely promising intermetallic compound for high temperature structural applications in oxidizing atmospheres. The phase diagram (Fig. 7) [139] indicates that MoSi₂ melts congruently at a high temperature of ~ 2020°C, has a tetragonal structure below 1900°C and a hexagonal structure above this temperature. It has a moderate density (6.31 g/cm³), and an excellent electrical and thermal conductivity. It is extremely brittle with a fracture toughness of about 3 - 5 MPa.m^{1/2} [91,111,140] and has low impact strength at low temperatures, but exhibiting a brittle to ductile transition at approximately 925°C [141,142]. Above this temperature, MoSi₂ behaves more like a metal showing yielding and stress-relieving characteristics. Since it undergoes creep and plastic deformation at temperatures above transition temperature, the strength at elevated temperatures is relatively low. Therefore, to make MoSi₂ as a viable structural material, it is necessary to improve the room-temperature fracture toughness, elevated-temperature strength and creep resistance.

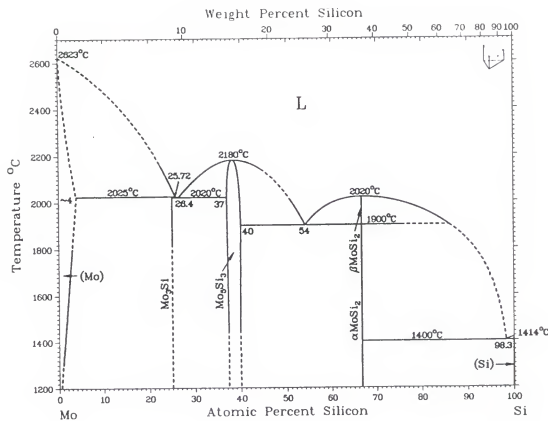


Fig. 2.7 Mo-Si Phase Diagram [139].

MoSi_2 has excellent high-temperature oxidation resistance. Its use as a heating element in furnaces that operate in air at temperatures up to 1700°C is a clear demonstration of its excellent high-temperature properties. Its outstanding oxidation resistance is due to the formation of a glassy silica (SiO_2) layer which acts as a protective film at high temperature [143]. However, MoSi_2 can disintegrate catastrophically (pest) during oxidation at temperatures about $400 - 600^{\circ}\text{C}$ [143-146]. At these temperatures, a mixed oxide layer containing amorphous SiO_2 , monoclinic Mo_9O_{26} , and MoO_3 platelets is formed on the surface of MoSi_2 , as contrasted with the formation of only SiO_2 layer at higher temperature oxidation [143]. The mixed oxide layer is voluminous, poorly adherent and even flakes off, resulting in a complete disintegration of MoSi_2 specimens [144,146]. However, a recent research [143] indicated that MoSi_2 -pest could be prevented by ensuring the material is > 95 pct dense or by high-temperature preoxidation to produce a protective SiO_2 layer. Thus, MoSi_2 -pest is not expected to prevent its application as a monolithic or composite matrix material for high-temperature applications.

CHAPTER 3 EXPERIMENTAL PROCEDURE

3.1 Microstructural Characterization and Raw Materials

The microstructure, fracture surfaces, and interfaces of the composites were characterized with optical microscope, scanning electron microscope, and electron microprobe. X-ray diffractometry (XRD) was used to assist the determination of the phases presented in the commercially pure MoSi₂ powder. The particle size of the MoSi₂ powder was determined based on the principle of the centrifugal photosedimentation using a particle size analyzer (Model CAPA-700). The grain size, d, of the hot-pressed MoSi₂ matrix and Nb reinforcements was assessed by the mean linear intercept method using the following formula:

$$d = \frac{L_T}{P_L} \quad (3.1)$$

where L_T is the length of the measuring line and P_L is the number of boundary intersected by the line.

The matrix of the composites was commercially pure MoSi₂ powder of -325 mesh (supplied by Johnson Mathey Inc.). The powder had an irregular shape as shown in Figure 3.1. Depending on the lot number of the powder, the average particle size ranged from 1.2 to about 4.8 μm diameter determined by the method of centrifugal photosedimentation. The composition provided by the vendor was Mo > 61.0%, Si 36.6%, C 0.06%, N 0.03%, O 1.22% and metallic impurities < 0.5% (wt%). Note that there is a high oxygen content in the as-received powder. Analysis of the x-ray diffractometry (XRD) showed only MoSi₂ peaks (2θ angles from 50° to 100°), indicating other phases if present were below the volume fraction detectable by XRD,

Table 3.1. Mechanical properties of as-received niobium *

Thickness of Nb foil (mm)	1.0	0.5	0.25
Microhardness (HV, kg/mm ²)	110	79.4	82.3
Yield strength (σ_0 , MPa)	204	121	123
Tensile strength (σ_u , MPa)	277	195	204
Elongation (δ)	0.403	0.523	0.468
Strength coefficient (MPa)	454	353	370
Strength hardening coefficient	0.173	0.245	0.243
σ_0/HV	1.85	1.52	1.49
σ_u/HV	2.52	2.45	2.48

* Only one sample for each condition was tested.

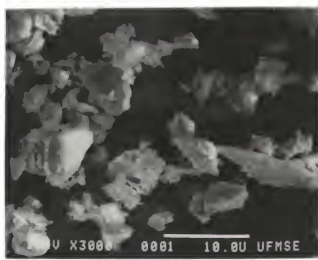


Fig. 3.1 Commercially pure MoSi₂ powder (supplied by Johnson Mathey Inc.)

or in the form of amorphous film on the surface of MoSi₂ powder such as a thin amorphous SiO₂ layer.

Different sizes of niobium in the form of foil or filament were used as ductile phases in the present study depending on the experimental objectives. The niobium had a purity of 99.8% based on metallic constituents (supplied by Johnson Matthey Inc.). Tensile and hardness tests on the as-received Nb indicated that the mechanical properties of Nb depended on the size of the niobium (see Table 3.1).

3.2 Fiber and Foil Coating Techniques

The coatings applied to the Nb surfaces included ZrO₂ or Al₂O₃. The former was applied by dipping the metal into a coating solution consisting of 97% ZrO₂ and 3% Al₂O₃ (supplied by ZYP Coatings, Inc.), while the latter was produced via sol-gel processing, physical vapor deposition or hot dipping in the molten aluminum followed by anodizing. The techniques for producing Al₂O₃ coating are detailed below.

Sol-gel coating technique. The sol solution was an aluminum-alkoxide-derived sol (using aluminum-sec-butoxide (ASB)), hydrolyzed in excess water and peptized with aluminum nitrate, Al(NO₃)₃. The procedure for preparing the sol solution has been described in detail by Clark et al. [147]. The ratio of aluminum nitrate to ASB in the sol was from 0.04 :1 to 0.07:1, a range which has been reported to produce the minimum volume gel with the highest solid concentration [148]. Solutions with ratios of water to ASB ranging from 100:1 to 25:1 were prepared. The compositions of the sols used are summarized in Table 3.2. Glycerol was added to some sol solutions to improve the flexibility of the dried gel [149].

The sol-gel coatings were produced by dipping Nb foils into the sol solution for 5 seconds or by electrophoretic deposition onto the Nb surface. For the latter technique, the Nb foil was kept parallel to the anode with a separation distance of 1 cm. A constant DC voltage ranging from 0.5 to 2 volts was applied across the

Table 3.2 Composition of the sol solution

Designation of the sol	$\frac{\text{Al}(\text{NO}_3)_3}{\text{ASB}}$	$\text{H}_2\text{O : ASB}$	$\frac{\text{H}_2\text{O}}{\text{glycerol}}$	pH	Viscosity (centipoise)
SG 1	0.04 : 1	100 : 1	100 : 2	3.35	2.13
SG2	0.07 : 1	100 : 1	100 : 2	3.05	2.27
SG3	0.04 : 1	50 : 1	100 : 2	3.05	4.41
SG4	0.07 : 1	50 : 1	100 : 2	2.85	4.52
SG5	0.04 : 1	25 : 1	50 : 2	2.80	-
SG6	0.04 : 1	100 : 1	nil	3.35	-

electrodes and the coating time was kept at 30 minutes for all the experiments. All coatings were conducted within 24 hours after the preparation of the sol to avoid aging of the sol. Once a coating was applied, the sample was withdrawn from the sol at a rate of 10 cm/sec for both dip coating and electrophoretic coating. After withdrawing from the sol, the Nb foils were suspended vertically for 48 hours at the ambient temperature before hot pressing with MoSi_2 powder. Some air dried Nb foils were further dried at 500°C for 1 hr with a heating rate of $30^\circ\text{C}/\text{min}$ before the hot pressing.

Physical vapor deposition. Physical vapor deposition of Al_2O_3 on Nb was conducted using a Thermionics 100-0030 system with an electron beam heated source, operating in 2×10^{-6} torr vacuum. The emission current was 200 mA with a potential difference between the cathode and the anode being 3 KV, resulting in a deposition rate of approximately $10 \text{ } \overset{0}{\text{\AA}}/\text{sec}$. By changing the deposition time, three different deposit thicknesses were obtained, i.e., 1, 2 and $3 \mu\text{m}$.

Hot dipping and anodizing. Hot dipping of Nb foils into the molten aluminum bath was conducted in an alumina crucible which was kept inside a box-type resistance

furnace. Aluminum used to prepare the molten bath had a nominal purity of 99.999 wt% based on metallic constituents. Two different bath temperatures, 930°C and 870°C, were chosen to evaluate the effects of the molten metal temperature on the thickness and uniformity of the coating. Dipping time varied from 2 to 5 min depending on the bath temperature used. All samples were withdrawn from the bath at a rate of ~ 10 cm /sec. Since the molten bath was exposed to the air directly, an oxide layer developed on the surface of the molten bath, which caused non-uniform aluminum coating on the first few Nb foils. These were excluded from the subsequent processing.

Anodizing of the hot dipped Nb foils was conducted in an electrolyte containing 5 wt% sulfuric acid. Such low acid concentrations were used because high concentrations tended to attack the alumina formed, and the film produced had been reported to be more dense using a low acid concentration [150]. The process was conducted at ambient temperature, and a constant DC voltage ranging from 10 to 20 volts was applied to produce current densities ranging from 5 to 25 mA/cm². Anodizing time was 30 minutes for most operating conditions.

3.3 Fabrication of MoSi₂ Matrix Composites

For the Nb filament toughened composites, the filaments were pre-aligned in a plane and set with acrylic resins. The Nb filament sheets were then stacked together with MoSi₂ powders in an appropriate thickness ratio and vacuum hot pressed at 1700°C for 40 min under a pressure of 30 MPa. The diameter of the filaments was 0.25 mm and the volume fraction of Nb in the composites was 10 or 20% .

For the Nb foil toughened composites, the coated or uncoated Nb foils were stacked with the MoSi₂ powders and vacuum hot pressed at 1400°C for 1 hr with a pressure of 40 MPa. The thickness of the Nb foils ranged from 0.127 to 1.0 mm and the volume fraction of the niobium was 20% in all the foil toughened composites. In

order to minimize residual thermal stresses, the hot pressed discs were held in the hot pressing chamber at 800°C for 1 hour before cooling down to room temperature. The residual thermal stresses induced with such processing have been estimated to be small with a tensile stress of 19 MPa in the matrix and a compressive stress of 79 MPa in the Nb on the lamina plane [151].

3.4 Measurement of Intrinsic Properties of the Ductile Phase

Since the flow behavior of constrained ductile phases is different from that measured from a simple tensile test, the experimental procedures proposed by Ashby et al. [26] were taken to measure the flow behavior of constrained Nb. For these experiments, laminated specimens were prepared by stacking a Nb foil with two layers of MoSi₂ powder at an appropriate ratio, and then vacuum hot pressing at 1400°C for 1 hour under a pressure of 40 MPa. Three different thicknesses of Nb foils (1.0, 0.5 and 0.25 mm) were used to prepare the laminated composites. The hot pressed discs were cut into rectangular tensile test bars with dimensions of 5.0 x 3.9 x 30.0 mm, as shown in Fig. 3.2. Straight-through notches in the MoSi₂ matrix were introduced using a diamond wafering blade with a thickness of 0.15 mm. The distance from the notch tip to the laminate interface was selected as 300 µm for 1.0 mm thick Nb lamina and 200 µm for 0.5 and 0.25 mm thick Nb laminae. Such distances have been found to be small enough not to distort the stress-displacement curve of the constrained ductile reinforcement and at the same time maintain an appropriate degree of elastic constraint from the matrix [119].

Displacement controlled tensile tests were conducted using an INSTRON machine with a displacement speed of 0.005 in/min. Wedge type grips were used to clamp the specimens and load train alignment was achieved by coupling the top trip to a universal joint. The load was recorded as a function of cross-head displacement.

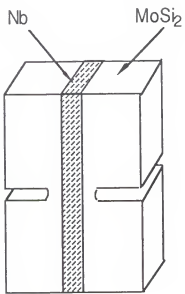


Fig. 3.2 Schematic of a composite laminate tensile test specimen.

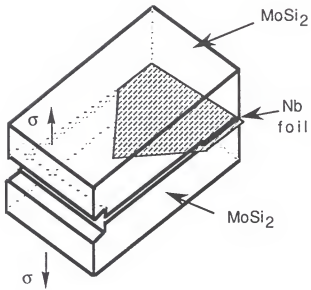


Fig. 3.3 Short bar specimen geometry.

3.5 Measurement of Fracture Energy of Matrix/Reinforcement Interface

The measurement of the interfacial fracture energy was conducted on chevron notched short bars using the procedures recommended in Reference 152. In the present study, however, a modified specimen geometry, as shown in Fig 3.3, was used. An advantage of the present geometry is that there is no need for compliance calibration due to symmetry of compliance of the specimen with respect to the interface. The technique involves determining the critical stress intensity factor from the peak load of the notched bars and then converting the critical stress intensity factor to the fracture energy of the interface. The equation used to calculate the fracture energy of the interface, G_{\max} , is [152]

$$G_{\max} = \frac{K_{ICSR}^2}{E} \quad (3.2)$$

where E is the elastic modulus of MoSi₂ and K_{ICSR} is the critical stress intensity factor determined from the peak load of the short bar test. The test specimens were hot pressed with a coated or uncoated Nb foil (0.127 mm thick) sandwiched in between two layers of MoSi₂. The hot pressed discs were then cut into rectangular short bar with dimensions of 8.28 x 9.25 x 14.29 mm (Fig. 3.3). The notch in the short bar was cut parallel to the foil using a diamond wafering blade with a thickness of 0.4 mm. The thickness of the notch was chosen to be slightly larger than that of the foil to insure that the initiation and propagation of the crack is at the weakest position among various interfaces between matrix/coating/reinforcement. The specimen was loaded at a constant test machine crosshead speed of 0.005 in/min using a hydro-servo controlled MTS. The load was recorded as a function of the crosshead displacement.

3.6 Measurement of Toughness of the Composites

The toughnesses of the MoSi₂ matrix and the laminated composites were measured by 4-point bending of chevron notched specimens, with an inner and outer

span of 10 and 20 mm, respectively, using a hydro-servo controlled MTS with a cross head speed of 4×10^{-4} mm/sec. A schematic of the bend test setup is shown in Fig. 3.4. The notch on each sample was cut perpendicular or transverse to the laminate plane depending on the purpose of the experiments.

The peak load of the bending tests was used to calculate the toughness of the composites, K_{max} , with the aid of the following equation [153]

$$K_{max} = \frac{P_{max}}{B \sqrt{W}} Y_{min}^* \quad (3.3)$$

where P_{max} is the maximum test load, B and W are the width and height of the bending bar, respectively, and Y_{min}^* is the minimum value of the dimensionless stress intensity factor coefficient as a function of relative crack length for the particular specimen used. It should be noted that because of the rising crack-growth resistance for ductile-phase-toughened composites, the maximum load and the minimum value of the dimensionless stress intensity factor coefficient do not occur coincidentally at the same crack length, and therefore P_{max} does not exactly correspond to the stress-intensity factor at failure, but a good approximation to it [154-157]. The fact that P_{max} and Y_{min}^* do not occur coincidentally at the same crack length also induces a specimen size effect [154,157]. Thus, the dimensions of the specimens in the present study were kept constant, and the value calculated using eq. (3.2) is called "damage tolerance" and designated as K_{max} in the paper, rather than K_{IC} .

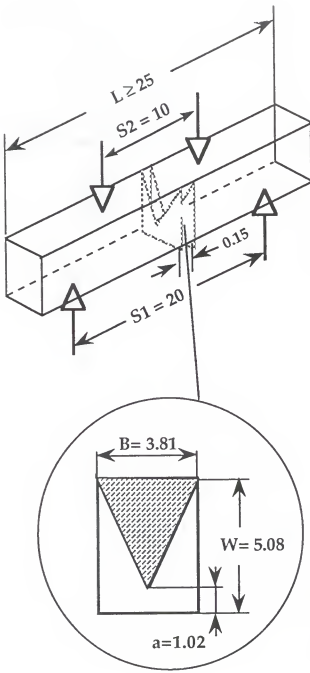


Fig. 3.4 Configuration of four point bend test on chevron notched specimens (all dimensions in millimeters).

CHAPTER 4 RESULTS AND DISCUSSION

4.1 Microstructures of the Composites

4.1.1 Monolithic MoSi₂

Typical microstructures of as-polished MoSi₂, hot pressed at temperatures between 1300-1700°C under a pressure of 40 MPa for 1 h, are shown in Fig. 4.1. It is evident that the hot pressed monolithic MoSi₂ contains second phases and/or porosities as indicated by the dark spots in Fig. 4.1. Furthermore, the size of the second phases or porosities increase with increasing processing temperature. High magnification backscattered-electron images of the microstructures processed at 1400 and 1700°C (Fig. 4.2) suggests that the dark spots in Fig. 4.1 fit into at least two categories: one is second phase particles which are solid dark areas in the figure, and the other may be porosities or second phases containing high Z elements which are dark areas with white points in them. The white points in the dark areas may come from high Z elements or from more secondary electron signals due to the rough surfaces of the porosities. Note that the MoSi₂ hot pressed at 1400°C has fewer pores or second phases containing high Z elements. Furthermore, it is noted that most of the second phases and porosities are located at the grain boundaries and triple points. For particle sizes larger than 1 μm, electron microprobe analysis indicated that the majority of these second phase particles were SiO₂ and others were Mo₅Si₃. The presence of Mo₅Si₃ and SiO₂ in the hot pressed monolithic MoSi₂ has also been confirmed using TEM technique by other investigators [158-161].

If the oxygen impurity in the commercial MoSi₂ powder is assumed to be in the silica particles, then the volume fraction of silica can be estimated to account for about

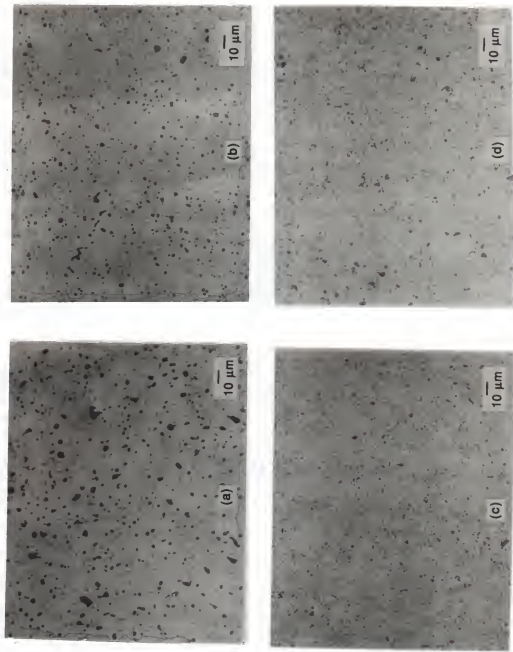


Fig. 4.1 Typical optical microstructures of as-polished MoSi₂ hot pressed at (a) 1700°C, (b) 1600°C, (c) 1400°C and (d) 1300°C with a pressure of 40 MPa for 1 hour.

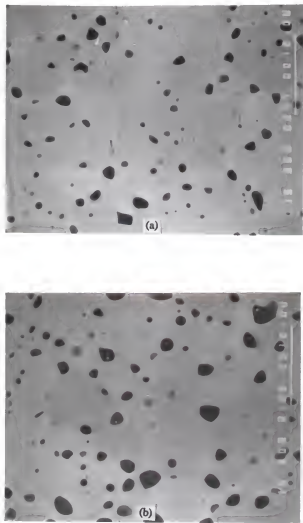


Fig. 4.2 Backscattered-electron images of MoSi_2 hot pressed at
(a) 1400°C and (b) 1700°C .

Table 4.1 Densities of hot pressed monolithic MoSi₂ measured using Archimedes' principle

Hot pressing temperature, (°C)	Density (g/cm ³)	Theoretical density (%)*
1300	5.92	97.21
1400	6.09	100.00
1600	5.89	96.72
1700	5.84	95.90

* Assuming the presence of 6 vol % SiO₂.

6 vol%. Thus, by assuming the presence of 6 vol% SiO₂ the densities of the hot pressed MoSi₂ measured using Archimedes' principle may be calculated and the results are summarized in Table 4.1. The results suggest that the highest density is achieved by hot pressing at 1400°C, consistent with the microstructural observations. The reason for decreasing density as processing temperature increases is not yet clear. The grain size of hot pressed MoSi₂ does not seem to depend strongly on the processing temperature in the temperature range studied as shown in Fig. 4.3. Instead, the second phases become coarser as processing temperature increases. Insensitivity of the grain size to the processing temperature is believed to be related to the presence of the second phases located at the grain boundaries and triple points and provide a pinning force for grain growth. Since processing at 1400°C provides the highest density, most of the composites in the present study were consolidated at this temperature.

4.1.2 MoSi₂/Uncoated Nb Interface

The microstructure and compositional profiles of a MoSi₂/uncoated Nb interface hot pressed at 1400°C are shown in Fig. 4.4. As seen in the figure, Nb and

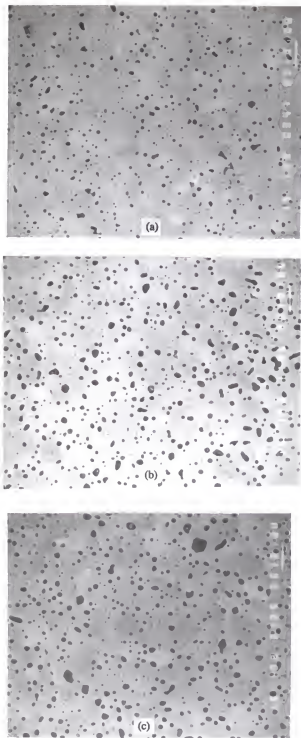


Fig. 4.3 Secondary-electron images of MoSi_2 hot pressed at (a) 1400°C , (b) 1600°C and (c) 1700°C . The corresponding density of each sample is listed in Table 4.1

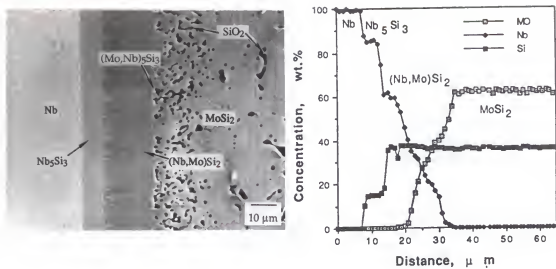


Fig. 4.4 Microstructure and composition profile across the interphase in the MoSi₂/uncoated Nb composite hot pressed at 1400°C.

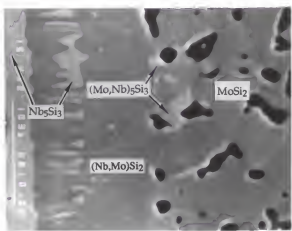


Fig. 4.5 Microstructure of (Mo,Nb)₅Si₃ at the MoSi₂/(Nb,Mo)Si₂ interface in the MoSi₂/uncoated Nb composite hot pressed at 1400°C.

MoSi_2 reacted extensively during the processing, forming three new intermetallic compounds at the interface. The resulting interaction region consisted of



However, it was found that $(\text{Mo},\text{Nb})_5\text{Si}_3$ existed in a discrete form rather than a continuous layer. Most of the $(\text{Mo},\text{Nb})_5\text{Si}_3$ phase was formed around the dark areas in Fig. 4.4 which were porosity or SiO_2 . A high magnification of $(\text{Mo},\text{Nb})_5\text{Si}_3$ microstructure at the $\text{MoSi}_2/(\text{Nb},\text{Mo})\text{Si}_2$ interface is shown in Fig. 4.5. The thickness of the interaction zone formed was measured to be about $30 \mu\text{m}$ for hot pressing at 1400°C for 1 h, and the nature of the reaction products were found to depend on the processing temperature and time. For example, Fig. 4.6 shows the interfacial microstructure and the corresponding composition profile of a MoSi_2/Nb sample which was hot pressed at 1700°C for 30 min. At this processing temperature, only one $(\text{Nb},\text{Mo})_5\text{Si}_3$ interphase was formed instead of the three intermetallics, Nb_5Si_3 , $(\text{Nb},\text{Mo})\text{Si}_2$ and $(\text{Mo},\text{Nb})_5\text{Si}_3$, formed at 1400°C .

Such temperature dependence of interphase formation can be explained in terms of Mo-Si-Nb ternary phase diagram and temperature dependence of the diffusivity of each elemental species. The available isopleth through MoSi_2/Nb [162] shows that there are two four phase equilibria, at 1730 and 1740°C , associated with MoSi_2/Nb vertical section. The isopleth [162] also shows that the relevant phase fields remain essentially unchanged below the two four phase equilibria. Therefore, the composition path in the present study can be analyzed on the basis of the 800°C isothermal section [163], which has been slightly modified by Lu et al. [164] to eliminate the Nb_4Si phase [165] and is shown in Fig. 4.7. The composition paths for hot pressing at 1400°C and 1700°C are also shown in Fig. 4.7 with line A and B, respectively. The non-planar interface of $\text{Nb}_5\text{Si}_3/(\text{Nb},\text{Mo})\text{Si}_2$ in Fig. 4.4 (hot pressed at 1400°C) suggests that the composition path crosses the corresponding two phase region by cutting across the tie lines. On the other hand, the sharp interface of $\text{Nb}/\text{Nb}_5\text{Si}_3$ indicates that the

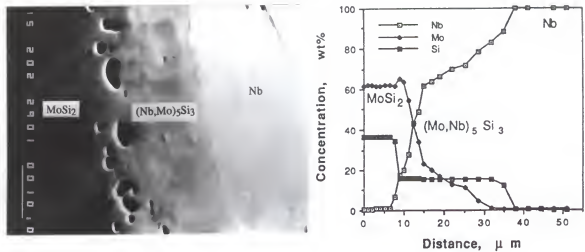


Fig. 4.6 Microstructure and composition profile across the interphase in the MoSi_2 /uncoated Nb composite hot pressed at 1700°C .

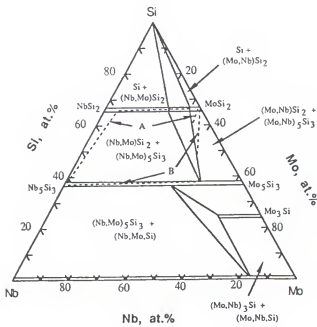
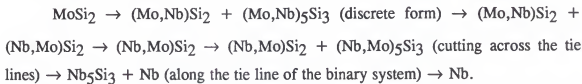
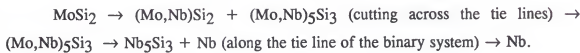


Fig. 4.7 Isothermal section of the Mo-Si-Nb ternary diagram [163] at 800°C , showing the composition path of Nb/ MoSi_2 systems. Line A is for 1400°C and line B for 1700°C .

composition path runs along the tie line in the corresponding two-phase region. Therefore, the composition path for 1400°C is shown in the following route:



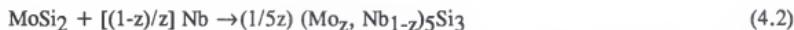
Similarly, based on the microstructure examination and composition analysis, the composition path for hot pressing at 1700°C (Fig. 4.6) is



Since the isopleth of the Mo-Nb-Si system [162] shows that the relevant phase fields remain essentially unchanged below 1730°C, the difference in the microstructures at different processing temperatures below 1730°C might be due to the changes in the interface reaction rate which is proportional to the free energy of formation of these compounds or due to changes in diffusion kinetics of the elemental species to the reaction sites. According to the phase diagram shown in Fig. 4.7, the compounds formed in the MoSi_2/Nb diffusion couple may be described, depending on whether or not $(\text{Nb},\text{Mo})\text{Si}_2$ forms, by the following formulae:



or

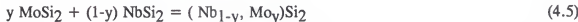


where the coefficients a , b , c , x , y and z depend on the composition and relative amounts of the products. For the above equations, it is assumed that 1 mole of MoSi_2 reacts completely with the required amount of niobium to form the compounds listed on the right-hand side of the equations. The free energy for reaction (4.1) can be calculated by considering several intermediate steps, such as the following:





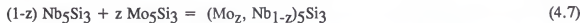
and



Similarly, equation (4.2) can be broken down into



and



Reactions (4.4), (4.5) and (4.7) correspond to the formation of the solid solutions from mixing of the pure components. Based on the available thermodynamic data [166], free energies of formation for consuming 1 mole of MoSi_2 in reactions (4.3) and (4.6) have been calculated for two different temperatures, 1400^0C and 1700^0C , and the results are listed in Table 4.2. As seen in the table, the free energies of formation for reactions (4.3) and (4.6) do not vary substantially as the hot pressing temperature increases from 1400 to 1700^0C . It should be noted that depending on the amounts of MoSi_2 and niobium participating in reaction (4.3), the ratio of the products NbSi_2 to Nb_5Si_3 may not be fixed as indicated in the equation. Other possibilities such as the formation of much more Nb_5Si_3 than NbSi_2 or a similar amount have also been considered. However, the calculations show that the same conclusion mentioned above (for the case of more NbSi_2 than Nb_5Si_3) still holds for these cases. Since no data on the free energy of mixing for reactions (4.4) and (4.7) are available, the free energy of mixing can be assumed to be ideal. This may not be an unreasonable approximation since $(\text{Mo}_x, \text{Nb}_{1-x})_5\text{Si}_3$ is a continuous solid solution as shown in Fig. 4.7. For this case, the free energy of mixing is proportional to temperature for a fixed composition. Thus, the change in the free energy of mixing for reactions (4.4) and (4.7) from 1400^0C to 1700^0C should not change the order of the free energy of formation for reactions (4.1) and (4.2). A similar argument may apply to reaction (4.5), since the isopleth of the Mo-Nb-Si system [162] shows that the relevant phase fields remain

Table 4.2 The standard free energy of formation for some possible reactions in the MoSi₂/Nb diffusion couple

Reaction	ΔG_{1400} (kcal.mol ⁻¹)	ΔG_{1700} (kcal.mol ⁻¹)
4.3	-44.46	-49.76
4.6	-37.45	-38.20

essentially unchanged below 1730⁰C, i.e., the phase relations between (Nb,Mo)Si₂, (Mo,Nb)Si₂ and (Nb,Mo)₅Si₃ remain unchanged (Fig. 4.7), implying that (Nb_{1-y}, Moy)Si₂ behaves more or less like an ideal solid solution. Thus, although the free energies of formation for reactions (4.1) and (4.2) change with temperature, the order of the free energy of formation for reactions (4.1) and (4.2) does not vary with temperature in the range of interest. Therefore, the free energy of formation of these compounds on the reaction kinetics may not explain the observed microstructural change from 1400⁰C to 1700⁰C.

In contrast, the microstructural changes in the interaction zone at different processing temperatures could be due to the change in the diffusion kinetics of Si, Nb and Mo, as will be discussed below. The composition profile in Fig. 4.4 (1400⁰C) shows clearly that Si diffuses far deeper than Mo into the Nb-rich regions, indicating that Si has a higher mobility than Mo. This is consistent with the available literature data [167,168], which show that diffusivities of Si and Mo in Nb could be expressed as follows.

$$D_{\text{Si}} = 0.51 \times 10^{-2} \exp(-48,000/RT) \quad 700 - 1500^{\circ}\text{C}$$

$$D_{\text{Mo}} = 92 \exp(-122,000/RT) \quad 1725 - 2182^{\circ}\text{C}$$

The above equations indicate that the diffusion coefficients of silicon in niobium at 1400°C and 1700°C are 2.73×10^{-9} and $2.45 \times 10^{-8} \text{ cm}^2\text{s}^{-1}$ respectively. For molybdenum, the corresponding values are 1.56×10^{-14} and $2.81 \times 10^{-12} \text{ cm}^2\text{s}^{-1}$. Because of the low mobility of Mo relative to Si, the interphase formation at 1400°C is dominated by the diffusion of Si into Nb. This is supported by the formation of Nb_5Si_3 adjacent to Nb instead of the formation of $(\text{Nb},\text{Mo})_5\text{Si}_3$. However, as temperature increases, diffusion of Mo becomes more pronounced relative to diffusion of Si because of its higher diffusion activation energy, and therefore a stronger temperature dependence of its diffusivity. Similarly, Nb diffusion becomes more competitive at high temperatures, which combined with the diffusion of Mo leads to the formation of $(\text{Nb},\text{Mo})_5\text{Si}_3$ at 1700°C , as shown in Fig. 4.6. The limited growth of $(\text{Mo},\text{Nb})\text{Si}_2$ interphase at 1700°C is probably due to the faster growth of $(\text{Mo},\text{Nb})_5\text{Si}_3$ caused by the more pronounced diffusion of Nb relative to Si at high temperature. It should be noted that at 1400°C , growth of Nb_5Si_3 depends mainly on the transport of Si through the $(\text{Nb},\text{Mo})\text{Si}_2$ layer. However, at 1700°C , as Nb diffusion becomes more pronounced, the growth of $(\text{Mo},\text{Nb})_5\text{Si}_3$ is enhanced not only in the direction of the Nb-rich region but also in the direction of the $(\text{Nb},\text{Mo})\text{Si}_2$ interphase. Thus, when the diffusion of Nb becomes competitive with respect to the diffusion of Si, the growth of $(\text{Mo},\text{Nb})_5\text{Si}_3$ is enhanced and that of $(\text{Nb},\text{Mo})\text{Si}_2$ is limited.

Note that according to the conservation of mass, much more $(\text{Mo},\text{Nb})_5\text{Si}_3$ should exist in the diffusion couple. However, only small amount of $(\text{Mo},\text{Nb})_5\text{Si}_3$ has been observed, as shown in Fig. 4.4. This is believed to be due to the presence of SiO_2 in the commercial MoSi_2 powder as shown in Fig. 4.4 and reported in References 158 - 161. The presence of SiO_2 makes the actual composition of the starting MoSi_2 powder shift to the MoSi_2 -Si two phase field, instead of in the single phase MoSi_2 field. The presence of the extra silicon is also reflected in the composition profile. As shown in Fig 4.4, Matano interfaces of three elements are not at the same

position, with the Si Matano interface far more closer to the Nb-rich side than that of Mo. However, the difference in the position of Matano interfaces becomes smaller at 1700⁰C, as shown in Fig. 4.6. The results suggest that the presence of SiO₂ contributes more to the diffusion process at lower temperatures, whereas at high temperatures contributions from MoSi₂ and Nb become more pronounced.

4.1.3 Chemical Compatibility of Coating Materials with Nb and MoSi₂

The chemical compatibilities of the potential coating materials (Al₂O₃, ZrO₂ and mullite) with MoSi₂ matrix and Nb reinforcement were assessed experimentally via microstructural and compositional analysis of the samples after hot pressing MoSi₂ and Nb with the coating materials. Figure 4.8 shows the micrograph and compositional profiles of the Al₂O₃/MoSi₂ interface. The sample was produced by hot pressing powder mixtures of MoSi₂ and Al₂O₃ at 1700⁰C for 40 minutes followed by annealing at 1400⁰C for 100 h. As seen in the figure, there exist two very distinctive types of interface: a relatively sharp interface with a thickness less than the distance between two consecutive scanning points of the electron microprobe (2 μm), and a relatively wide interface with a gradual change in the composition which is about 7 μm thick. The wide interface was determined to be rich in Si, Al and O, with little or no Mo, as shown in Fig. 4.8. As discussed in Section 4.1.1, the commercial MoSi₂ contains SiO₂. Consequently, it is believed that the interaction layer at the wide interface is due to a reaction between Al₂O₃ and SiO₂ impurity when both are in contact. Figure 4.9 which shows that there also exist sharp interfaces on both sides of an Al₂O₃ particle further supports this argument. The results indicate that Al₂O₃ is chemically compatible with MoSi₂ and that the presence of SiO₂ in commercial MoSi₂ powder may cause the degradation of the Al₂O₃ coating in the MoSi₂/Nb composites.

Similar results were obtained with the samples of MoSi₂-ZrO₂ and MoSi₂-mullite. For instance, the interface of MoSi₂/mullite is very sharp as shown in Fig.

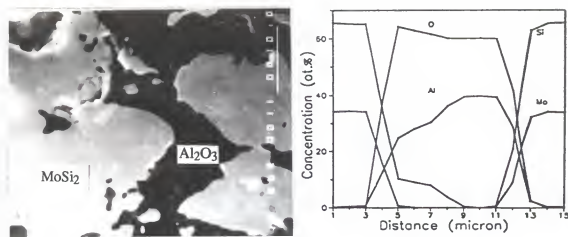


Fig. 4.8 Microstructure and composition profile across an Al_2O_3 particle in MoSi_2 matrix hot pressed at 1700°C for 40 min and annealed at 1400°C for 100 hours.

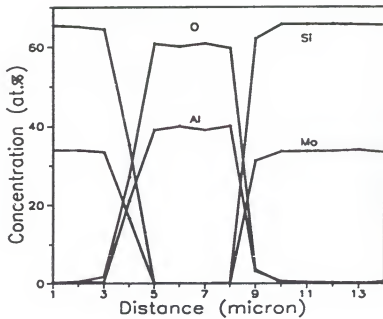


Fig. 4.9 Composition profile across an Al_2O_3 particle in MoSi_2 matrix with the same processing condition as the sample in Fig. 4.8.

4.10 and its thickness was measured to be around $1\mu\text{m}$ (the resolution limit of the microprobe). These results indicate that Al_2O_3 , ZrO_2 , and mullite are chemically compatible with MoSi_2 . The microstructures and the corresponding composition profile of $\text{Al}_2\text{O}_3/\text{Nb}$ interface are shown in Fig. 4.11. A very sharp interface (about $1\mu\text{m}$) indicates that Nb is chemically stable with Al_2O_3 up to about 1700°C .

The above findings were also confirmed by thermodynamic calculations. Using the thermodynamic data available [169], the free energy changes in possible reactions among the coating materials (Al_2O_3 and ZrO_2), MoSi_2 and Nb were calculated at 1400K and 2000K. The reaction components considered in these calculations included Mo, MoSi_2 , Mo_5Si_3 , Mo_3Si , MoO(g) , MoO_2 , $\text{MoO}_3(l)$, Si, SiO(g) , SiO_2 , Al, Al_2O_3 , AlO(g) , $\text{Al}_2\text{O(g)}$, Zr, ZrO_2 , ZrO(g) , Nb, NbO , NbO_2 , Nb_2O_5 , ZrSi_2 , ZrSi , Zr_5Si_3 , Zr_2Si , and $\text{O}_2(g)$ and all the compounds were assumed to be stoichiometric. Table 4.3 summarizes some reactions which have lower standard free energy changes among the possible reactions. It is clear from Table 4.3 that Al_2O_3 and ZrO_2 are chemically stable with MoSi_2/Nb system within the temperature range considered.

However, it was found that mullite is not chemically compatible with Nb, as shown in Fig. 4.12. Severe interaction was observed and the interaction zone was measured to be about $10\mu\text{m}$ at the as-hot pressed condition. The reaction products, however, could not be determined because of the fine microstructure (smaller than $1\mu\text{m}$) in the interaction zone as shown in Fig. 4.12. Nevertheless, the result clearly shows that mullite could not be used as a diffusion-barrier coating in MoSi_2/Nb composite.

4.1.4 Effectiveness of the Inert Coating as a Diffusion Barrier

The microstructure and composition profiles of the ZrO_2 uncoated Nb/MoSi_2 interface which was vacuum hot pressed at 1700°C for 40 minutes are shown in Fig. 4.13. It is noted that the thickness of the interaction zone between Nb and MoSi_2 has

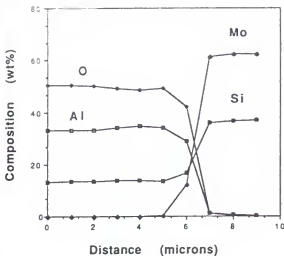
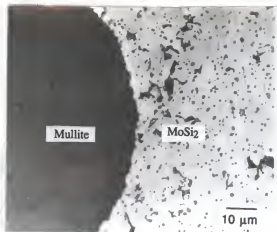


Fig. 4.10 Microstructure and composition profile across an mullite/MoS₂ interface hot pressed at 1700°C for 40 min.

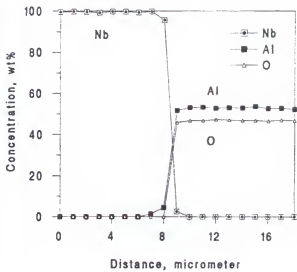


Fig. 4.11 Microstructure and composition profile across an Nb/Al₂O₃ interface hot pressed at 1700°C for 40 min.

Table 4.3 The standard free energy changes for some possible reactions among the coating materials, matrix and reinforcements.

Reactions	ΔG_{1400K} (kcal)	ΔG_{2000K} (kcal)
$\text{MoSi}_2 + 5/6 \text{ZrO}_2 = 5/6 \text{Zr} + 2/6 \text{Mo}_3\text{Si} + 10/6 \text{SiO(g)}$	102.338	62.021
$\text{MoSi}_2 + 7/5 \text{ZrO}_2 = 7/5 \text{Zr} + 1/5 \text{Mo}_5\text{Si}_3 + 7/5 \text{SiO}_2$	76.964	74.266
$\text{MoSi}_2 + 4 \text{ZrO}_2 = 2 \text{Zr}_2\text{Si} + \text{MoO}_2 + 3 \text{O}_2(\text{g})$	646.815	569.275
$\text{Nb} + 1/2 \text{ZrO}_2 = \text{NbO} + 1/2 \text{Zr}$	29.28	27.799
$\text{Nb} + 5/4 \text{ZrO}_2 = 1/2 \text{Nb}_2\text{O}_5 + 5/4 \text{Zr}$	94.664	89.586
$\text{MoSi}_2 + 5/9 \text{Al}_2\text{O}_3 = 10/9 \text{Al} + 1/3 \text{Mo}_3\text{Si} + 5/3 \text{SiO(g)}$	99.396	54.509
$\text{MoSi}_2 + 7/5 \text{Al}_2\text{O}_3 = 14/5 \text{AlO(g)} + 1/5 \text{Mo}_5\text{Si}_3 + 7/5 \text{SiO(g)}$	341.994	237.263
$\text{MoSi}_2 + 7/5 \text{Al}_2\text{O}_3 = 7/5 \text{Al}_2\text{O(g)} + 1/5 \text{Mo}_5\text{Si}_3 + 7/5 \text{SiO}_2$	125.433	86.435
$\text{Nb} + 5/6 \text{Al}_2\text{O}_3 = 5/3 \text{Al} + 1/2 \text{Nb}_2\text{O}_5$	90.096	78.318
$\text{Nb} + 1/2 \text{Al}_2\text{O}_3 = 1/2 \text{Al}_2\text{O(g)} + \text{NbO}$	46.590	32.145

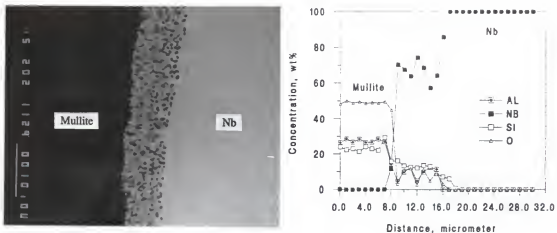


Fig. 4.12 Microstructure and composition profile across an Nb/mullite interface hot pressed at 1700°C for 1 hour.

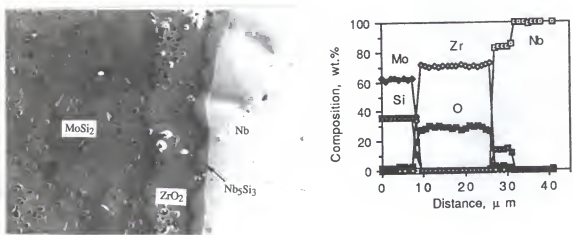


Fig. 4.13 Microstructure and composition profile across the MoSi₂/ZrO₂-coated Nb interface hot pressed at 1700°C for 40 min.

been reduced from about 30 μm for the uncoated Nb (Fig. 4.6) to 4 μm upon coating of Nb with ZrO_2 . In addition, the reaction product at the Nb/ ZrO_2 interface was determined to be Nb_5Si_3 , instead of $(\text{Mo},\text{Nb})_5\text{Si}_3$ for the uncoated samples. Furthermore, no appreciable diffusion of Nb and Mo across the coating was detected, as indicated by the Nb and Mo composition profiles in Fig. 4.13.

The growth rate of the interaction layer (Nb_5Si_3) in the ZrO_2 coated Nb filament reinforced composites were determined by annealing the samples for 25 and 100 hours at 1300°C . As shown in Fig. 4.14, the thickness of Nb_5Si_3 was increased to 6 μm after annealing for 100 hours. The thickness was also found to fit into a parabolic function of the annealing time. The results indicate that the growth of the Nb_5Si_3 layer is controlled by the diffusion of the elemental species through the Nb_5Si_3 rather than the diffusion of Si through ZrO_2 . In other words, the diffusion of Si is relatively fast through ZrO_2 . Thus, the ZrO_2 coating may not be an effective diffusion barrier for Nb/ MoSi_2 system because of the high Si diffusivity, even though it is chemically compatible with Nb and MoSi_2 .

Similar observations were made for the Al_2O_3 sol-gel coated Nb/ MoSi_2 interface. Typical composition profiles and microstructure at the Nb/ $\text{Al}_2\text{O}_3/\text{MoSi}_2$ interface produced by hot pressing at 1400°C for 1 h are shown in Fig. 4.15. Similar to the ZrO_2 coated Nb, the formation of Nb_5Si_3 at the Nb side of the Nb/ Al_2O_3 interface was observed. Its thickness was measured to be around 15 μm , compared with 30 μm of $(\text{Mo},\text{Nb})_5\text{Si}_3$ formed with uncoated Nb in composites produced under the same hot pressing conditions. These experimental observations indicate that the diffusivities of Si in ZrO_2 and Al_2O_3 must be relatively high compared with diffusivities of other species.

An order of magnitude calculation of Si diffusivity through ZrO_2 and Al_2O_3 coatings made from the thickness of the intermetallics formed indicated that the apparent diffusivity of Si was larger than $1.0 \times 10^{-9} \text{ cm}^2/\text{sec}$ in ZrO_2 at 1300°C and

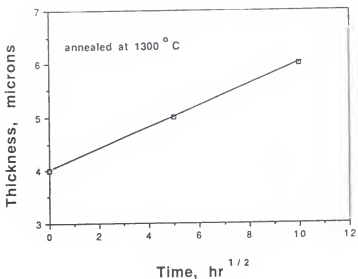


Fig. 4.14 The thickness of Nb₅Si₃ vs the square root of the annealing time in MoSi₂/ZrO₂-coated Nb composites.

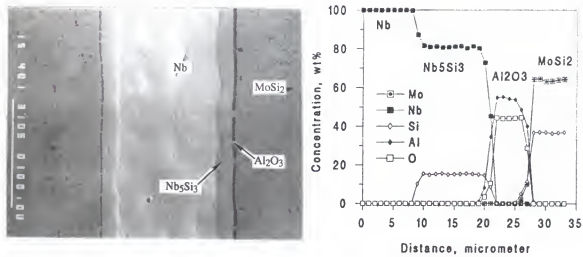


Fig. 4.15 Microstructure and composition profile across the MoSi₂/Al₂O₃-coated Nb interface hot pressed at 1400°C for 1 hour.

larger than $2 \times 10^{-8} \text{ cm}^2/\text{sec}$ in Al_2O_3 at 1400°C . These values are considerably higher than the bulk diffusion of Si in these ceramic materials, suggesting that Si diffusion might have occurred via different diffusion paths than bulk diffusion. The most feasible fast diffusion route may be through the grain boundary. Since the grain size of the coating produced by the sol-gel technique is small, the diffusion flux from grain boundary diffusion may dominate the diffusion process because of the large grain boundary area. Another potential fast diffusion path is the free surface generated by the porosities in the coating. The porosities may also provide a probable path for gaseous diffusion of SiO . Therefore, for these coating materials to be used as diffusional barriers, grain boundary area and processing defects must be minimized. In the next section, it will be shown that the effectiveness of the coating as a diffusion barrier indeed depends strongly on the processing techniques and the process control parameters.

4.2 Optimization of Coating Processes

From Section 4.1, it is clear that Al_2O_3 and ZrO_2 are chemically compatible with both MoSi_2 and Nb. However, ZrO_2 has a much higher thermal expansion coefficient than MoSi_2 and Nb. This may cause a very low interfacial fracture energy owing to the thermal expansion mismatch between the coating and the matrix and reinforcement [170]. In contrast, Al_2O_3 has a thermal expansion coefficient close to those of both MoSi_2 and Nb. Thus, it has been chosen as the coating material for the present composite system. In the following sections, three different coating techniques for applying a thin Al_2O_3 film on Nb reinforcement will be discussed. The techniques consist of (i) sol-gel coating; (ii) physical vapor deposition; (iii) hot dipping the metal in molten Al, followed by anodizing Al to form Al_2O_3 . It will be shown that the effectiveness of the coating as a diffusion barrier depends strongly on the processing techniques and the process control parameters.

4.2.1 Coating via Sol-Gel Technique

The microstructures of electrophoretically sol-gel coated Nb/MoSi₂ interface with different processing conditions are shown in Fig. 4.16. As seen in the figure, the coatings have degraded during the processing and have become discontinuous, thus allowing for direct contact and interdiffusion between Nb and MoSi₂ in the discontinuous regions. The degradation of the coating is likely partially due to the presence of SiO₂ in the commercial MoSi₂ powder. As discussed in Section 4.1.1, the as-received MoSi₂ powder contains SiO₂ and Mo₅Si₃, most of which end up at triple points and grain boundaries after consolidation. Experimental results in Section 4.1.3 suggested that Al₂O₃ may react with SiO₂ present in the commercial MoSi₂ powder. Therefore, the degradation of the coating at the present case is likely due to the reaction between the Al₂O₃ coating and SiO₂ particles at the region where the two are in contact. Another reason for the breakdown of the continuous coating could be due to cracking during drying and firing of the gel. It was found that when the coating was thick, as in the cases of Fig. 4.16 (b) and (c), cracking occurred more readily during drying and firing in the furnace or even during the air drying for the case of Fig. 4.16 (c). The addition of glycerol prevented cracking somewhat when the coating was thin, but not when it was thick. Thus, the discontinuity of the coating is primarily attributed to the attack of SiO₂ in the case of thin coatings and additional cracking during the drying and firing in the case of thick coatings.

Notwithstanding the above mentioned localized attack, the application of the coating reduced the thickness of the interaction layer between Nb and MoSi₂, e.g., from ~ 30 µm for uncoated samples shown in Fig. 4.5 to ~ 15 µm for the coated samples shown in Fig. 4.16. In addition, it could be seen from Fig. 4.16 that the thickness of the oxide coating increased with decreasing the ratio of water to ASB. This result suggests that the higher the concentration of ASB, the higher the rate of the build-up of hydrated aluminum hydroxide, i.e., AlO(OH) which is positively surface-

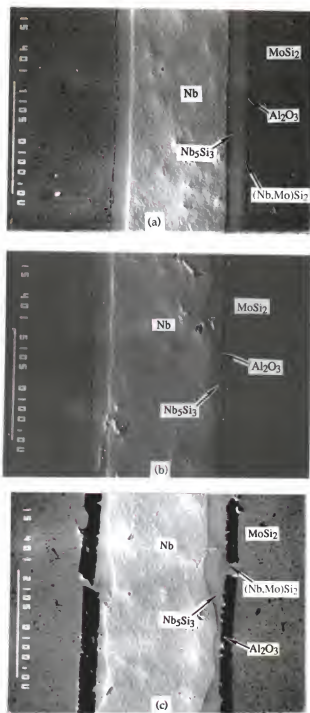


Fig. 4.16 Microstructures of MoSi_2 /sol-gel coated Nb interfaces hot pressed at 1400°C , 40 MPa for 1 hour. The coatings were produced via electrophoresis with the ratios of $\text{H}_2\text{O} : \text{ASB}$ and $\text{Al}(\text{NO}_3)_3 : \text{ASB}$ in the sols being (a) 100 : 1 and 0.04 : 1, (b) 50 : 1 and 0.04 : 1 and (c) 25 : 1 and 0.04 : 1, respectively.

charged with a formula of $\text{AlO(OH}_2\text{)}^+$, on the niobium surface. Furthermore, it was found that if the coating was thick and dense enough, the diffusion of Si across the coating could be minimized. An example is provided in Fig. 4.17 which was taken from a region where there was a relatively long continuous alumina coating. The coating in the figure was obtained via electrophoresis using SG5 sol (Table 3.2) with a DC voltage of 1 volt. As seen in the figure, the thickness of the interaction region has been drastically reduced to $\sim 1 \mu\text{m}$ from $\sim 30 \mu\text{m}$ for the uncoated samples. The reaction product of the electrophoretically coated samples could not be determined because the thickness of the interaction zone was close to the beam size of the electron microprobe ($1 \mu\text{m}$). Nevertheless, the result clearly indicates that if the coating is dense enough and continuous, the diffusion of Si can be effectively limited.

In an effort to further establish the effect of the coating quality on the elemental diffusion and interfacial interaction, the following experiments were conducted. The experiments involved making alumina laminae using tape casting technique, sintering the tape, placing the sintered tape in between the MoSi_2 and Nb laminae, and hot pressing them at 1400°C for 1 hr. The pre-sintering of the alumina was conducted at 1400°C for 1 hour with a heating rate of $3^\circ\text{C}/\text{min}$. Fig. 4.18 shows the result of the experiment. As seen in the figure, the Si diffusion has been totally eliminated, suggesting that if the oxide layer is thick and dense, the interdiffusion and interphase formation can be prevented thoroughly.

The above discussion suggests that as the thickness of the coating increases, the ability of the coating to retard Si diffusion increases. In addition, for the present composite system which contains SiO_2 , a thick and dense coating is necessary to defend the attack of SiO_2 . Thus, it seems that a low water/ASB ratio to produce a thick coating is more favorable. However, there is a lower limit to the water/ASB ratio below which bulk gelation occurs readily and AlO(OH)^+ hardens, not responding to the electric field [171]. Therefore, there is an optimum ratio which allows for an

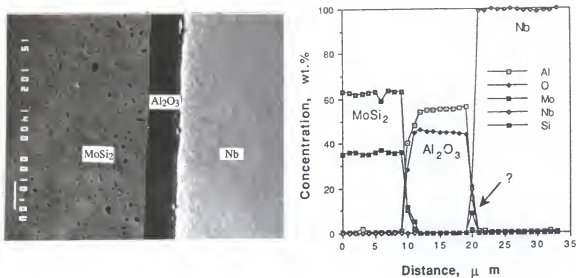


Fig. 4.17 Microstructure and composition profile of a MoSi_2 /sol-gel coated Nb interface, hot pressed at 1400°C , 40 MPa for 1 hour. The coating is obtained using SG5 sol (Table 3.2) with a DC voltage of 1 volt.



Fig. 4.18 Interfaces of MoSi_2 /pre-sintered Al_2O_3 tape/Nb compact, hot pressed at 1400°C , 40 MPa for 1 hour.

adequate thickness of the coating without bulk gelation. For the present study, this ratio was found to be 25:1, indicated as the solution SG5 in Table 3.2. However, the cracking problem associated with the thick coating still presents a formidable processing challenge which is yet to be solved.

No obvious effect of the ratio of aluminum nitrate to ASB on the quality and thickness of the coating was observed for the two ratios investigated in the present study. Finally, the Al_2O_3 coating formed using dip-coating technique was found to be thinner and more porous than that produced with electrophoresis technique.

4.2.2 Coating via Physical Vapor Deposition.

The microstructures of MoSi_2 plates diffusion-bonded to PVD coated Nb with different thicknesses of the alumina coating are shown in Fig. 4.19. Interphase formation was detected in all cases. However, the thickness of the interaction zone was reduced dramatically from $\sim 30 \mu\text{m}$ for uncoated samples (Fig. 4.5) to 15, 5 and $1 \mu\text{m}$ for PVD coated samples with a coating of 1, 2 and 3 μm thicknesses, respectively. The result clearly indicates that the thickness of the interaction zone decreases with increasing thickness of the coating, a trend also observed with sol-gel coatings. Detailed examination of Fig. 4.19 also reveals that degradation of the oxide coating occurs in all cases, but is quite localized, as can be seen clearly in Fig. 4.19(c). Since the degradation is not an overall problem of reaction between Al_2O_3 and MoSi_2 , but a localized attack, it is again most likely due to the presence of SiO_2 . It should be noted that the breakdown of the coating is not due to the damage by MoSi_2 particles during the processing. This can be illustrated using Fig. 4.20 which compares the interfaces produced with different processing conditions. Figure 4.20(a) was obtained by hot pressing the coated Nb with MoSi_2 powder directly, and Fig. 4.20(b) by hot pressing the coated Nb with the pre-sintered and polished MoSi_2 plates. It is clear that the

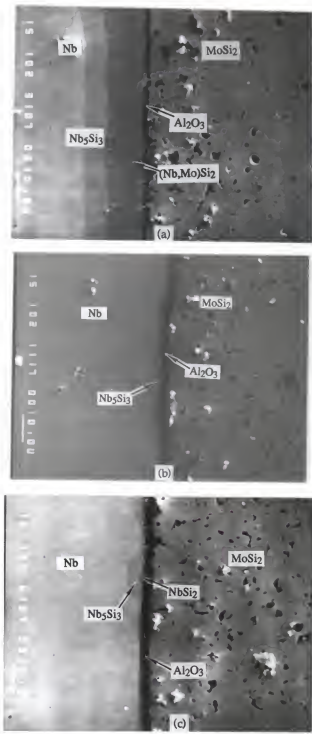


Fig. 4.19 Microstructures of MoSi₂/PVD coated Nb interfaces, hot pressed at 1400°C, 40 MPa for 1 hour. (a) 1 μm Al₂O₃ coating; (b) 2 μm Al₂O₃ coating; (c) 3 μm Al₂O₃ coating.

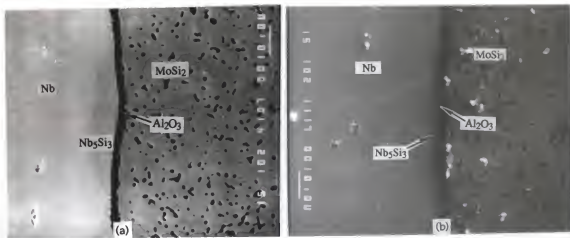


Fig. 4.20 Effect of the contact of the thin oxide coating with MoSi_2 powder and plates on the integrity of the coating. (a) the coating in contact with the powder; (b) the coating in contact with the pre-polished plate. (Hot pressed at 1400°C , 40 MPa for 1 hour.)

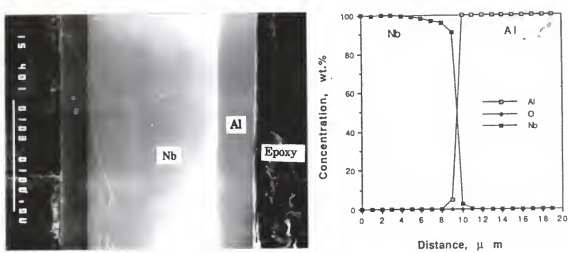


Fig. 4.21 Microstructure and composition profile of Al/Nb interface in a hot dipped Nb sample. The temperature of the molten bath is 930°C and dipping time is 2 min.

coating characteristics using MoSi_2 powder are similar to those of using pre-sintered and polished MoSi_2 plates.

Comparing the results of PVD coating and sol-gel coating indicates that the former technique produces a much denser Al_2O_3 on Nb than the latter one; in the case of sol-gel coating the interphase thickness was reduced to $\sim 1 \mu\text{m}$ only when the coating thickness reached $\sim 10 \mu\text{m}$. For the PVD coating, the same reaction zone thickness was observed when the coating thickness was $\sim 3 \mu\text{m}$. The reduction in the zone thickness is directly related to the density of the coatings produced. For PVD, the oxide compound is transformed to the vapor state which then packs on the surface of Nb. In contrast, sol-gel coating involves a large volume shrinkage associated with the crystallization of the gel, leading to the formation of pinholes, porosity or cracks in the coating.

4.2.3 Coating via Hot Dipping and Anodizing.

A typical microstructure and compositional profiles of Al/Nb interface in a Nb sample hot dipped in a molten aluminum bath at 930°C for 2 minutes are shown in Fig. 4.21. As can be seen, the hot dipping process produced a sharp Al/Nb interface with a thickness of $\sim 1 \mu\text{m}$. The compositional analysis also shows negligible interdiffusion between Al and Nb during the dipping operation. In addition, the interface is very clean and no oxygen is detected at the interface by the compositional analysis, as shown in Fig. 4.21. The thickness of the aluminum coating ranged from $25 \mu\text{m}$ to $40 \mu\text{m}$. Hot dipping at 870°C for 5 minutes showed a similar result except that the uniformity of the coating was reduced.

Figure 4.22 shows the microstructure and composition profile of the coating after being anodized with a current density of $\sim 14 \text{ mA/cm}^2$ for 30 min. As seen in the figure, aluminum has been converted to alumina and the thickness of the coating has been reduced from $\sim 30 \mu\text{m}$ to $\sim 10 \mu\text{m}$ during the anodizing process. Moreover, the interface remains clean and sharp after the anodizing. It was found that the anodizing

Table 4.4 Thickness of Al_2O_3 layer as a function of the current density during the anodizing of pure Al plates.

Current density (mA/cm ²)	Anodizing time (minute)	Thickness (μm)
5 - 7	30	- 2
8 - 10	30	- 5
12 - 14	30	- 10
23 - 25	30	- 25

time and current density had a profound influence on the thickness of the Al_2O_3 formed, as given in Fig. 4.23 and Table 4.4. Fig. 4.23 shows the variation with time of the current density and thickness of the alumina formed for anodizing pure aluminum plates (99.999 wt%) under a constant voltage. As expected, the thickness of the alumina increases with time rapidly at the early stage of anodizing, but it slows down after a certain period of time (about 30 min), suggesting that the alumina approaches a limit thickness asymptotically for a given voltage. Correspondingly, the current density decreases rapidly at the early stage of the anodizing, and levels off when the alumina becomes thick. The effect of current density on the thickness of the oxide film is shown in Table 4.4. As seen in the table, increasing the current density tends to increase the limit thickness of the oxide film. The current density dependence of the limit thickness suggests that the oxide film formed dissolves in the electrolyte during the anodizing process and the limit thickness is a result of the rate of dissolution matching the rate of formation. These results are in agreement with the literature [150,172,173].

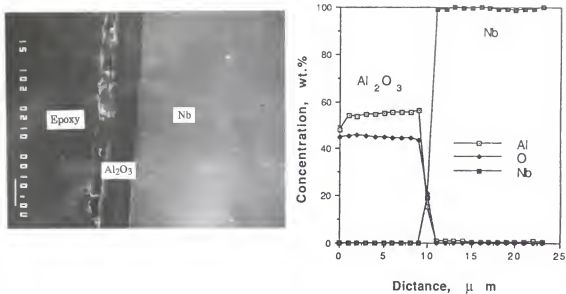


Fig. 4.22 Microstructure and composition profile of $\text{Al}_2\text{O}_3/\text{Nb}$ interface after a hot dipped Nb has been anodized with a current density of 14 mA/cm^2 for 30 min.

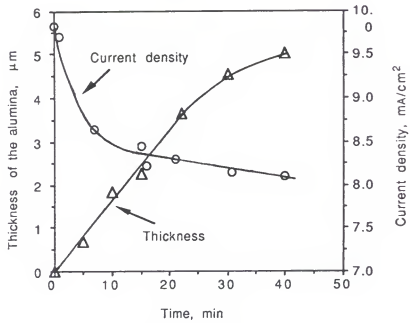


Fig. 4.23 Current density and thickness of the alumina film vs. time during the anodizing with a constant voltage.

When anodizing the hot dipped Nb, the situation was complicated by the fact that the total thickness of the coating, i.e., the (Al + Al₂O₃) layer, on the surface of Nb became thinner and thinner as anodizing proceeded because of the dissolution of the oxide in the electrolyte [173]. If the anodizing time was too long, the entire coating would dissolve, exposing interior Nb. If the anodizing time was too short, some Al remained unconverted which would reacted severely with Nb during the subsequent consolidation. Therefore, when anodizing the hot dipped Nb, it is necessary to take into account the decrease of the thickness of (Al + Al₂O₃) layer in addition to the consideration of the effect of the current density on the thickness of the Al₂O₃ film. The present study showed that for a current density of ~ 12 mA/cm² and an electrolyte with 5 wt% sulfuric acid, the rate at which the thickness of (Al + Al₂O₃) layer decreased was ~ 0.45 μm/min. Thus, knowing the thickness of Al from the hot dipping and the current density for the anodizing, it is possible to calculate the anodizing time to control the coating quality.

Figure 4.24 shows the microstructure and corresponding composition profile for a MoSi₂/anodized Nb interface. The processing condition for the Nb foil was hot dipping in the molten aluminum at 930°C for 2 min and anodizing for 45 min with a current density of ~ 12 mA/cm². As seen in the figure, the thickness of the coating is ~ 10 μm and a reasonably dense coating is formed. The thickness of the interaction region has been reduced from ~ 30 μm for the uncoated samples to ~ 4 μm for the coated samples. Note that for sol-gel coating technique, when the coating was ~ 10 μm, the interaction zone was limited to ~ 1 μm, indicating that the coating produced via sol-gel processing is denser than that produced via hot dipping and anodizing technique.

The effect of the anodizing current density on the quality of Al₂O₃ coating is shown in Fig. 4.25. The difference in processing condition for the two micrographs is that the dipped Nb was anodized with ~ 12 mA/cm² for 45 min for Fig. 4.25(a), and with ~ 20 mA/cm² for 30 min for Fig. 4.25(b). As seen in Fig. 4.25, the final

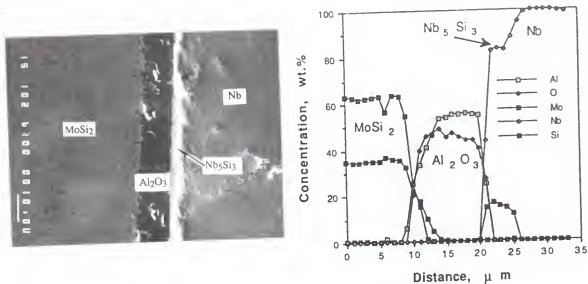


Fig. 4.24 Microstructure and composition profile of MoSi_2 /anodized Nb interface.
Processing condition: Nb foil is hot dipped at 930°C for 2 min, anodized with $\sim 12 \text{ mA/cm}^2$ for 45 min, and finally hot pressed with MoSi_2 at 1400°C , 40 MPa for 1 hour.

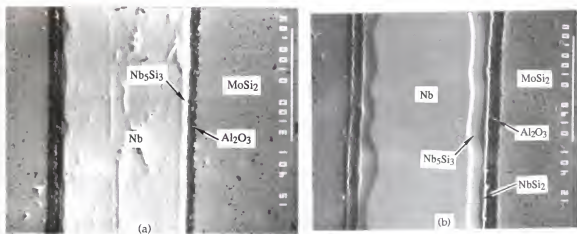


Fig. 4.25 Effect of the anodizing current density on the quality of Al_2O_3 coating, hot pressed at 1400°C , 40 MPa for 1 hour. (a) Nb foil is hot dipped at 930°C for 2 min, anodized with $\sim 12 \text{ mA/cm}^2$ for 45 min; (b) Nb foil is hot dipped at 930°C for 2 min, anodized with $\sim 20 \text{ mA/cm}^2$ for 30 min.

thicknesses of the coatings are very similar (~ 10 mm) for both processing conditions. However, the interphases formed have different thicknesses with Fig. 4.25(a) having about 4 mm and Fig. 4.25(b) about 12 mm, indicating that the oxide film formed with the condition of Fig. 4.25(b) is more porous than that formed with the condition of Fig. 4.25(a). The results imply that better coatings are produced using lower current densities. However, lower current densities tend to produce thinner oxide layers. Thus, an optimized anodizing current density is needed to produce a coating with proper density and thickness. For the present MoSi₂ matrix which contains SiO₂, it seems that a medium current density (12 - 14 mA/cm²) which produces a coating with proper combination of thickness and density would be recommended.

In conclusion, the present set of experiments has demonstrated that a thick and dense Al₂O₃ coating is effective in eliminating the interactions between MoSi₂ and Nb totally, and the best coating is provided with physical vapor deposition, followed by sol-gel technique.

4.3 Fracture Energy of the Matrix/Reinforcement Interfaces

In this section, the fracture energies of MoSi₂/Nb interfaces with and without coatings will be discussed. The relationships between processing routes, microstructures and mechanical properties of the interfaces will be explored.

4.3.1 MoSi₂/Uncoated Nb Interface

Typical interfacial microstructures of MoSi₂/Nb composites have been shown in Figures 4.4 and 4.6. When the hot-pressing temperature was 1400°C, the interfaces between the uncoated Nb and MoSi₂ was MoSi₂/(Nb,Mo)Si₂/Nb₅Si₃/Nb (Fig. 4.4), while they became MoSi₂/(Mo,Nb)₅Si₃/Nb when the hot-pressing temperature was 1700°C (Fig. 4.6). Despite the different interfacial microstructures, mechanical

behaviors were observed to be almost the same for the samples processed at the two different temperatures. Figure 4.26 shows a typical load-displacement curve of the chevron notched short bar for a MoSi₂/uncoated Nb laminated composite hot pressed at 1400°C. A stable crack propagation has been achieved, as indicated by the fluctuation in the curve near the maximum load. Therefore, the maximum load was used to calculate G_{max} with the aid of eq. (3.1). The corresponding fracture surface at the chevron crack is also presented in Fig. 4.27. By examining the two fracture surfaces of a broken short bar with scanning electron microscopy (SEM) and energy dispersive spectrometer (EDS), the failure location at the interface was determined. The results are summarized in Table 4.5. For comparison, the fracture energy of monolithic MoSi₂ measured by this method is also included in the table. It was noted that the failure of MoSi₂/uncoated Nb specimens took place inside MoSi₂ rather than at the interfaces, indicating that the interfacial region has a higher toughness than the matrix. Indeed, the value of G_{max} of MoSi₂ measured in the present study was 33.7 J/m², and all the measurements conducted on MoSi₂/uncoated Nb specimens showed a fracture energy of about 36.4 J/m² because the crack in MoSi₂ failed to follow the chevron-notched plane strictly.

The above discussion shows clearly that the failure of the notched short bar specimens does not necessarily propagate along an interface. In the following sections, more examples will be provided to show that depending on the processing conditions, the crack could propagate along an interface, by kinking between two interfaces, or only inside MoSi₂ matrix. Owing to this feature, the measured fracture energy of interface using the notched short bar has been referred to as "fracture energy of the interfacial region" of the laminates in the present study.

4.3.2 MoSi₂/Al₂O₃ Coated Nb Interface

Typical microstructures of MoSi₂/Nb interface coated with Al₂O₃ using

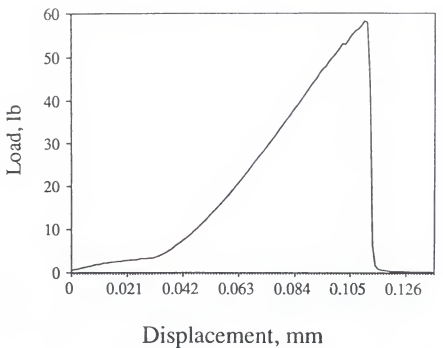


Fig. 4.26 A typical load-displacement curve of chevron notched short bar for a MoSi₂/uncoated Nb laminated composite and the corresponding fracture surface.

Table 4.5. Fracture energy and failure location of the interfacial region in the coated and uncoated Nb/MoSi₂ systems

System	Failure location	Toughness, G_{max} , J/m ²
MoSi ₂ alone		33.7 ± 1.4
MoSi ₂ /uncoated Nb	Inside the MoSi ₂	> 33.7
MoSi ₂ /Al ₂ O ₃ coated Nb via sol-gel technique	Al ₂ O ₃ /(Nb,Mo)Si ₂ interface or Al ₂ O ₃ /Nb ₅ Si ₃ interface	16.1 ± 1.3
MoSi ₂ /Al ₂ O ₃ coated Nb via hot dipping and anodizing	Al ₂ O ₃ /NbSi ₂ interface or Al ₂ O ₃ /Nb ₅ Si ₃ interface	15.5 ± 1.6
MoSi ₂ /Al ₂ O ₃ coated Nb via PVD	Partially inside the MoSi ₂ and partially at Al ₂ O ₃ /(Nb,Mo)Si ₂ interface	31.7 ± 3.4
MoSi ₂ /ZrO ₂ coated Nb	ZrO ₂ /Nb ₅ Si ₃ interface or inside the ZrO ₂	12.8 ± 1.0

different coating techniques have been presented in Fig. 4.16 (sol-gel coating), Fig. 4.19 (PVD), and Fig. 4.25 (hot-dipping-and-anodizing). For convenience, these microstructures are presented in Fig. 4.27 again. Included for comparison is also a micrograph of MoSi_2 /uncoated Nb interface.

A typical load-displacement curve of the hot-dipping-and-anodizing coated Nb/ MoSi_2 laminate and the corresponding fracture surfaces at the chevron crack are shown in Fig. 4.28. It is clear that the failure of the laminate occurred mainly along the $\text{Al}_2\text{O}_3/\text{NbSi}_2$ interface and a small portion of the failure was in the Nb_5Si_3 phase. The latter was probably due to the discontinuity of the oxide coating generated during the anodizing process and/or the roughness of the interface. Depending on the processing control parameters, the interphase formed can be only one phase, i. e., Nb_5Si_3 (Fig. 4.24 and Fig. 4.25(a)), or two phases, NbSi_2 and Nb_5Si_3 (Fig. 4.25(b) and Fig. 4.27(d)). However, the measured fracture energies of the interfacial region for the two cases are very similar. These results have been summarized in Table 4.5.

Fracture surface for the sol-gel coated Nb/ MoSi_2 laminate are shown in Fig. 4.29. It is noted that most of the failure occurred along $\text{Al}_2\text{O}_3/(\text{Nb},\text{Mo})\text{Si}_2$ interface, and a small portion of the failure occurred in MoSi_2 , a situation similar to the hot-dipping-and-anodizing case. Correspondingly, the specimens using the two coating techniques mentioned above exhibited a similar fracture energy of the interfacial region, as given in Table 4.5. Again, the measured fracture energies of the interfacial region for the case of only one interphase formed, i.e., Nb_5Si_3 (Fig. 4.16(b)) and for the case of two interphases formed, $(\text{Nb},\text{Mo})\text{Si}_2$ and Nb_5Si_3 (Fig. 4.16(a)), are nearly the same, as observed with the hot-dipping-and-anodizing coated specimens.

Quite different fracture surface was observed for the PVD coated specimens (1 μm thickness coating). As shown in Fig. 4.30, failure location in this case was partially in MoSi_2 and partially at the interface of $\text{Al}_2\text{O}_3/(\text{Nb},\text{Mo})\text{Si}_2$. This is believed

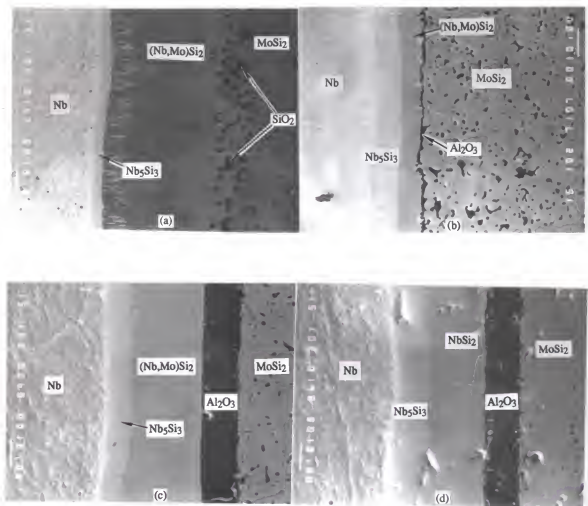


Fig. 4.27 Interfacial microstructures of MoSi_2/Nb laminated composite with different processing conditions. (a) uncoated Nb, (b) PVD coated Nb, (c) sol-gel coated Nb, and (d) hot-dipping-and-anodizing coated Nb.

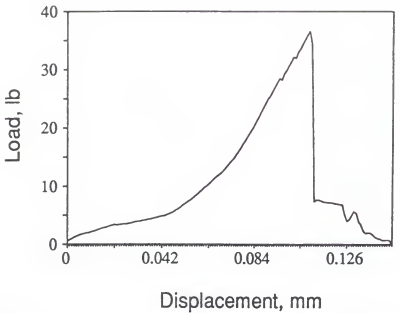


Fig. 4.28 A typical load-displacement curve of chevron notched short bar for a MoSi_2 /hot-dipping-and-anodizing coated Nb laminated composite and the corresponding fracture surfaces.

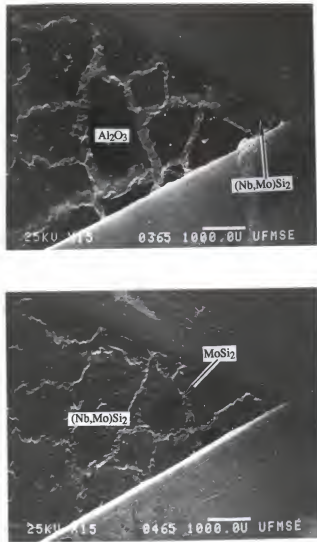


Fig. 4.29 General view of the two corresponding fracture surfaces of a broken short bar at the chevron crack for a MoSi₂/sol-gel coated Nb laminated composite.

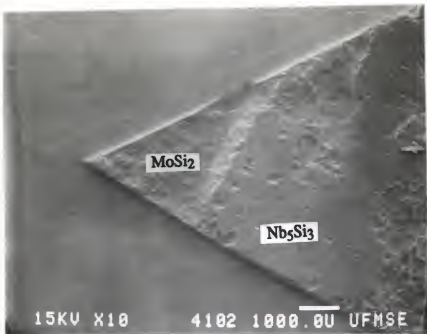


Fig. 4.30 Fracture surface at the chevron crack of a PVD coated Nb/MoSi₂ specimen.

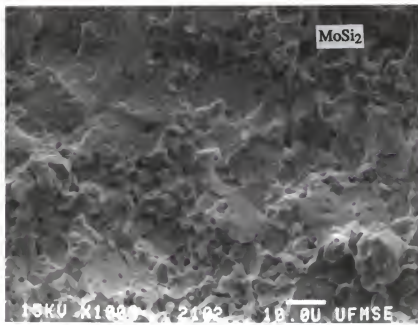


Fig. 4.31 An enlarged fracture surface of the tip area of Fig. 4.30.

Table 4.6 Fracture energy of the interfaces

System (category)	G_{max} , J/m ²
MoSi ₂	33.7
Al ₂ O ₃ /(Nb,Mo)Si ₂ (I)	~ 16
Al ₂ O ₃ /NbSi ₂ (I)	~ 16
Al ₂ O ₃ /Nb ₅ Si ₃ (I)	~ 16
Al ₂ O ₃ /MoSi ₂ (I)	> 16 ?
MoSi ₂ /(Nb,Mo)Si ₂ (II)	> 33.7
Nb ₅ Si ₃ /(Nb, Mo)Si ₂ (II)	> 33.7
Nb ₅ Si ₃ /Nb (III)	> 33.7

to be due to the small and frequent discontinuity of the oxide coating (Fig. 4.27(b)) caused by the presence of the SiO₂ in the commercial MoSi₂ powder, as discussed in Section 4.4.2. It appears that because of such small and frequent discontinuity of the coating, the fracture resistance along the Al₂O₃/(Nb,Mo)Si₂ interface has been increased. Owing to the roughness of the interface (Fig. 4.27(b)), crack is unable to propagate along the Al₂O₃/(Nb,Mo)Si₂ interface, but have to kink between the interface and MoSi₂ matrix in order to obtain crack propagation with minimum energy consumption.

It is apparent that various interphases were formed in the present study due to the diffusion of Si, Mo and/or Nb through the coating. In order to analyze the fracture energy of the interface, the interfaces at the interfacial region have been divided into three categories, as shown in Table 4.6. Category I consists of an interface (bonding) between the oxide coating and intermetallics. Category II is composed of a bond between two intermetallics. Category III is the interfaces which have a bond between a

metal and an intermetallic. Because of the formation of the intermetallics, no direct bonding between oxide and metal was observed. By examining the failure locations and fracture energy of the interfacial region measured, the fracture energy for the interfaces present in this study can be estimated as summarized in Table 4.6.

It is noted that fracture energy for the oxide bond, category I, is lower than the bonds between two intermetallics or between a metal and an intermetallic (categories II and III). The fracture energies of the former is at a level of 16 J/m^2 in the present instance, which is even lower than the fracture energy of the alumina itself ($\sim 20 - 40 \text{ J/m}^2$). The low fracture energy of the oxide bond is attributed to the low bond strength between alumina and silicides involved. As concluded by Sutton and Feingold [174], the bond strength between oxide and other materials is directly related to the amount of interaction between the two materials, and the free energy of formation of the other materials' oxide is an important criterion in determining the interaction. Weak bonding will form when the conditions are unfavorable for the formation of other oxides. In the present case, elemental Mo, Nb and Si have a lower free energy of formation of their oxides in comparison with Al_2O_3 [175]. As such, the formation of silica, niobium and molybdenum oxides, directly or by decomposition of MoSi_2 , is unfavorable in terms of free energy change. Therefore, it is expected that the reactivity of the silicides with alumina would be very low, resulting in a low bond strength. On the other hand, if the free energy of formation is more favorable for forming other oxides instead of alumina, strong bond may form. An example is given by the work of Dalgleish et al. [176]. They found that crack always initiated in the alumina adjacent to the interface of a Al-Mg alloy bonded to an alumina. High bond strength in this case can be attributed to a much more negative free energy of formation for MgO than that of Al_2O_3 .

Moreover, the fracture energy of category I interface was found to be insensitive to the change in the composition of the silicides, as shown in Table 4.6. This is probably due to the similarity of Nb and Mo in their atomic structures. If this is

true, $\text{Al}_2\text{O}_3/\text{MoSi}_2$ interface should show similar fracture energy. However, no failure at $\text{Al}_2\text{O}_3/\text{MoSi}_2$ interface was observed in the present study. As shown in Fig. 4.27(c) and (d), one major difference of $\text{Al}_2\text{O}_3/\text{MoSi}_2$ interface from the $\text{Al}_2\text{O}_3/\text{NbSi}_2$ and $\text{Al}_2\text{O}_3/(\text{Nb},\text{Mo})\text{Si}_2$ interfaces is that the former is rougher than the latter. Such roughness of the interface can increase fracture resistance by the mechanism of interlocking and crack deflection. Thus, $\text{Al}_2\text{O}_3/\text{MoSi}_2$ interface shows a higher fracture resistance than $\text{Al}_2\text{O}_3/\text{NbSi}_2$ and $\text{Al}_2\text{O}_3/(\text{Nb},\text{Mo})\text{Si}_2$ interfaces, although their bond strengths may be similar.

Category II and III interfaces all exhibit higher fracture resistance than MoSi_2 matrix, indicating the bond strength between two intermetallics or between a metal and an intermetallic is high. In this case, crack was observed to propagate inside the MoSi_2 matrix instead of inside the interphases formed. However, this does not necessarily mean that MoSi_2 has a lower inherent fracture resistance than that of the interphases, $(\text{Nb},\text{Mo})\text{Si}_2$ and Nb_5Si_3 . It is believed that the low apparent fracture resistance of MoSi_2 in the present instance is partially related to the high porosity and SiO_2 in MoSi_2 adjacent to the interface, as shown in Fig. 4.27(a). High porosity is due to the fast diffusion of Si into Nb and segregation of vacancy onto the opening channel of MoSi_2 powder compact. In contrast, the interphases formed are very dense, as shown in Fig. 4.27. Because the pores distribute along the grain boundary of MoSi_2 , it is expected that crack would propagate along the grain boundary and an intergranular fracture results. Indeed, this is confirmed by SEM observation. Figure 4.31 shows an enlarged fracture surface of the tip area in Fig. 4.30. Therefore, low apparent fracture resistance of MoSi_2 is partially caused by the presence of porosity and SiO_2 .

4.3.3 $\text{MoSi}_2/\text{ZrO}_2$ Coated Nb Interface

The interfacial microstructure of $\text{MoSi}_2/\text{ZrO}_2$ coated Nb has been presented in Fig. 4.13 which shows that the interfacial region is $\text{MoSi}_2/\text{ZrO}_2/\text{Nb}_5\text{Si}_3/\text{Nb}$ for

$\text{MoSi}_2/\text{ZrO}_2$ coated Nb systems. A typical load-displacement curve of the chevron-notched short bar for a $\text{MoSi}_2/\text{ZrO}_2$ coated Nb laminate and the corresponding fracture surface are shown in Fig. 4.32. Again, the fluctuation in the curve near the maximum load is taken as an indication of the stable propagation of the crack. The failure location was identified as at the $\text{ZrO}_2/\text{Nb}_5\text{Si}_3$ interface or inside the ZrO_2 , and the fracture energy of the interface was measured to be 12.8 J/m^2 . These results have been included in Table 4.5 for comparison. It is noted that ZrO_2 coated Nb system has the lowest interfacial fracture energy among the systems studied. This is likely due to the existence of residual tensile stresses in the zirconia coating caused by a higher coefficient of thermal expansion of the zirconia than that of the matrix and reinforcement.

In conclusion, the experiments in this section have demonstrated that fracture energy of an interfacial region depends on the interfacial bond strength, roughness of interface and microstructure of the two component materials at the interface. Weak bond strength leads to a low interfacial fracture energy. Roughness of the interface increases the interfacial fracture energy. Porosity in one of the two component materials at the interface could lead to a low fracture energy of the interfacial region due to the crack propagation along the weak path in one of the component materials instead of along the interface.

4.4 Interactions between Cracks and Ductile Reinforcements

In this section, the crack propagation and crack-ductile reinforcement interactions at various stages of the loading will be discussed. The technique used was by unloading the chevron notched samples at various loads during four-point bending tests, followed by sectioning the unloaded samples and investigating the crack geometry. The tensile test specimens shown in Fig. 3.2 were also used to aid the investigation of the characteristics of the crack interaction with ductile reinforcements.

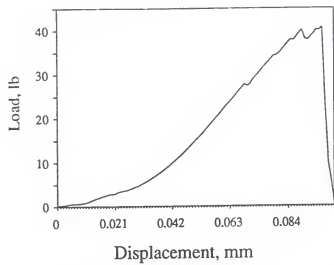


Fig. 4.32 A typical load-displacement curve of chevron notched short bar for MoSi₂/ZrO₂ coated Nb laminated composite and the corresponding fracture surface.

4.4.1 Relation between the External Load and Crack Propagation in MoSi₂/Nb Composites

Typical load-displacement curves of chevron notched specimens for a monolithic MoSi₂ and an uncoated-Nb-foil-reinforced composite are shown in Fig. 4.33. The load levels at which the specimens were unloaded are indicated by points (a) through (e) in the figure. The unloaded specimens were sectioned parallel to the crack propagation direction but perpendicular to the direction of the foil alignment, and then examined for the extent of crack propagation. Figures 4.34(a)-(e) show the nature of crack propagation in the samples at the corresponding load levels indicated in Fig. 4.33. For the sample loaded up to 15 lbs (point (a) in Fig. 4.33) which is approximately 10 % of the peak load of the composite, a crack was observed at the tip of the chevron notch, which had propagated in a stable manner as shown in Fig. 4.34(a). When the load was increased to 35 lbs (point (b) in Fig. 4.33) which is about 23% of the peak load, the result indicated that the crack had already propagated throughout the entire thickness of the matrix. This load is approximately 80 % of the peak load of the monolithic matrix. Beyond point (b), the matrix is split in two sections, and many more secondary cracks were also observed.

The extensive cracking of the matrix at a load level considerably below the peak load of the composite may be explained using the principle of strain compatibility in composite materials. During the initial loading and prior to cracking of the matrix, most of the applied load is carried by the matrix because elastic modulus of MoSi₂ matrix (380 GPa) is much higher than that of Nb foils (105 GPa). For the Nb foils to carry the same stress as the matrix does, it needs to be elongated three times more than the matrix (when there is no constraint for deformation from the matrix), which is not possible if the matrix is not cracked. Therefore, the reinforcement with a lower elastic modulus will carry a minor part of the load until a matrix crack has opened appreciably to allow for straining of the reinforcement. This has been schematically shown in Fig.

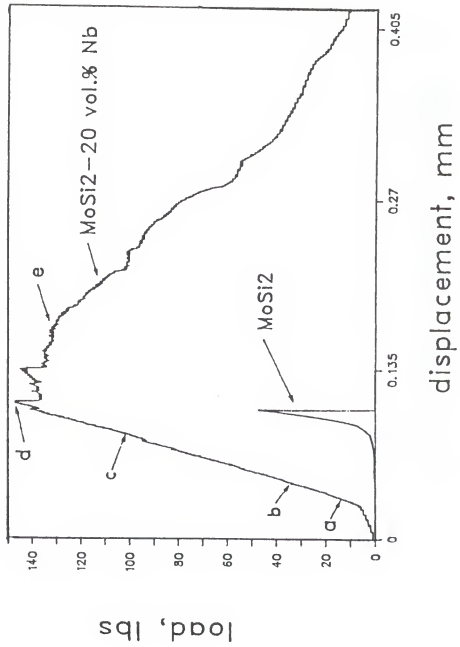
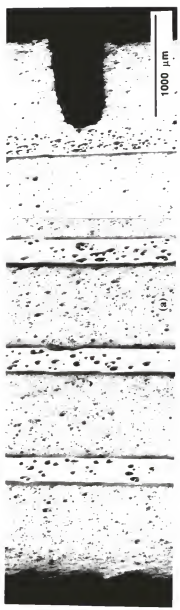
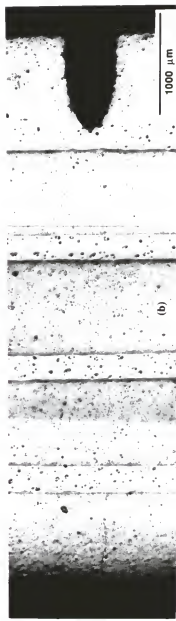


Fig. 4.33 Typical load-displacement curves of chevron-notched monolithic MoSi₂ matrix and uncoated niobium-foil-reinforced composite specimens. The letters on the composite curve indicate the approximate curve levels for the microstructures shown in Fig. 4.34.



(a)



(b)

Fig. 4.34 Caption overleaf.

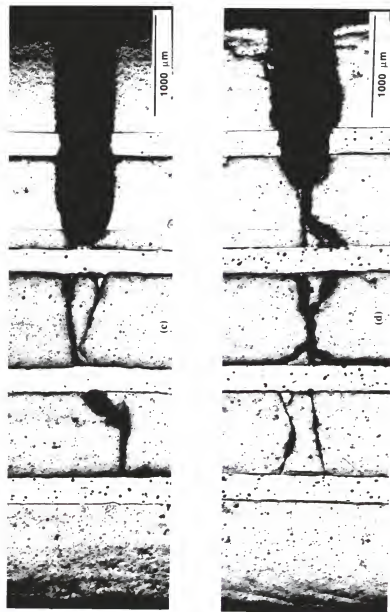


Fig. 4.34 Caption overleaf.



Fig. 4.34 The propagation of the cracks in uncoated niobium-foil-reinforced MoSi₂ composites at various load levels shown in Fig. 4.33.

2.5, where the reinforcements which are farther behind the crack tip are strained much more than the ones closer to the tip or ahead of the crack. Obviously, the required level of the crack opening for the additional straining of the reinforcement will depend on the length of debonded section of the reinforcement; the larger the debonding length, the larger is the reinforcement section which is being strained, and the larger is the required crack opening. Moreover, the latter will also depend on the relative values of the elastic moduli of the matrix and the reinforcement.

Closer examination of Fig. 4.34 reveals interesting aspects of the interaction between cracks and Nb foils in the composites reinforced by the uncoated Nb foils. At the early stages of loading, there is only one primary crack propagating in the matrix. This primary crack propagates through the matrix in a step-wise manner, instead of propagation on one crack plane (Fig. 4.34(b)). The step-wise crack propagation in the matrix may be explained through geometrical effects of the Nb reinforcement foils. In these laminated composites, as a crack ends on one side of Nb foils, it needs to reinitiate in the other side, making the crack propagation discontinuous in nature. The reinitiation plane, however, may not necessarily be on the same plane of the crack on the other side of the foil because of the existence and statistical distribution of defects in MoSi₂, which can initiate the crack. The net result is the step-wise crack propagation.

When the geometry of the Nb reinforcements is changed from foils to filaments, the crack propagation in the matrix is also expected to change. For filament reinforced composites, the crack can propagate continuously throughout the matrix without the need for reinitiation. Therefore, the crack will propagate on the plane of the maximum stress intensity and the secondary cracks are not expected to form. Fig. 4.35 shows the fractured surface of a uncoated Nb filament reinforced composite. As seen in the figure, there is no appreciable debonding at the reinforcement/matrix interface and the filaments have failed in a brittle cleavage manner. The brittle fracture of the filaments is thought to occur because of the lack of decohesion at the reinforcement/matrix interface

due to strong bonding and because of the absence of the virtual decohesion by secondary cracks as in the laminated composites. As a result, the filaments are constrained by the matrix, creating a tri-axial stress state, which leads to the brittle fracture of the filaments.

When Nb foils were coated with Al_2O_3 , the cracks in the laminated composites propagated in a manner similar to the uncoated Nb foil reinforced composites: step-wise propagation of the primary crack, extensive secondary cracking and ductile failure of Nb foils. However, when Nb foils were coated with ZrO_2 , the mode of crack propagation was found to be dependent of the processing temperature. If the hot pressing temperature was 1400°C , the crack was observed to propagate in a manner similar to the uncoated Nb foil reinforced composites. However, when the hot pressing temperature was raised to 1700°C , a different propagation mode was observed, as shown in Fig. 4.36. In this composite, there was no extensive secondary cracking and Nb foils failed in a brittle manner, even though the primary crack propagated in the step-wise manner. The brittle fracture of Nb foil is believed to be due to the embrittlement of Nb foils, as will be discussed further in the following section.

4.4.2 Behavior of Cracks at the Interface

The scenario of how cracks behave near the interface will be explored in this section. Details of cracks impinging on Nb foils for uncoated and coated composites are shown in Fig. 4.37. The micrographs were taken from the cross sections of laminated composites unloaded at about 20% of the peak load of the composites during the four-point bending tests. It is noted from the figures that debonding at the interface does not occur when a crack approaches the interface or just impinges on it for both uncoated and coated reinforcement systems. This is not surprising since all the fracture energies of the interfaces measured in the present study are higher than 1/5 of the matrix fracture energy. The observation is consistent with an estimation made by Cook and

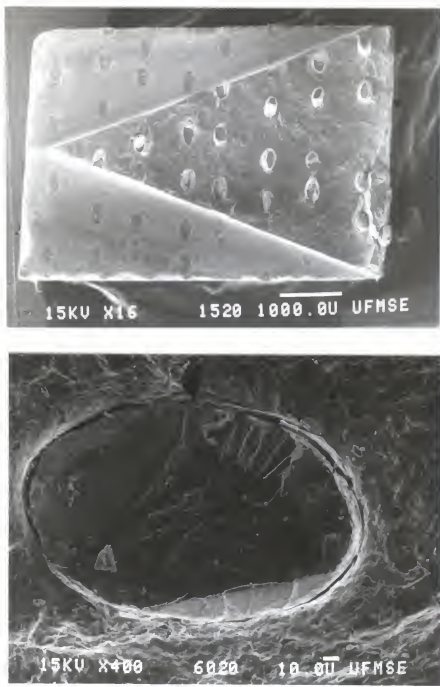


Fig. 4.35 Fracture surface of a uncoated niobium-filament-reinforced MoSi₂ composite, showing limited decohesion at the interface and brittle cleavage fracture of the niobium filament: (a) a fractured chevron-notched specimen; (b) a fractured niobium filament.

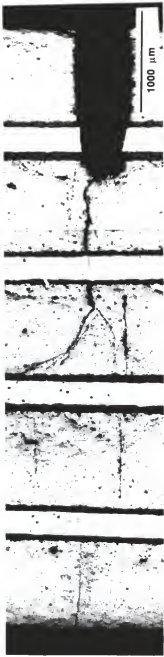


Fig. 4.36 The crack propagation in a ZrO_2 -coated niobium-foil-reinforced MoSi_2 composite. Note that the niobium foils failed in a brittle manner.

Gordon [177]. They found that, for an elliptical crack, an interfacial fracture energy of 1/5 or less of the matrix fracture energy would cause interfacial debonding in advance of the crack.

Figure 4.38 shows a typical microstructure of an uncoated Nb tensile test specimen. A notch tip can be seen at the left side of Fig. 4.38(a), which shows that a crack initiates at the notch tip and ends at the Nb foil. Fig. 4.38(b) is a close-up of one of the crack tips in Fig. 4.38(a). As seen in the figure, the impingement of the crack on the interface causes local dislocation slip of the reinforcement instead of interfacial failure, leading to the release of the stress concentration. In addition, there are also multiple cracks at the interface which add to relaxation of tip stress intensity and effectively enlarge the initial plastic zone in the ductile phase. The result shows that interfacial failure is not the only mechanism of blunting cracks in the case of ductile reinforcements. Instead, the slip capability of ductile reinforcement can play an additional and important role.

As load continues to increase during the tensile tests after the cracks have impinged on the Nb foil, debonding at the interfaces and/or multiple fracture of the matrix near the interfaces occur due to a relatively large lateral deformation of the Nb reinforcement compared to the matrix and load transfer from the matrix to the reinforcement. Typical features of debonding at the interface and multiple fracture of the matrix near the interface for the coated and uncoated specimens are shown in Fig. 4.39. It is noted that interfacial debonding has occurred at the oxide coated systems (Fig. 4.39(a)), as contrasted with multiple matrix fracture near the interface for the uncoated systems (Fig. 4.39(b)). This is in agreement with the interface fracture energy measurement since the interfaces in the uncoated composites have a higher fracture energy than the matrix, as such the matrix is expected to fail more easily than the interfaces in these composites. On the other hand, for the oxide coated composites the fracture energy of the interfaces is lower than the fracture energy of the matrix. Thus,

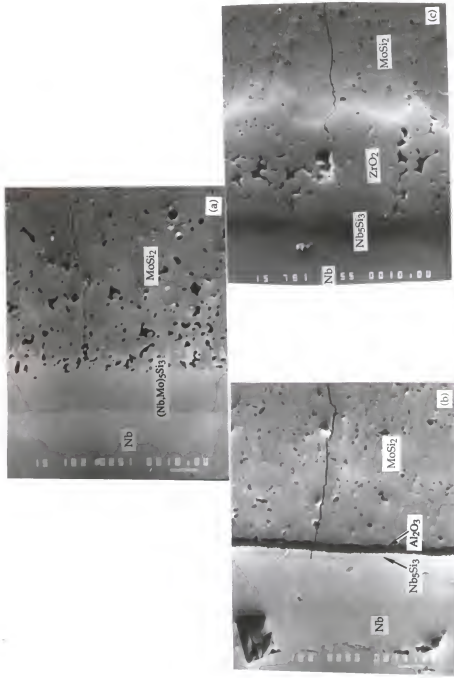


Fig. 4.37 Optical microstructures of composite laminates showing that cracks end at the front of the reinforcement without causing interfacial debonding. (a) Uncoated Nb, (b) Al₂O₃ coated Nb, and (c) ZrO₂ coated Nb reinforced composites.

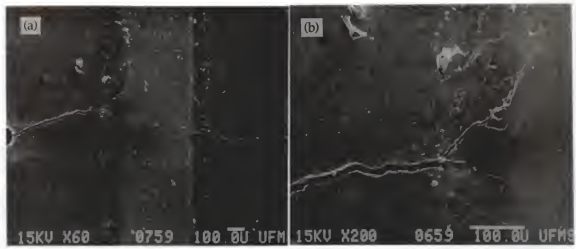


Fig. 4.38 An edge view of an unloaded tensile test specimen. (a) A general view of the cracks and (b) a close-up of the crack tips, showing dislocation slip of the Nb at the crack tips.

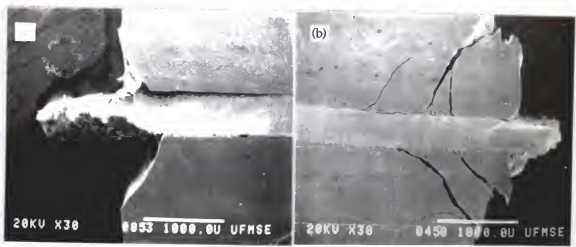


Fig. 4.39. An edge view of tensile tested specimens. (a) Debonding at the interface in a specimen with Al₂O₃ coated Nb. (b) Multiple matrix fracture near the interface in a specimen with uncoated Nb.

interfacial debonding prevailed in these composites. Similar results were also observed on bending tests of chevron notched composite laminates.

Both interfacial debonding and multiple matrix fracture create a "gauge length" at the matrix/reinforcement interface which is a region virtually free from constraints of the matrix. This region is called decohesion length in this paper. Measurement of the decohesion length was conducted for laminated composites and the results are shown in Table 4.7. Since the decohesion length of the laminated composites varies with load and position of the reinforcement, the values reported in Table 4.7 were measured at the peak load and for the second foil from the notch tip. Microhardness of the Nb reinforcements after hot pressing is also included in Table 4.7 to show how hardness of the Nb foils was affected by the processing conditions. Since little change in microhardness across the Nb foil cross section was observed, the microhardness was taken as a constant for each specific condition. The results for the specimens hot pressed at 1400°C show that the lower the fracture energy of the interface, the longer the decohesion length. This is expected since lower interfacial fracture energy means lower resistance to interfacial decohesion. However, in the case of ZrO₂ coated systems, when hot pressing temperature is increased to 1700°C, the decohesion length becomes negligible in contrast with the general trend exhibited by the composites processed at lower temperatures. Fig. 4.40 shows two typical load-displacement curves of bending tests on ZrO₂ coated Nb/MoSi₂ laminated composites hot pressed at 1400°C and 1700°C. It is noted that fracture energy of the composites is reduced and the failure becomes catastrophic when hot pressing temperature changes from 1400°C to 1700°C. Examination of fracture surfaces also shows a change of fracture modes from quasi-cleavage to cleavage, as shown in Fig. 4.41. As indicated in Table 4.7, microhardness of the Nb foils increases from 131 to 236 as the processing temperature is increased, indicating an increase in the slip resistance of the Nb foils. The embrittlement of Nb is probably due to the diffusion of interstitial oxygen into the foils

Table 4.7 Decohesion length and microhardness measured from the laminated composites reinforced with 20 vol.% of Nb foils with a thickness of 0.25 mm*

Composite System	Uncoated Nb	Al_2O_3 coated Nb	ZrO_2 coated Nb
Hot Pressing Temperature	1700°C	1400°C	1400°C
Decohesion Length (mm)	0.75 ± 0.08	0.76 ± 0.06	0.80 ± 0.12
Vickers Hardness	145	131	134
			131
			236

* Four specimens for each condition have been tested except Al_2O_3 coated Nb system for which eight specimens have been tested.

at higher processing temperature from the decomposition of ZrO₂. Loss of the ductility of the foil leads to little lateral deformation of the Nb and resultant transverse stresses, which results in negligible decohesion length. To support this inference, tensile tests on single constrained reinforcement specimens were conducted and the results showed that whenever Vickers hardness of uncoated Nb foils increased to about 200 by controlling hot pressing conditions, the fracture mode was always by cleavage even if the notches were cut directly into the Nb foils. This result shows clearly that brittle fracture of the Nb foils is due to embrittlement of the foils.

From the above discussion, it can be summarized that as a crack approaches the ductile reinforcements in these systems, there exist three competitive mechanisms: interfacial debonding, multiple matrix fracture and direct crack propagation through the ductile reinforcement. Figure 4.42 shows schematically these interactions. For the case of high ductility reinforcements, the crack is blunted by local dislocation slip of the ductile phase. The present experiments showed that extensive debonding did not occur at the early stage of the crack/ductile phase interaction, so that the interaction could be approximated as the case of no debonding at this stage. Thus, to fail the ductile reinforcement, a much higher tensile stress has to be applied which increases shear stresses at the interface due to load transfer and transverse stresses caused by the difference between lateral displacements of the matrix and reinforcement. Both shear and transverse stresses enhance interfacial debonding and/or multiple matrix fracture. Thus, whether interfacial debonding or multiple matrix fracture predominates depends on the values of the fracture energies of the matrix and interface. On the other hand, for the case of low ductility reinforcements, the crack can relatively easily propagate through the reinforcement before occurrence of the interfacial debonding or multiple matrix fracture. The decohesion length, which results from the competition of the three above mentioned mechanisms, is controlled by a combination of three material

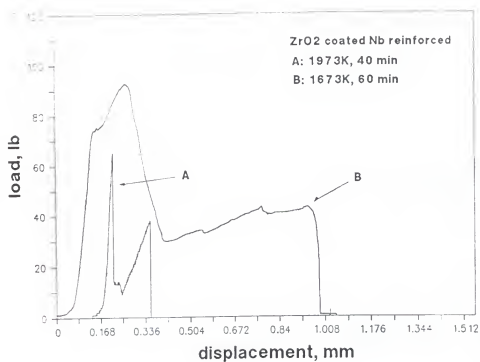


Fig. 4.40 Typical load-displacement curves of bending tests on chevron notched composite laminates reinforced by ZrO_2 coated Nb foils.

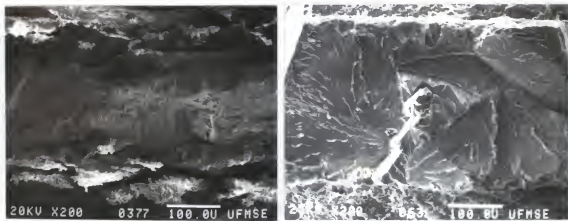


Fig. 4.41 Fracture surfaces of the Nb foils in composite laminates reinforced by ZrO_2 coated Nb, (a) hot pressed at 1400°C for 1 hour and (b) hot pressed at 1700°C for 40 min.

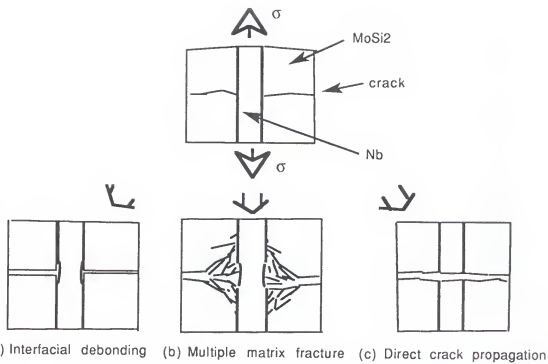


Fig. 4.42 Schematic of the three competitive mechanisms at the interface. Conditions for the process to dominate shown in (a) are high toughness reinforcement and weak interface, (b) are high toughness reinforcement and strong interface, (c) are low toughness reinforcement and strong or weak interface.

properties: interface fracture energy, toughness of the matrix and slip capability of the reinforcement.

4.4.3 Fracture Surface Observation on MoSi₂ Matrix

An overall view of the fracture surface of chevron notched specimens for the monolithic MoSi₂ is presented in Fig. 4.43. Higher-magnification views of the fracture surfaces of the monolithic MoSi₂ at different positions relative to the notch are shown in Fig. 4.44 where figures (a), (b), and (c) are taken from the positions a, b, and c shown in Fig. 4.43, respectively. As seen in the figures, intergranular fracture prevails at the tip of the notch, while transgranular fracture dominates at the bottom of the notch. Between these two positions, a transition of fracture mode is observed. Most of the visible second phases on the intergranular fracture surface (Fig. 4.44(a)) have been identified as amorphous silica, and the rest as carbon-stabilized Mo₅Si₃ particles [158]. There also exist some pores along the grain boundary, as seen on the intergranular fracture surface. The presence of the silica glass and pores weakens the grain boundary. The change in fracture mode with the position is ascribed to the different natures of crack propagation at different positions. Owing to the geometry of the V-notch, propagation of the crack is stable near the notch tip, unstable at the bottom of the notch and changes from stable to unstable at the intermediate position [178,179]. Because of these characteristics, crack propagation near the notch tip is controlled by the crosshead speed of the testing machine, and it becomes fast at the bottom of the notch. Thus, at the notch tip the crack has more time to choose the energy path which is grain boundary for the present matrix due to the presence of silica glass and pores, while at the bottom of the notch the crack propagates too fast to choose the low energy path, leading to transgranular fracture.

A general view of a typical fracture surface at the notch plane of a laminate containing 20 vol. % of Nb laminae with a thickness of 0.25 mm is presented in Fig.



Fig. 4.43 Fracture surface of a MoSi₂ chevron notched specimen.

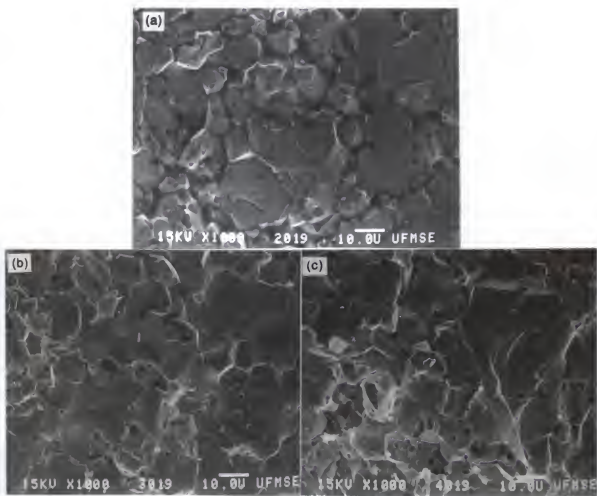


Fig. 4.44 High magnification views of the fracture surfaces of MoSi₂. Figures (a), (b) and (c) are taken from the positions a, b and c shown in Fig. 4.43, respectively.

4.45. The a, b, c, and d in Fig. 4.45 denote the positions where the fractographs of Fig. 4.46(a), (b), (c) and (d) are taken, respectively. Note that intergranular fracture again dominates at the tip of the notch, while transgranular fracture prevails at the bottom of the notch, a general trend also observed in the monolithic MoSi₂. The presence of ductile laminae makes crack propagation in the matrix become discontinuous, i. e., the crack has to stop at one side of the Nb lamina and reinitiates on the other side to continue the propagation. However, the position dependence of fracture mode of MoSi₂ in the composite laminate shows little difference from that of the monolithic MoSi₂. Such phenomena could be explained in terms of the discussion made in Section 4.4.1 where it was shown that a primary crack has already propagated through the entire MoSi₂ matrix at a load level of about 20% of the peak load in the bend test of chevron notched specimens. Therefore, the presence of Nb laminae does not have much influence on the fracture mode of MoSi₂ which fractures at the early stage of the bend test. The presence of Nb laminae, however, improves the damage tolerance of the brittle materials, as will be discussed in Sections 4.5 and 4.6.

4.5 Flow Behavior of Constrained Niobium

As discussed in Section 2.3, the primary toughening mechanism of ductile reinforcement is due to the bridging of ductile ligaments [20-26,105-107]. The ductile bridging ligaments tend to hold the crack faces together and reduce the stress intensity seen at the crack tip. Thus, the key to predict the increased fracture toughness is to calculate the clamping forces of the bridging ligaments, $\sigma(u)$, as a function of crack opening. In this section, the clamping forces of the bridging ligaments as a function of crack opening, i.e., the flow behavior of the constrained ductile phases, will be presented. The experimental procedure used has been presented in Section 3.4.



Fig. 4.45 An overall view of fracture surface of a laminated composite containing 20 vol.% of Nb laminae with a thickness of 0.25 mm. The a, b, c and d denote the positions where the fractographs of Fig. 4.46(a), (b), (c) and (d) are taken, respectively.

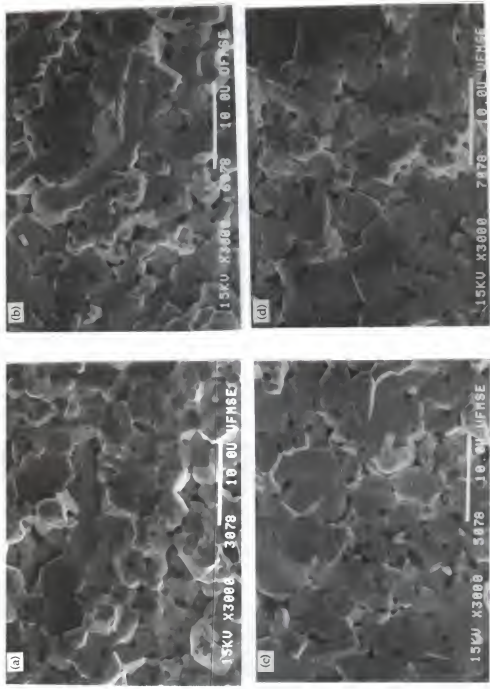


Fig. 4.46 Fracture surfaces of MoSi₂ matrix in a laminated composite. Figures (a), (b), (c) and (d) are taken from the positions a, b, c and d shown in Fig. 4.45, respectively.

4.5.1 Intrinsic Properties of Unconstrained Niobium

Mechanical properties measured from the as-received Nb have been summarized in Table 3.1. However, these properties cannot represent the intrinsic properties of niobium reinforcements embedded in the MoSi₂ matrix (called as the processed Nb in the text) because the embedded niobium have undergone the hot compaction process. Thus, the properties of the processed Nb have to be obtained if a more accurate relation between the flow behaviors of the constrained and unconstrained ductile phases is to be obtained.

To obtain the processed Nb, the following procedures has been taken: first, one layer of ZrO₂ coated Nb foil was hot pressed with MoSi₂; second, the hot pressed discs were cut into rectangular bars; and finally, the MoSi₂ on both sides of the Nb foil was broken off by mechanical means. The last step was not very difficult due to a relative weak bonding between Nb and MoSi₂ at the presence of a ZrO₂ coating layer.

The properties measured from the processed Nb are summarized in Table 4.8. Comparison between Tables 3.1 and 4.8 reveals that strength of Nb has increased after hot pressing except for the 1.0 mm Nb foils. The rate of strain hardening has also increased for all the niobium. Such changes are believed to be due to a combination of two competitive processes during hot pressing: (1) grain growth of Nb, as shown in Fig. 4.47; (2) solid solution strengthening because of its contact with the silicides formed at the matrix/reinforcement interface, as shown in Fig. 4.13. For 1.0 mm Nb foils, the grain size has changed from 15 to ~500 μm, which leads to a large decrease in strength and overshadows the increase due to the solid solution hardening. For 0.5 and 0.25 mm Nb foils, the grain size has changed from 50 to ~370 μm and from 48 to ~300 μm, respectively. However, shorter diffusion distance to the center of the niobium has made solid solution hardening dominate over the

Table 4.8. Mechanical properties of the processed Nb
(ZrO_2 coated, hot pressed at $1400^\circ C$, 40 MPa for 1 hour)*

Thickness of Nb foil (mm)	1.0	0.5	0.25
Microhardness (HV, kg/mm ²)	104	114	131
Yield strength (σ_y , MPa)	180 ± 6	211 ± 9	236 ± 11
Tensile strength (σ_u , MPa)	221 ± 8	260 ± 7	285 ± 10
Elongation (δ)	0.32 ± 0.03	0.18 ± 0.02	0.10 ± 0.02
Strength coefficient (MPa)	356 ± 11	363 ± 10	386 ± 12
Strength hardening coefficient	0.165 ± 0.032	0.085 ± 0.004	0.076 ± 0.007
σ_y/HV	1.73	1.85	1.80
σ_u/HV	2.12	2.28	2.1

* Three samples for each condition were tested.

Table 4.9 Microhardness of Nb with different processing conditions
(hot pressed at $1400^\circ C$, 40MPa for 1 hr)

Thickness of Nb foil (mm)	1.0	0.5	0.25
Processing condition	Uncoated	Al_2O_3 coated	ZrO_2 coated
HV (kg/mm ²)	104	106	104
	118	116	114
	131	134	131

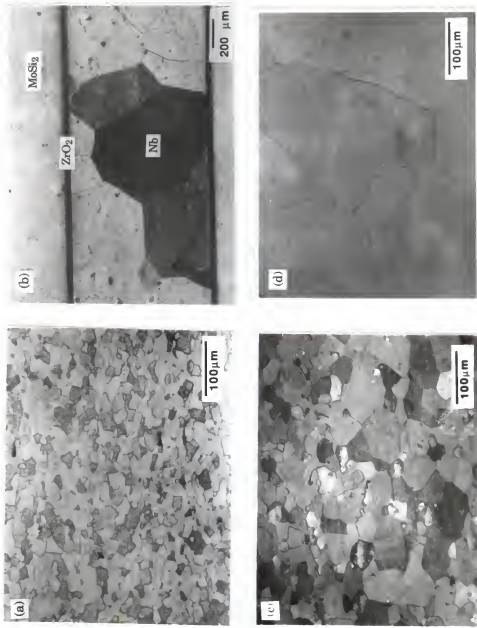


Fig. 4.47 Optical microstructures of Nb foils. (a) as-received, 1.0 mm thick; (b) processed, 1.0 mm thick; (c) as-received, 0.5 mm thick and (d) processed, 0.5 mm thick. Note that different magnifications are used.

softening due to the grain growth. Therefore, 0.5 and 0.25 mm Nb foils show an increased strength after hot pressing.

Examination of the true stress-strain data of the processed Nb indicates that as the true strain exceeds a certain value, the true stress-strain follows a power law quite well. For example, the true strain at which the true stress-strain starts to follow a power law is ~ 0.34% for 0.25 mm processed Nb, and is ~ 1.0% for 1.0 mm processed Nb. Thus, the true stress-strain data after the above mentioned strains (e.g., 0.34% for 0.25 mm Nb) have been used to calculate both the strength coefficient and the strength hardening coefficient. The results are included in Table 4.8 and also presented below for convenience.

$$\begin{aligned}\sigma_t &= 356 \varepsilon_t^{0.165} \text{ (MPa)} && \text{for 1.0 mm Nb} \\ \sigma_t &= 363 \varepsilon_t^{0.085} \text{ (MPa)} && \text{for 0.5 mm Nb} \\ \sigma_t &= 386 \varepsilon_t^{0.076} \text{ (MPa)} && \text{for 0.25 mm Nb}\end{aligned}\quad (4.8)$$

The above true stress-strain relations have been utilized to describe the intrinsic properties of the unconstrained ZrO₂ coated Nb as well as the unconstrained Al₂O₃ coated and uncoated Nb because of the following reasons. As shown in Tables 3.1 and 4.8, although the tensile strength of the niobium varies with the thickness, the tensile strength is proportional to its hardness, i.e., σ_u/HV equals to 2.48 ± 0.04 and 2.19 ± 0.08 for the as-received and processed Nb, respectively. Such relation has also been reported for other materials, especially for those that show a necking at the maximum tensile load [180]. Ratio of the yield strength to the Vicker's hardness is also approximately a constant, as shown in Tables 3.1 and 4.8. The results indicate that it is reasonable to infer the strength of the niobium from the hardness measured. Hardnesses of Nb hot pressed with different conditions are summarized in Table 4.9. The table shows that the hardnesses are almost the same for each group of Nb based on the size. Due to such hardness results, the stress-strain relations for the unconstrained uncoated and Al₂O₃ coated Nb can be assumed to be the same as that

of the processed Nb which is the ZrO_2 uncoated Nb before $MoSi_2$ on both sides of the Nb foils has been broken away.

It is clear, from the above discussion, that the intrinsic mechanical properties of the Nb reinforcement in the composites are different from those of the Nb before the processing. It is believed that such change in properties due to the high temperatures during hot compaction processing is a common phenomenon for ductile-phase-reinforced brittle matrix composites. Even in chemically compatible composites, the change of grain size will cause property change of the ductile reinforcements. Such change imposes difficulty on the prediction of the composite properties.

4.5.2 Failure Mechanism and Related Observation on Constrained Niobium

An edge view of the unconstrained and constrained uncoated Nb foils after tensile test is shown in Fig. 4.48. As seen in the figure, Nb foils fail by drawing down to a wedge for both the constrained and unconstrained conditions. All three different sizes of Nb foils show the same failure mechanism. Furthermore, similar necking was also observed for all the coated Nb hot pressed at $1400^{\circ}C$.

The decohesion lengths (defined in Section 4.4.2) measured for the tensile test specimens are summarized in Table 4.10. The data show that within each size group, decohesion length increases from the uncoated to Al_2O_3 coated and then to ZrO_2 coated Nb/ $MoSi_2$ composites. Such results are consistent with the measurement of the interfacial fracture energy, as discussed in Section 4.3 which shows that the uncoated Nb/ $MoSi_2$ has the highest interfacial fracture energy, followed by the Al_2O_3 coated and then ZrO_2 coated Nb/ $MoSi_2$ composites.

The increase of the decohesion length with the thickness of Nb foils, as shown in Table 4.10, is believed to be mainly related to the necking of the Nb. Figure 4.49 shows schematically the effect of the necking on the decohesion length. The length of

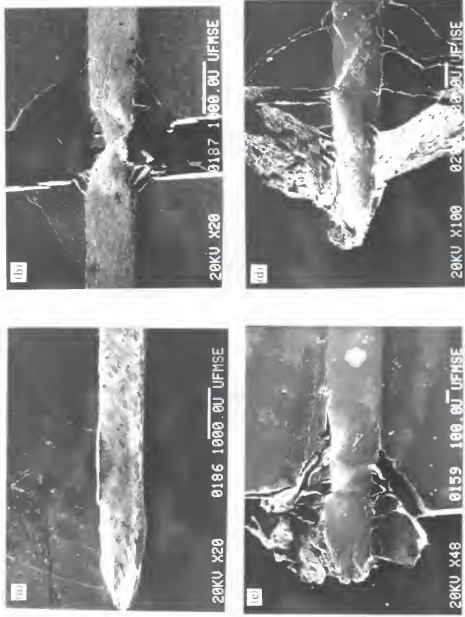


Fig. 4.48 An edge view of fractured specimens, showing contour of the neck. (a) is an unconstrained, processed Nb foil with a thickness of 1.0 mm, (b), (c) and (d) are constrained Nb with thicknesses of 1.0, 0.5 and 0.25 mm, respectively.

Note that different magnifications are used.

Table 4.10 Decohesion length in the Mo₅Si₂/Nb composites
(hot pressed at 1400°C, 40 MPa for 1 hour)*

Thickness of Nb foil (mm)	1.0	0.5	0.25	
Processing condition	Uncoated Al ₂ O ₃ coated	Uncoated ZrO ₂ coated	ZrO ₂ coated	
Decohesion length (mm)	10 ± 5	2.9±0.4 all the way to the grips.	3.3±0.4 all the way to the grips.	0.86±0.09 0.94±0.23 1.30±0.61

* Four specimens for each condition were measured except for 0.5-mm-thick Nb lamina for which eight specimens were measured.

the Nb region affected by necking, $2H$, is proportional to the thickness of the Nb, as shown in Fig. 4.48. Approximately, H is 1.3 times of the thickness of Nb, measured from Fig. 4.48. Large lateral displacement of Nb in the necking affected region gives rise to large transverse stresses which lead to the interfacial debonding and/or matrix fracture. Thus, the thicker the niobium, the longer the necking affected region, and therefore the longer the decohesion length. If the interface bonding is relatively weak, such as the Al_2O_3 and ZrO_2 coated interfaces, the transverse stresses aroused by lateral displacement of the Nb during uniform strain can be large enough to cause the interfacial debonding all the way to the test grips. During the uniform strain, the lateral displacement of Nb right at the interface is proportional to thickness of the Nb. Therefore, decohesion by this mechanism is easier to occur in thick Nb composites than in thin Nb counterparts, as indicated in Table 4.10.

It has been shown in Section 4.4 that the failure of the constrained Nb laminae in MoSi_2 matrix involves the following scenario. When an advancing crack just impinges a Nb reinforcement, no debonding at the matrix/reinforcement interface occurs. As external load continues to increase, debonding at the interface and/or multiple fracture of the matrix near the interface occurs due to a relatively large lateral deformation of the Nb reinforcement compared to the matrix and load transfer from the matrix to the reinforcement. Then, the necking and fracture of the niobium begin as the load continues to increase. Based on this observation, the flow behavior of the constrained Nb can be simplified into three stages: (1) elastic deformation; (2) plastic deformation within the decohesion region; (3) localized plastic deformation within the necking region. Three stages are illustrated in Fig. 4.50. The crack opening of the matrix can be directly related to the deformation of Nb in the decohesion zone. At the early stage of crack opening, Nb only undergoes elastic deformation, as shown in Fig. 4.50(a). As crack opening increases, Nb enters the stage of plastic deformation (Fig. 4.50(b)). At last, the work hardening rate of the

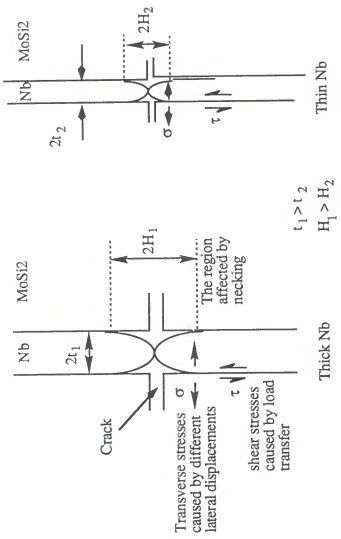
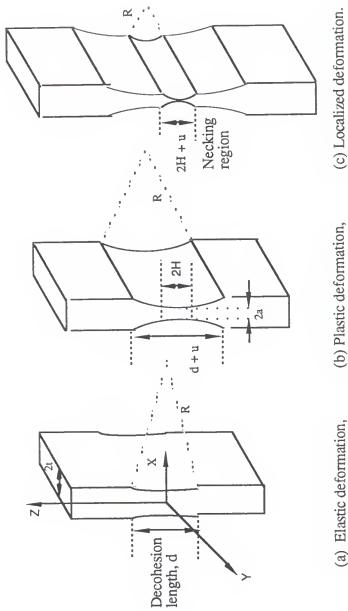


Fig.4.49 A schematic showing effect of necking on the decohesion length.



(a) Elastic deformation, (b) Plastic deformation, (c) Localized deformation.

Fig. 4.50 A schematic of three stages of deformation for constrained Nb. $2H$ is the length of the necking affected region, $2a$ is the remaining thickness of the reinforcement, and u is displacement.

niobium at the central portion of the decohesion region is lower than the stress increasing rate due to decrease in the cross section area of the reinforcement, the localized deformation begins (Fig. 4.50(c)), which leads to the final failure of the Nb lamina. Such simplified deformation processes will be used to model stress-displacement behavior of the constrained Nb, as presented in Section 4.5.4.

4.5.3 Stress-Displacement Curves of Constrained Niobium

Figure 4.51 shows typical stress-displacement curves for the uncoated Nb foils with different thicknesses constrained in MoSi₂ matrix. The parameters measured are summarized in Table 4.11. The work of rupture normalized by the yield strength, σ_0 , and half thickness of ductile phase, t , is given by

$$E_t = \int_0^{U^*} \frac{\sigma(u)}{\sigma_0} \frac{du}{t}$$

The values of E_t , called the normalized work of rupture in the text for convenience, are also included in Table 4.11. As seen in the figure and table, due to the different intrinsic properties of the niobium, the maximum stresses reached by the constrained Nb, σ_{max} , are different for different sizes of Nb. However, if the σ_{max} is normalized by its own yield strength, the normalized maximum stress, σ_{max}/σ_0 , becomes independent of the thickness of Nb. This result suggests that the maximum stress reached is not a function of size of the ductile phase. On the other hand, it is noted that the work of rupture increases with size of Nb, indicating that large size of ductile reinforcement is more effective in improving toughness of the brittle matrix composites. It is also noted that the normalized work of rupture, E_t , increases with increasing size of the niobium. The size dependency of the normalized work of rupture is attributed to the size dependency of the decohesion length, as will be discussed in Section 4.5.5. The result suggests that the data of the normalized work

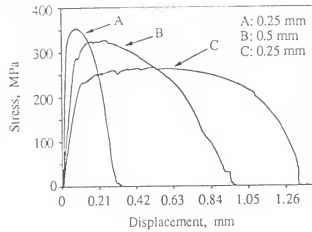


Fig. 4.51 Typical stress-displacement curves of constrained, uncoated Nb laminae with different thicknesses.

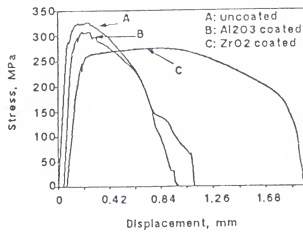


Fig. 4.52 Effect of the coatings on the stress-displacement curve, measured from composite laminates with 0.5 mm thick Nb lamina.

Table 4.11 Summary of the parameters calculated from the model and measured for the uncoated Nb/MoS₂ laminates*

2t (mm)	Measured			Calculated		
	σ_{max} (MPa)	σ_{max}/σ_0	ξ (J/m ²)	E_t	σ_{max} (MPa)	σ_{max}/σ_0
1.0	259 ± 23	1.44	477,000 ± 35,900	5.3	292	1.62
0.5	325 ± 16	1.54	239,000 ± 24,000	4.5	329	1.56
0.25	351 ± 15	1.49	85,000 ± 7,800	2.8	354	1.50

* Four specimens for each condition were tested except for 0.5-mm-thick Nb lamina for which eight specimens were tested.

Table 4.12 Summary of the parameters calculated from the model and measured from the composites with 0.5 mm thick Nb lamina*

Processing condition	Measured			Calculated		
	σ_{max} (MPa)	σ_{max}/σ_0	ξ (J/m ²)	E_t	σ_{max} (MPa)	σ_{max}/σ_0
uncoated	325 ± 16	1.54	239,000 ± 24,000	4.5	329.3	1.56
Al ₂ O ₃ coated	310 ± 11	1.47	243,000 ± 21,000	4.6	328.4	1.55
ZrO ₂ coated	275 ± 12	1.31	429,000 ± 26,000	8.1	328.2	1.55

* Eight specimens for each condition were tested.

of rupture obtained from the tests on large size of ductile reinforcements cannot be extended to small size of the reinforcements directly.

Effect of coatings on the stress-displacement curves is shown in Fig. 4.52. The parameters measured are summarized in Table 4.12. The data show that as the decohesion length increases, i.e., as the constraint on the reinforcement decreases, the work of rupture increases. This is not surprising since the longer the decohesion length, the more ductile material participates in the plastic deformation, and therefore the more energy is consumed before fracture. It is noted that as the decohesion length increases, the normalized maximum stress decreases, indicating that increasing constraints on the ductile phase increases the σ_{\max} . Table 4.12 also shows that the normalized work of rupture is dependent on the interfacial bonding strength. This is believed to be due to the increase of work of rupture with increasing decohesion length. The above results indicate that limited decohesion enhances the energy consumed to fracture the constrained ductile reinforcement, and therefore improves toughness of the composites.

4.5.4 Modeling of Flow Behavior of the Constrained Niobium

As discussed in Section 4.5.2, the flow behavior of the constrained Nb in the present study can be simplified into three stages: (1) elastic deformation; (2) plastic deformation within the decohesion region; (3) localized plastic deformation within the necking region. To model the stress-displacement relation of constrained ductile phase, $\sigma-u$, some assumptions are made. First, displacement of the stress-displacement curve is assumed to only come from the deformation of Nb lamina inside the decohesion region because the Nb outside the decohesion region is bonded to the matrix and only undergoes elastic deformation. Second, contour of the Nb lamina in the decohesion region is assumed to be part of the outside surface of a cylinder with a varied radius of R for all the stages of the deformation, as shown in

Fig. 4.50. Such an assumption is a good approximation to the real contour of the Nb observed in the experiments and makes the calculation possible. Third, plane strain is assumed for the computation in all the stages. In addition, in the calculation the value of u is measured as the axial displacement of the matrix point at the boundary of the decohesion region, while σ is computed from the total force exerted on the remaining cross section of the midplane at the neck, normalized by the original midplane area.

Stage of elastic deformation. To compute σ - u data for elastic deformation, two more assumptions are made: (1) the volume-conserving nature of large scale plastic deformation is also applicable to this stage; (2) the effective stress across the midplane of the neck is constant. Although the assumed contour and constant effective stress do not represent the real situation of the decohesion region, they introduce negligible error to the work of rupture (see the Appendix).

Based on the assumption (1) and the assumed contour, the displacement, u , can be related to the radius of the cylinder, R , by geometry as follows.

$$R = \frac{(d + u)^3}{12 tu} + \frac{4 tu}{3(d + u)} \quad (4.9)$$

From the assumption of plane strain, we have

$$\sigma_y = \mu(\sigma_z + \sigma_x) \quad (4.10)$$

where μ is the Poisson's ratio of Nb and equals 0.39 [181].

By definition, the effective stress, $\bar{\sigma}$, is written as [182]

$$\bar{\sigma}^2 = 1/2 \{ (\sigma_x - \sigma_y)^2 + (\sigma_y - \sigma_z)^2 + (\sigma_z - \sigma_x)^2 \} \quad (4.11)$$

where σ_x , σ_y , and σ_z are principal stresses because the shear stress components vanish on the midplane of the neck by symmetry [183]. Substituting eq. (4.10) into eq. (4.11), we have

$$\bar{\sigma}^2 = 0.762 \sigma_x^2 + 0.762 \sigma_z^2 - 1.4758 \sigma_x \sigma_z \quad (4.12)$$

From the boundary condition at the neck, i.e., $\sigma_x = 0$, eq. (4.12) reduces to

$$\bar{\sigma}^2 = 0.762 \sigma_{za}^2 \quad (4.13)$$

where σ_{za} is the stress in the z-direction on the free surface of the midplane of the neck. Substituting eq. (4.13) back into (4.12) and solving for σ_z , we have

$$\begin{aligned}\sigma_z &= 0.968 \sigma_x + \sqrt{\sigma_{za}^2 - 0.062 \sigma_x^2} \\ &\approx 0.968 \sigma_x \pm \sigma_{za}\end{aligned}\quad (4.14)$$

because $0.062 \sigma_x^2 \ll \sigma_{za}^2$ (as shown in eq. (4.16)). The negative sign in eq. (4.14) can be discarded because of the boundary condition at the neck that $\sigma_x = 0$ and $\sigma_z = \sigma_{za}$ when $x = a$.

Based on the force balance in the x-direction acting on an element at the midplane of the neck, Bridgman has derived a formula for a necking plate [183]

$$\left(\frac{x}{a}\right) \sigma_z = \left(\frac{x}{a}\right) \sigma_x - \left[R + \frac{a}{2} \left(1 - \frac{x^2}{a^2} \right) \right] \frac{\partial \sigma_x}{\partial x} \quad (4.15)$$

where x and a have been defined in Fig. 4.50. Introduction of eq. (4.14) into (4.15) results in a linear first order differential equation for σ_x , i.e.,

$$\frac{\partial \sigma_x}{\partial x} - \frac{0.032 x}{\left[a R + \frac{a^2}{2} \left(1 - \frac{x^2}{a^2} \right) \right]} \sigma_x = - \frac{x}{\left[a R + \frac{a^2}{2} \left(1 - \frac{x^2}{a^2} \right) \right]} \sigma_{za} \quad (4.16)$$

The solution for eq. (4.16) is

$$\sigma_x = \sigma_{za} \left[31.25 - 31.25 \frac{\left(\frac{R}{a}\right)^{0.032}}{\left(\frac{R}{a} + 0.5 - 0.5 \frac{x^2}{a^2}\right)^{0.032}} \right] \quad (4.17)$$

The above σ_{za} can be related to the average elastic strain, $\bar{\epsilon}_x$, which can be measured from the dimension of the neck using the relation of $\bar{\epsilon}_x = \ln(a/t)$ and related to the elastic strain in the x-direction at the position of x on the midplane of the neck, $\epsilon_x(\sigma_x, \sigma_y, \sigma_z)$, as follows

$$\bar{\varepsilon}_x = \frac{\int_0^a \varepsilon_x(\sigma_x, \sigma_y, \sigma_z) dx}{a} \quad (4.18)$$

where ε_x can be found from the plane strain condition using the equations of

$$\sigma_y = \mu (\sigma_x + \sigma_z) \quad (4.19)$$

and

$$\varepsilon_x = 1/E \{ \sigma_x - \mu (\sigma_y + \sigma_z) \} \quad (4.20)$$

where E is Young's modulus of Nb. Substituting eqns. (4.14), (4.17) and (4.19) into (4.20) yields

$$\varepsilon_x = \frac{\sigma_{za}}{E} \left\{ 9.55 - 10.1 \frac{\left(\frac{R}{a}\right)^{0.032}}{\left(\frac{R}{a} + 0.5 - 0.5 \frac{x^2}{a^2}\right)^{0.032}} \right\} \quad (4.21)$$

Substituting eq. (4.21) into (4.18) results in

$$\bar{\varepsilon}_x = \frac{\sigma_{za}}{a E} \left\{ 9.55 a - 10.1 \int_0^a \frac{\left(\frac{R}{a}\right)^{0.032}}{\left(\frac{R}{a} + 0.5 - 0.5 \frac{x^2}{a^2}\right)^{0.032}} dx \right\} \quad (4.22)$$

Thus, by numerical integration of eq. (4.22), σ_{za} can be found from $\bar{\varepsilon}_x$ for any specific R and a. With σ_{za} in hand, σ_z can be found from eqns. (4.14) and (4.17).

Stage of plastic deformation. The Von Mises yield criterion is used to monitor the initial yielding. Thus, when the effective stress reaches the yield strength of the Nb, plastic deformation begins. Now, Bridgman's formula for a necking plate on the condition of plane strain [183]

$$\sigma_z = \sigma_{za} \left\{ 1 + \ln [1 + 0.5 \frac{a}{R} (1 - \frac{x^2}{a^2})] \right\} \quad (4.23)$$

can be used directly to compute the nominal axial stress. By applying boundary

conditions at the neck, a relation between σ_{za} and the effective stress, $\bar{\sigma}$, can be found as follows. The plane strain condition at the stage of plastic deformation gives

$$\sigma_y = 0.5 (\sigma_x + \sigma_z) \quad (4.24)$$

Substituting eq. (4.24) into (4.11) yields

$$\bar{\sigma}^2 = 0.75 (\sigma_x - \sigma_z)^2 \quad (4.25)$$

Combining eq. (4.25) with the boundary condition that $\sigma_x = 0$ on the free surface of the midplane of the neck, we have

$$\sigma_{za} = 1.1547 \bar{\sigma} \quad (4.26)$$

where $\bar{\sigma}$ is determined by the effective strain $\bar{\varepsilon}$. The effective strain can be calculated from the plastic strain ε_{xp} in the x-direction using the plasticity equation which can be written as [184]

$$d\varepsilon_{xp} = \frac{d\bar{\varepsilon}}{\bar{\sigma}} [\sigma_x - 0.5 (\sigma_y + \sigma_z)] \quad (4.27)$$

Substituting eqns. (4.24) - (4.26) into (4.27) results in

$$d\varepsilon_{xp} = -0.866 d\bar{\varepsilon} \quad (4.28)$$

Integration of eqn. (4.28) yields

$$\bar{\varepsilon} = -1.1547 \varepsilon_{xp} \quad (4.29)$$

where ε_{xp} is constant over the plane of the neck because $\bar{\varepsilon}$ is constant over the whole plane of the neck [183]. In the computation, the effective strain at the initial yield is assigned as zero (i.e., ε_{xp} is equal to the total strain $\ln(a/t)$ deducted by the elastic strain at the yield), while the effective stress has a value of the yield strength of the unconstrained Nb. After the initial yield, the niobium is assumed to have perfect isotropy of strain hardening, and a power law, $\bar{\sigma} = C \bar{\varepsilon}^m$, is used to compute the effective stress. Thus, σ_z can be found by substituting the effective stress into eqns. (4.23) and (4.26).

Stage of localized plastic deformation. The localized plastic deformation is assumed to begin when the nominal axial stress is about to decrease. The length of

the region affected by necking, $2H$, shown in Fig. 4.50., is chosen as $2t$. After necking down to a point at the neck, the region with such dimension gives two triangles with the height equal to the base. The base is assumed to have no more deformation when the localized deformation begins. The assumptions give rise to a contour as shown in Fig. 4.50(c), and such contour is an approximation for the contour of Nb in the decohesion region, as shown in Fig. 4.48. The displacement in the stage of the localized deformation is assumed to come only from the deformation of the necking affected region and the computation of the nominal axial stress is carried out using eqs. (4.23) and (4.26).

In summary, with the above approximate model the effect of bonding conditions at the interface on the calculated $\sigma(u) \sim u$ curve is introduced by properly selecting the decohesion length at the interface, since the decohesion length is dependent on the interfacial conditions as revealed in the experiments (Sections 4.4.2 and 4.5.2). The effects of the intrinsic mechanical properties of ductile phase are addressed by utilizing the elastic modulus, yield strength and true stress-strain relation of the ductile phase throughout the computation of the $\sigma(u) \sim u$ curve. Finally, the size of the ductile phase comes into play through the selection of the decohesion length as well as the direct entry of the half thickness of the ductile phase in the model.

4.5.5 Comparison between the Model and Experiments

Effect of the decohesion length. Dependence of the stress-displacement curve on the decohesion length is shown in Fig. 4.53 which is generated using the true stress-strain data of 0.5 mm Nb. The results indicate that the maximum stress reached by the constrained Nb, σ_{\max} , increases with increasing constraints on the ductile reinforcement. However, increasing constraints decreases the work of rupture. Such results suggest that a relatively weak bond at the interface enhances the work of

rupture and therefore is conducive to toughening of the brittle matrix composites. Similar results are obtained by other investigators using different models [23,24,26].

The calculated parameters from the model based on the experimental data of 0.5 mm thick Nb lamina in Table 4.10 are presented in Table 4.12. Ratios of the calculated and measured normalized work of rupture, $E_t(\text{cal})/E_t(\text{exp})$, is also included in the table. A comparison between the calculated and measured data in Table 4.12 reveals that the calculated work of rupture deviates from the measured counterparts by about 20%. However, the general trend that work of rupture decreases with increasing interfacial fracture energy observed in the experiments has been maintained in the prediction of the model. The discrepancy in the values between the calculated and measured work of rupture lies in the assumptions involved in the model, especially the one relating to the contour of the Nb lamina in the decohesion region. Although the assumed contour of the neck makes the computation feasible, it does not exactly reflect the real contour of the Nb which actually displays a convex shape at the region away from the neck, as shown in Fig. 4.48. On the one hand, the assumed contour (a concave shape) leads to a larger strain to failure, when compared with the convex shape of the real contour; on the other hand, it also results in a larger radius of curvature at the neck than does the real contour. As such, a less severe state of triaxial stresses results and a lower stress in axial direction (Z-direction) is predicted by the model. All of these contribute to the discrepancy in the work of rupture. Nevertheless, the predicted values are reasonable approximations to the measured counterparts.

It is also noted from Table 4.12 that σ_{\max} predicted by the model is insensitive to the interfacial bonding conditions in the range of the measured decohesion lengths. The results suggest that the present coated and uncoated Nb/MoS₂ laminates are in the range of low constraints because in the high constraint range (i.e., short decohesion length), σ_{\max} is very sensitive to the decohesion length,

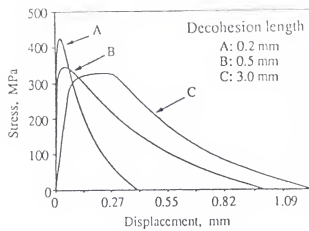


Fig. 4.53 Effect of decohesion length on the stress-displacement curve.

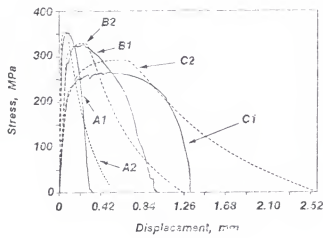


Fig. 4.54 Effect of reinforcement size on the stress-displacement curve. A1, B1 and C1 (solid lines) are experimental curves of the composites with 0.25, 0.5 and 1.0 mm thick Nb laminae, respectively; A2, B2 and C2 (dashed lines) are results from the model for composites with 0.25, 0.5 and 1.0 mm thick Nb laminae, respectively.

as shown in Fig. 4.53. An experimental evidence indicating that the present laminates are in the range of low constraints is that the maximum stress reached by the laminate composites with 1.0 mm Nb lamina are almost the same for different decohesion lengths ranging from ~ 5 to $\sim 15 \mu\text{m}$.

Effect of reinforcement size. A comparison of the size effect between the model and experiments for the uncoated Nb/MoS₂ laminates is shown in Fig. 4.54. The input data for the model are from eq. (4.8), Tables 4.8 and 4.10 with each size of Nb having its own measured parameters and properties. The input of Young's modulus is from the slope of the stress-strain curve of the unconstrained Nb in a simple tensile test. As shown in Fig. 4.54, the model fits the experimental data reasonably well except the stage of the localized plastic deformation. The deviation in this stage is believed to be due to the difference between the real and assumed contours of the neck, as discussed earlier. The parameters calculated from the model are summarized in Table 4.11. It is noted that the calculated maximum stress, the work of rupture and the normalized work of rupture are all close to the measured counterparts, clearly indicating that these can be estimated from the model.

The reinforcements used in composites for structural applications may be smaller in size than those tested in the present study. To predict the work of rupture for small size of reinforcements, it is necessary to know the decohesion length in advance for the use of the model. A plot of σ_{\max} vs. decohesion length computed from the model for the composites with 0.25 mm Nb lamina is shown in Fig. 4.55. It is noted that there exists a characteristic decohesion length, d_c , below which σ_{\max} becomes very sensitive to the decohesion length. Computation of the model shows that the characteristic decohesion length is equal to twice of the thickness of the niobium and the normalized work of rupture with the characteristic decohesion length, called as the characteristic normalized work of rupture, is constant regardless of size of the reinforcement.

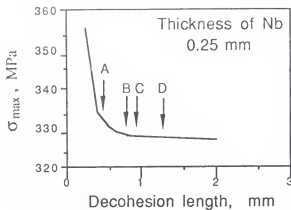


Fig. 4.55 A plot of σ_{\max} vs decohesion length. Arrow A shows characteristic decohesion length, and arrows B, C and D show the measured decohesion lengths of the composites containing uncoated, Al_2O_3 coated and ZrO_2 coated Nb laminae, respectively.

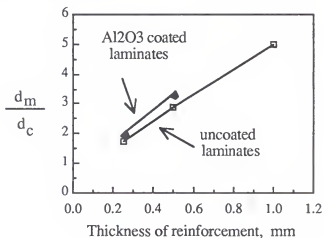


Fig. 4.56 A plot of ratio of the measured to characteristic decohesion lengths as a function of reinforcement size.

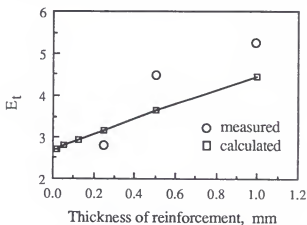


Fig. 4.57 Normalized work of rupture as a function of reinforcement size.

The measured decohesion lengths, d_m , in the present study are all larger than d_c . However, the ratio of d_m to d_c is found to be a linear function of size of the reinforcement, as shown in Fig. 4.56. The relations found are

$$\begin{aligned} d_m/d_c &= 0.66 + 10.72 t && (\text{for Al}_2\text{O}_3 \text{ coated laminates}) \\ d_m/d_c &= 0.66 + 8.70 t && (\text{for uncoated laminates}) \end{aligned} \quad (4.30)$$

It is noted that d_m becomes closer to d_c as size of the reinforcement decreases, suggesting that the normalized work of rupture becomes smaller and closer to the characteristic normalized work of rupture. The oxide coating changes the slope of the line, indicating that the coating enhances decohesion and such effect becomes larger as the reinforcement size increases. With the aid of eq. (4.30), the decohesion length of small size of the reinforcement can be predicted and the work of rupture be calculated from the model. A plot generated in this way is shown in Fig. 4.57 which shows that E_t decreases with decreasing the reinforcement size, as found in the experiments. Thus, the model can be used to estimate the contribution of ductile reinforcements to the toughness of a brittle matrix composite.

Effect of yield strength and work hardening. Effects of yield strength and work hardening on the work of rupture are evaluated by substituting the properties of several different materials into the model. The properties are obtained from Reference [185] and the true stress-strain curves for some materials are shown in Fig. 4.58. It is noted that both 4340 steel and 70/30 brass have a higher work hardening rate than the Nb used in the present study. The computed stress-displacement curves are shown in Fig. 4.59, and the input and output data are summarized in Table 4.13. It is clear that work of rupture increases with increasing work hardening rate. Although 70/30 brass has the lowest yield strength, its high work hardening rate enables it to have a much higher work of rupture than both 4340 steel and Nb both of which have higher yield strengths than the brass. The reason for such phenomenon is that a high work hardening rate reinforcement has a higher increase rate in the load-carrying ability,

Table 4.13 The input and output data for computing the stress-displacement curves shown in Fig. 4.59 (the thickness of all materials is assumed as 0.5 mm)

Material	Input Data			Output Data			
	$\sigma_t = K\epsilon_t^n$ (MPa)	σ_0 (MPa)	E (GPa)	μ	σ_{max} (MPa)	ξ^2 (m^2)	E_t
Nb	$363\epsilon_t^{0.085}$	210	105	0.39	329	196,000	3.7
SAE4340 steel	$642\epsilon_t^{0.15}$	230	193	0.29	496	351,000	6.1
0.6% C steel	$1573\epsilon_t^{0.10}$	500	199	0.29	1337	801,000	6.4
70/30 brass	$897\epsilon_t^{0.49}$	80	111	0.30	483	662,000	33.1

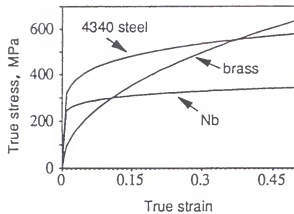


Fig. 4.58 The true stress-strain curves of the some materials used for evaluating effects of yield strength and work hardening.

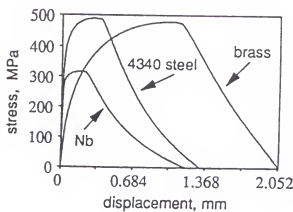


Fig. 4.59 Computed stress-displacement curves using the data in Fig. 4.58 and Table 4.13.

and instability (i.e., the localized plastic deformation within the necking region), comes relatively later than a low work hardening rate reinforcement. Thus, high work hardening rate reinforcements have a relatively longer stage of plastic deformation in the whole decohesion region, leading to more energy dissipation and higher work of rupture. It is noteworthy that the brass has a very high normalized work of rupture, which suggests that the normalized work of rupture could probably be used as an indicator of the efficiency with which the work hardening contributes to enhancing the work of rupture.

When yield strength is very high, such as 0.6 % C steel in Table 4.13, the work of rupture would be also very high. As shown in Table 4.13, 0.6% C steel has a much higher work of rupture than 70/30 brass although it has a lower work hardening rate than the brass. Contribution of yield strength to work of rupture is mainly to increase the maximum stress reached by the constrained reinforcement. From the above discussion, it is concluded that high work hardening rate and high yield strength are both beneficial to the work of rupture. Work hardening, however, is more effective in enhancing the work of rupture than yield strength because the former delays the instability of deformation for constrained ductile reinforcements, therefore more material of the reinforcements participates in plastic deformation and more energy has to be consumed.

In summary, based on the small-scale bridging concept, the experiments and the model indicate that work of rupture is enhanced by a relatively weak bond at the matrix/reinforcement interface, by large size of reinforcement, and by high yield strength and high work hardening rate. High work hardening rate is more effective in enhancing work of rupture than high yield strength.

4.6 Effects of Interface, Size and Orientation of Ductile Phases on Toughness

In this section the effects of interface, size and orientation of ductile phases on the toughness of composites will be discussed. For the procedures of measuring the toughness of the composites, please refer to Section 3.6.

4.6.1 Dual-Effect of the Matrix/Reinforcement Interface on the Toughness of the Composites

Typical load-displacement curves of bending tests on chevron notched composite laminates hot pressed at 1400°C are shown in Fig. 4.60. There are two prominent features in the figure: (1) uncoated Nb reinforced composites exhibit the highest peak load, (2) mechanical behavior of ZrO₂ and Al₂O₃ coated systems are similar, both of them showing an increase in the carried load in the last part of the displacement curves. The latter observation is caused by the extensive delamination at the interface, and correspondingly more niobium participates in deformation and deforms under much less constrained condition. Because of this feature, the total energy consumed to break a specimen (area under the curve) for the coated composites is larger than the uncoated ones. The work of fracture, defined as the total energy normalized with respect to the generated crack area [186], for the various composites are presented in Table 4.14. As seen in the table, the coated composites show the higher work of fracture, indicating that the low interfacial fracture energy, and thus long decohesion length, is beneficial to improving the toughness of the composite. This result is consistent with predictions based on other numerical and analytical studies [23,24,26].

However, the damage tolerance determined from the peak load of the chevron notched specimens shows an opposite trend. The damage tolerance determined in this way is also included in Table 4.14. The data show that uncoated Nb reinforced composites exhibit the highest damage tolerance, followed by Al₂O₃ coated and then

Table 4.14 Measured damage tolerance, steady-state toughness and other relevant parameters from the tensile tests and bend tests.

Material	Monolithic MoSi ₂	Uncoated Nb reinforced	Al ₂ O ₃ coated Nb reinforced	ZrO ₂ coated Nb reinforced	ZrO ₂ coated Nb reinforced
Hot pressing temperature	1700°C	1700°C and 1400°C	1400°C	1400°C	1700°C
Damage tolerance ^a (MPa.m ^{1/2})	3.3 ± 0.3	15.2 ± 1.3	14.0 ± 1.5	12.8 ± 1.5	8.6 ± 1.3
Work of fracture ^a (J/m ²)	690 ± 30	21,600 ± 3,000	28,700 ± 1,900	28,700 ± 4,600	2,800 ± 300
Interfacial fracture energy ^b	-	high	medium	low	low
Ductility of the reinforcement ^b	-	high	high	high	low
Decohesion	-	0.86 ± 0.09	0.94 ± 0.23	1.31 ± 0.61	-
Length (mm) ^c	-	350 ± 15	340 ± 29	330 ± 17	-
Peak Stress ^c (MPa)	-	85,400 ± 7,800	92,400 ± 9,500	103,200 ± 7,300	-
Work of Rupture ^c (J/m ²)	-				
Steady-State Toughness ^c (MPa.m ^{1/2})	-	88	92	97	

a. From bend tests on chevron notched composite laminates reinforced with 20 vol.% of Nb laminae (0.25 mm thick).

b. For details, see Tables 4.5 and 4.7.

c. From tensile tests on a single constrained Nb (0.25 mm thick).

#. Four specimens for each condition have been tested except Al₂O₃ coated Nb system for which eight specimens have been tested.

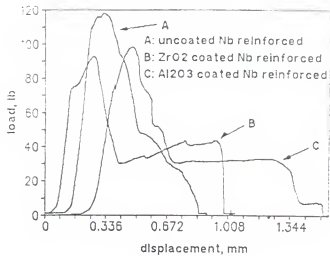


Fig. 4.60 Typical load-displacement curves of chevron notched specimens for laminated composites containing 20 vol% of Nb laminae with different interfacial conditions, hot pressed at 1400°C for 1 hour. The origin for each curve has been shifted for the convenience of observation.

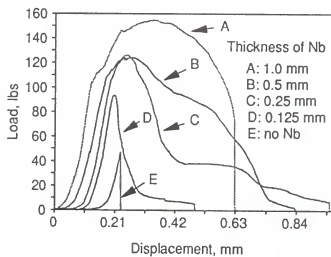


Fig. 4.61 Typical load-displacement curves of chevron notched specimens for monolithic MoSi₂ and laminated composites containing different thicknesses of uncoated Nb laminae, hot pressed at 1400°C for 1 hour. The origin for each curve has been shifted for the convenience of observation.

ZrO₂ coated composites. This sequence is parallel to the increase in the interfacial fracture energy of the composites, that is, the higher the interfacial fracture energy, the higher the damage tolerance of the composites.

The data in Table 4.14 also indicate that loss of ductility of the ZrO₂ coated Nb foils hot pressed at 1700°C results in a large drop in the toughness of the laminated composites. Therefore, the damage tolerance data suggest that a high degree of constraint is conducive to toughness as long as the ductile reinforcement has a high slip capability. When the reinforcement loses its slip capability, as in the case of ZrO₂ coated composites processed at 1700°C, decreasing the constraint, i.e., increasing the gauge length by decreasing the interfacial bonding, is more beneficial to improving the toughness.

In summary, the results from the bend test of chevron notched specimens indicate that the role of the interface for ductile reinforcement and debonding in the toughness depends on the criterion used to describe the toughness of the composites. If the peak load of the chevron notched specimen is used as an indicator of the toughness, a strong bonding, and therefore a high degree of constraints, would be desirable. On the other hand, if the total energy consumed to break a specimen is used as indicative of its toughness, then a relatively weak bonding is required.

The aforementioned dual-effects of the interfacial properties on the toughness of the composites can also be related to the data obtained from the simple tensile tests on a single constrained Nb foil which has been discussed in Section 4.5. For convenience, the properties measured from the tensile tests on 0.25 mm Nb reinforced composites have also been included in Table 4.14. The steady-state toughness of the composites in the table is calculated from eq. (2.6) and is proportional to the work of rupture of the constrained ductile phase. It can be seen from Table 4.14 that increasing decohesion length is conducive to improving steady-state toughness of the composites, a trend also shown by the work of fracture measured from chevron-notched specimens. Table 4.14,

at the same time, also reveals that the peak stress reached by the constrained Nb decreases with increasing decohesion length, a trend similar to that exhibited by the damage tolerance measured from the chevron notched specimens. This apparently dual role of the interface can be explained by relating the maximum stress reached by the constrained ductile phases to the crack propagation resistance in the case of large-scale bridging (i.e., crack length is at the same order of magnitude as the bridging length) as observed in the present composites. In Section 4.7, the large-scale bridging will be treated, and the results indicate that the maximum crack propagation resistance of the composites increases with increasing decohesion length. However, the maximum crack propagation resistance is achieved only after the crack has propagated extensively. When crack size is small, the composites with less decohesion show a higher crack propagation resistance than the counterparts with more decohesion. Therefore, it seems that the choice of weak or strong interface in describing the fracture behavior of ductile-phase-toughened composites depends on the criterion used to describe the toughness of the composites.

4.6.2 Effects of Niobium Size on the Toughness

Representative load-displacement curves of chevron notched specimens for monolithic MoSi₂ and laminated composites containing different thicknesses of Nb laminae are shown in Fig. 4.61. The origin for each curve in this figure has been shifted for the convenience of observation. It is noted that the catastrophic failure of MoSi₂ has changed to graceful failure, and the area under the load-displacement curve as well as the peak load have increased by the incorporation of ductile Nb laminae into the matrix. A comparison between laminated composites reveals that the area under the load-displacement curve increases with increasing thickness of Nb laminae. The peak load reached by the composites also exhibits a similar trend, i.e., as thickness of Nb

laminae increases, the peak load increases, with an exception of 0.5 mm Nb laminae which shows a similar peak load as 0.25 mm Nb laminae.

The measured work of fracture and damage tolerance are summarized in Table 4.15. It is clear from the table that the work of fracture of the composites increases with increasing thickness of Nb laminae. Similar size effects have also been observed in Al₂O₃/Ni [130], WC-Co/Mo [131] and NiAl/Nb [132] composite systems. The damage tolerance, however, does not exhibit a monotonic variation with lamina thickness. It is believed that this is due to the combined effects of size as well as intrinsic properties of Nb laminae. As mentioned in Section 4.4, the peak load of the bend test is mainly carried by Nb laminae. The damage tolerance, therefore, is actually an indicator of the bridging capability of the ductile phase and should be related to size, intrinsic properties and fracture behaviors of Nb laminae.

Overall views of representative fracture surfaces for composites containing different size Nb laminae are provided in Fig. 4.62. Higher-magnification views of the fracture surfaces of different thicknesses of Nb laminae are presented in Fig. 4.63. The crack propagation is from the top to bottom in Fig. 4.63. The positions from where the fractographs of Fig. 4.63 are taken are indicated in Fig. 4.62 with the a, b, c and d in Fig. 4.62 corresponding to the figure designation (a), (b), (c) and (d) in Fig. 4.63. It is noted that the fracture mode of Nb laminae changes from elongated dimples (Fig. 4.63(a)) to quasi-cleavage (Fig. 4.63(c) and (d)) as the thickness of Nb laminae decreases. The change in the fracture mode with the thickness of the niobium laminae can be related to the change of Nb ductility. The microhardness and yield strength of hot pressed Nb laminae have been included in Table 4.15. As shown in Table 4.15, the microhardness and yield strength of the Nb laminae increases with decreasing thickness. Thus, the thinner the Nb lamina, the less ductile it is.

Based on the above observations, it is clear that the damage tolerance of the composites in the present study is a reflection of the combined effects of the thickness

Table 4.15. Mechanical properties measured from MoSi₂/Nb composite laminates showing the effects of size and orientation of the ductile phase (niobium)

Thickness of Nb lamina (mm)	0.125	0.125	0.25	0.5	1.0
Orientation	T	N	N	N	N
Damage Tolerance (MPa.m ^{1/2})	14.9 ± 1.4	12.2 ± 0.5	15.2 ± 1.1	15.4 ± 0.6	17.6 ± 0.1
Work of Fracture* (J/m ²)	6,960 ± 350	5,490 ± 200	21,600 ± 3,000	30,900 ± 1,700	35,900 ± 3,500
HV (kg/mm ²)	155	155	130	114	104
σ_0 (MPa) [#]	279@	279@	236 ± 5	210 ± 11	180 ± 9
σ_0/HV	1.80@	1.80@	1.80	1.85	1.73

* 3, 3, 9, 5 and 3 specimens have been tested for laminates containing 0.125 (T-orientation), 0.125 (N-orientation), 0.25, 0.5 and 1.0 mm Nb laminae, respectively.

Three specimens for each size of Nb lamina have been tested.

@ σ_0 is not measured directly, but obtained by assuming $\sigma_0/HV = 1.80$.

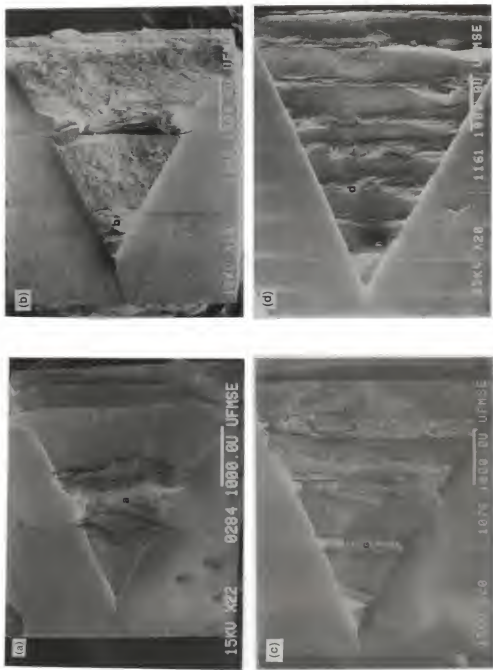


Fig. 4.62 Overall views of typical fracture surfaces of the laminated composites; (a) reinforced with 1.0 mm thick Nb laminae; (b) reinforced with 0.5 mm thick Nb laminae; (c) reinforced with 0.25 mm thick Nb laminae; (d) reinforced with 0.127 mm thick Nb laminae. The a, b, c and d in the figures indicate the positions where Fig. 4.63 has been taken.

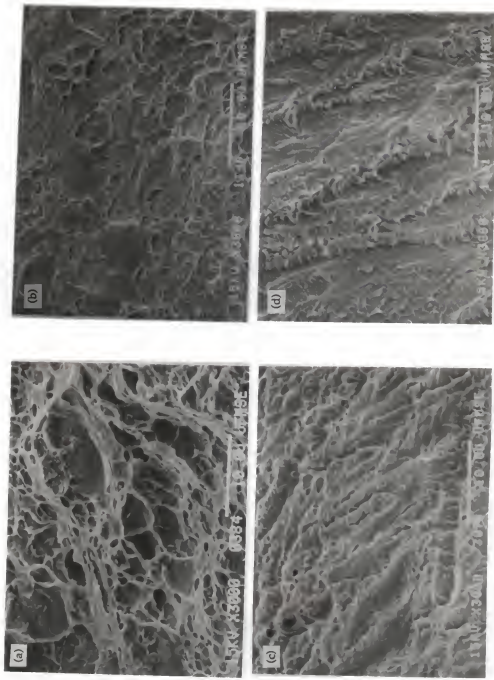


Fig. 4.63 Fracture surfaces of Nb laminate in the laminated composites. Nb laminate in (a) is 1.0 mm, (b) 0.5 mm, (c) 0.25 mm, and (d) 0.127 mm thick. The positions where the figures (a), (b), (c) and (d) are taken are shown in Fig. 4.62.

and the intrinsic properties of Nb laminae. An attempt has been made to separate these two combined effects, and the results will be discussed in Section 4.6.5.

4.6.3 Effects of Orientation of Niobium Lamina on the Toughness

The two different orientations of chevron notches are presented schematically in Fig. 4.64. For the sample shown in Fig. 4.64(a), crack propagation in the matrix is normal to the niobium laminae. Therefore, this orientation is called N-orientation. For the sample shown in Fig. 4.64 (b), the crack propagation is transverse to the niobium laminae. Thus, it is called T-orientation. Typical load-displacement curves of chevron-notched specimens for two different orientations of the composites containing 0.127 mm thick Nb laminae are shown in Fig. 4.65. Again, the origins of the curves in the figure has been shifted to facilitate the comparison. The corresponding damage tolerance and work of rupture for the two orientations have been summarized in Table 4.15. It is clear form the table that T-orientation not only has a larger work of fracture but also has a larger damage tolerance than N-orientation.

A general view of the fracture surfaces of chevron notched specimens for the two orientations is presented in Fig. 4.66. A relatively higher magnification of the fracture surface is shown in Fig. 4.67 to reveal the general characteristics of crack propagation for both orientations. The crack propagation in Fig. 4.67 is from the top to bottom. For the N-orientation, the crack propagation in the matrix is discontinuous in nature, as mentioned before. In contrast, for the T-orientation the crack propagates continuously once initiated, making less matrix fracture and less tortuosity on the fracture surface of the matrix (Fig. 4.67). It is expected that the discontinuous crack propagation is more energy consuming process than the continuous crack propagation. However, T-orientation (continuous crack propagation) actually exhibits a higher damage tolerance and work of fracture than N-orientation, as shown in Table 4.15. The apparent contradiction could be explained in terms of the observation that for the

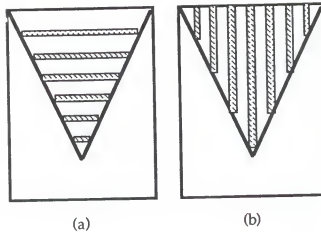


Fig. 4.64 (a) The notched plane of N-orientation where crack propagates normal to the lamina plane; (b) The notched plane of T-orientation where crack propagates transverse to the lamina plane. Crack propagates from the bottom to top in the figures.

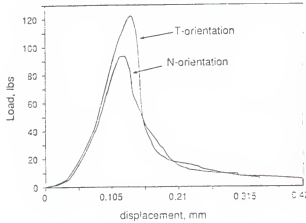


Fig. 4.65 Representative load-displacement curves of chevron notched specimens for two different orientations of the composites containing 0.127 mm thick Nb laminae. The origins of the curves have been shifted for the convenience of comparison.

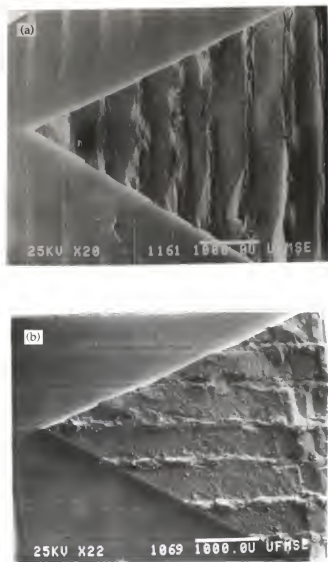


Fig. 4.66 Fracture surfaces of the laminated composites. (a) Crack propagates normal to the lamina plane (N-orientation); (b) Crack propagates transverse to the lamina plane (T-orientation).

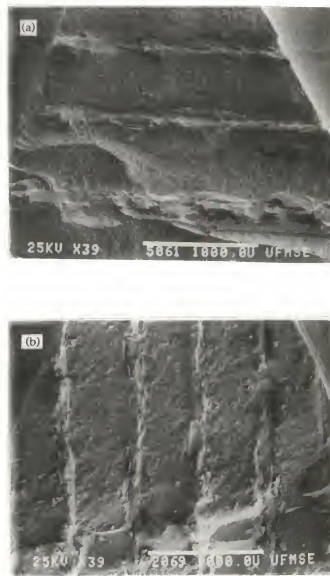


Fig. 4.67 A relatively higher magnification view of the fracture surfaces of the laminated composites, crack propagating from the top to bottom. (a) N-orientation; (b) T-orientation.

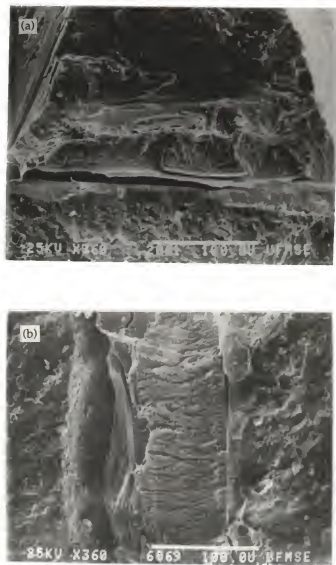


Fig. 4.68 Fracture surfaces of the Nb laminae in laminated composites. The direction of the overall crack propagation is from the top to bottom. (a) N-orientation; (b) T-orientation.

present specimens the crack propagation in the matrix actually occurs at the low level of load, and the peak load and the area after the peak load is controlled by the deformation and fracture of Nb reinforcements. Thus, the crack propagation characteristics of the matrix is not a dominant factor in determining the toughness of the present composites.

Fracture surfaces of Nb laminae for the N- and T-orientations are shown in Fig. 4.68. The fracture surfaces of Nb laminae reveals that fracture modes for the two orientations are very similar, both exhibiting quasi-cleavage fracture. The dependence of the measured toughness on the lamina orientation, therefore, might lie on the differences in the bending contributions of Nb laminae in the different orientations, which will be further discussed in the following sections.

4.6.4 Stress Analysis of the Chevron Notched Specimens of the MoSi₂/Nb Laminated Composites

The discussion in Section 4.4 has clearly shown that the extensive crack propagation in the matrix has occurred at the low level of load and the peak load is mainly carried by Nb laminae in the bend test. Based on such observation, a simple and approximate model has been proposed to analyze the present specimens. The basic purpose of the model is to relate the bridging capability of the Nb laminae to the peak load of the bend test. Assumptions involved in the present mechanics-of-material approach are (1) one-dimensional stress is assumed for chevron notched bend bar; (2) all sections that are far from the notch plane and are initially plane and perpendicular to the axis of the beam remain plane and perpendicular to it after bending; (3) all longitudinal elements bend into concentric circular arcs; (4) near the peak load the matrix in the tensile portion has already failed and the load is carried only by the bridging ductile phases; (5) the deformation in the tensile portion only comes from the

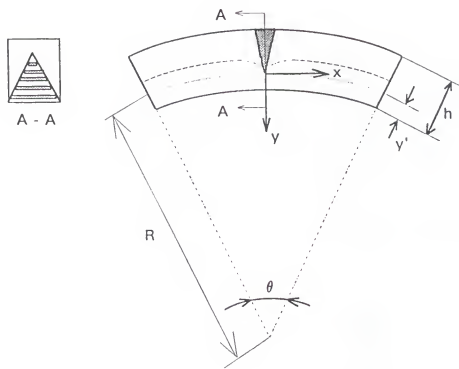


Fig. 4.69 Schematic of deformed bend bar, showing the relevant parameters used in the analysis.

ductile phases which are inside the "decohesion region" because other ductile phases are bonded to the matrix and only undergo elastic deformation.

Figure 4.69 shows the relevant parameters used in the model. The hatched area in the tensile portion of the beam denotes the bridging region. The dashed line indicates the real neutral axis which changes gradually near the notch plane from the midplane of the beam to the position close to the bottom of the notch. The position of the neutral axis right at the notch plane varies during the bending, because in the tensile portion of the notch plane load is carried only by Nb ligaments, and the ligaments enter the stage of plastic deformation, while the compression portion (containing MoSi₂ matrix and Nb laminae) still undergoes elastic deformation. To simplify the calculation, the neutral axis right at the notch plane has been chosen as the neutral axis for the beam and is indicated as the dotted line in Fig. 4.69. This is a reasonable approximation since the moment and force balance are calculated right at the notch plane. Thus, the position of the neutral axis (N.A.) is determined from force balance at the x-axis right at the notch plane, i.e.,

$$\int \int_0^{y'} \sigma_{x(\text{com})} dy dz + \int \int_{(h-y')}^0 \sigma_{x(\text{ten})} dy dz = 0 \quad (4.31)$$

where $\sigma_{x(\text{com})}$ is the stress component at x-direction in the compressive portion, $\sigma_{x(\text{ten})}$ is the nominal stress on the bridging ductile phases at x-direction in the tensile portion, h and y' are defined in Fig. 4.69, and z direction is perpendicular to the x-y plane.

Based on the geometry and the assumptions mentioned above, it can be shown that the engineering strain in the compressive portion, ϵ_c , is

$$\epsilon_c = - \frac{Y}{R} \quad (4.32)$$

and the nominal strain inside the decohesion region in the tensile portion, ϵ_t , is

$$\epsilon_t = - \frac{Y L}{R d_0} \quad (4.33)$$

where R is the radius of curvature of the neutral axis, L the outer span of the bend test setup, and d_0 the decohesion length at the matrix/reinforcement interface. $\sigma_x(\text{com})$ in eq. (4.31) is determined from the corresponding compressive strain in eq. (4.32) according to the elastic stress-strain relations for MoSi₂ and Nb. $\sigma_x(\text{ten})$ is calculated from the corresponding strain in eq. (4.33). The relation between $\sigma_x(\text{ten})$ and ε_t is calculated based on the equations derived in Section 4.5. Since at the beginning of the calculation the position of the neutral axis is not known for a specific value of R, the values of Y in eqns. (4.32) and (4.33) are unknown. An iteration approach has been used to calculate the position of the neutral axis by first assuming the midplane of the beam as the neutral axis, then calculating the corresponding ε_c and ε_t , and substituting them into eq. (4.31) to check whether or not eq. (4.31) is satisfied. If eq. (4.31) is not satisfied, a new neutral axis closer to the bottom of the notch than the former neutral axis is assumed, and the new ε_c and ε_t are calculated, and eq. (4.31) checked again. The procedure is repeated until the absolute values of the two terms on the left hand side of eq. (4.31) are within $\pm 5\%$ of each other.

Once the neutral axis for one specific value of R has been found, then it is straightforward to find the bending force, P, using the following equation

$$\frac{LP}{8} = - \int_0^y y \sigma_{x(\text{com})} dy dz + \int_{-(h-y)}^0 y \sigma_{x(\text{ten})} dy dz \quad (4.34)$$

Note that for each R value, there is only one corresponding bending force. By decreasing R gradually, therefore, a maximum bending force can be found which is regarded to be equivalent to the peak load of the load-displacement curve of chevron notched specimens. Comparison between this simple and approximate model and experiments is made in the following section.

Table 4.16 Comparison between the measured and calculated damage tolerances for laminated composites with N-orientation.

Thickness of Nb laminae (mm)	Designation of Specimens	K _{max(meas)} (MPa.m ^{1/2})	K _{max(cal)} (MPa.m ^{1/2})	$\frac{K_{\max(\text{meas})} - K_{\max(\text{cal})}}{K_{\max(\text{meas})}}$
0.5	HP051	15.7	12.5	-20.4 %
0.5	HP052	14.8	13.1	-11.5 %
0.5	HP053	16.1	12.8	-20.5 %
0.5	HP054	15.6	12.7	-18.6 %
0.5	HP055	14.7	12.5	-15.0 %
0.25	HP0251	15.0	11.9	-20.7 %
0.25	HP0252	15.2	12.4	-18.4 %
0.25	HP0253	14.9	12.6	-15.4 %
0.25	HP0254	14.9	12.0	-19.5 %
0.25	HP0255	16.4	12.5	-23.8 %
0.25	HP0256	14.8	12.2	-17.6 %
0.25	HP0257	16.9	12.6	-25.4 %
0.25	HP0258	15.7	12.1	-22.9 %
0.25	HP0259	13.2	11.9	-9.8 %

4.6.5 Comparison between the Experiments and Analytical Results

Table 4.16 compares the measured and calculated damage tolerances, designated as K_{max} in the table, for N-orientation laminated composites reinforced with 0.5 mm or 0.25 mm thick Nb laminae. Since the samples tested are not exactly the same in dimension, the calculation is carried out on the basis of the dimensions of each specimen. As mentioned before, different thicknesses of Nb laminae have different intrinsic mechanical properties (eq. (4.8)). Thus, the relations between $\sigma_x(\text{ten})$ and ϵ_t are different for 0.5 and 0.25 mm Nb laminae. As can be seen from the table, the calculated damage tolerances are about 15% lower than the measured data. The discrepancy probably comes from the assumption (1) in Section 4.6.4 because the state of stress near the notch plane is 3-dimensional. The position dependence of decohesion length at the interface may also contribute to the deviation of the calculated damage tolerance from the measured data. Nevertheless, the simple model reflects the main feature of the ductile-phase-reinforced composites, that is, the peak load of the composites is related to the bridging capability and the size of the ductile ligaments.

By assuming that different sizes of Nb laminae have the same intrinsic mechanical properties, the model can be used to predict the effect of size of Nb laminae on the toughness of the composites. One of the results calculated in this way has been presented in Fig. 4.70 in which it is assumed that all different sizes of Nb laminae have the same properties as that measured from 0.25 mm Nb laminae. It is clear from Fig. 4.70 that the damage tolerance of the composites increases with increasing size of Nb laminae. Thus, It can be concluded that in the thickness range studied (from 0.1 to 1.0 mm), as Nb lamina thickness increases, both the damage tolerance and the work of fracture of the composites increase.

Since the nominal stress on the bridging Nb as a function of the crack opening in the T-orientation is not known, the present model cannot be used directly to compare with the experiments at the T-orientation. However, as discussed above, the damage

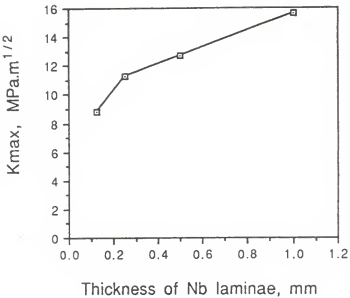


Fig. 4.70 Effect of Nb lamina thickness on toughness of the composites, calculated from the proposed model assuming that different thicknesses Nb laminae have the same intrinsic properties.

Table 4.17 Measured toughness of the composites containing Nb laminae with a thickness of 0.127 mm and moment of inertia of Nb cross section about the neutral axis at the notch plane.

	Damage Tolerance* K_{max} (MPa.m $^{1/2}$)	Work of Fracture (J/m 2)	Moment of Inertia of Nb Cross Section I_{Nb} (mm 4)	$\frac{K_{max}(N)}{K_{max}(T)}$	$\frac{\text{Work of}}{\text{Work of}}\frac{\text{Fracture}(N)}{\text{Fracture}(T)}$	$\frac{I_{Nb}(N)}{I_{Nb}(T)}$
Laminates with N-orientation	12.2 ± 0.5	5,490 ± 200	1.261	0.80	0.79	0.84
Laminates with T-orientation	14.9 ± 1.4	6,960 ± 350	1.507			

* Calculated from the peak load of the bending test.

tolerance of the composites is related to bridging capability of the ductile laminae. Therefore, it is believed that the observed orientation dependency of the damage tolerance is due to the different bending contributions of Nb laminae in the different orientations. Since the moment of inertia of Nb cross section about the neutral axis at the notch plane reflects the contribution of Nb laminae to resisting the external bending moment at the stage of elastic deformation, the moment of inertia of Nb cross section is calculated and listed in Table 4.17. Note that both the ratio of the damage tolerances in the N-orientation to the T-orientation and the ratio of the work of fracture in the N-orientation to the T-orientation are very close to the ratio of the moment of inertia of Nb cross section at the N-orientation to the T-orientation, indicating that the orientation dependence of damage tolerance is indeed due to the different bending contributions of Nb laminae in the different orientations.

4.7 Modeling of Ductile Phase Toughening --- Large Scale Bridging

As discussed in Section 2.3, ductile phase bridging has been analyzed theoretically by many investigators. The primary mechanism responsible for the toughening has been ascribed to the bridging of ductile ligaments behind the advancing crack tip [20,21,23-26]. In these studies, the toughening effect has been evaluated on the basis of the assumption of the small-scale bridging (SSB) for which the bridge-length is small relative to the crack length and the specimen size. However, in most of the ductile-phase-toughened composites, the bridging length is often at the same scale as the crack length and specimen size [116,133]. Our present research results also demonstrated that MoSi₂/Nb composites is large-scale bridging (LSB).

Ravichandran [134,135] and Cox [136,137] have recently proposed models for describing large scale bridging to account for the effects of the specimen geometry and crack length. Their approaches were intended to give a better estimation of the ductile phase toughening. However, the effect of size of ductile phases has not been addressed

in their studies and the ductile phase constitutive relations are assumed artificially [134-137]. In this section, therefore, not only the size effect will be addressed but also the constitutive relation of the ductile reinforcement based on the measurement from MoSi_2/Nb composites will be included to give insight into the direct relation between the constituents' properties (fracture energy of the matrix/reinforcement interface, decohesion at the interface, size of the ductile phase, etc.) and the overall performance of the composites.

4.7.1 Basic Model

The problem is defined in Fig. 4.71 which shows a crack of length $2a$ with ductile phase bridging in an infinite body. The hatched areas represent the bridging ligaments and the crack is assumed to grow symmetrically along the x -axis at the both positive and negative directions. σ_* and σ_i designate the externally applied stress and bridging stressess, respectively. For the present study, the effective stress intensity acting at the crack tip is treated as a superimposition of an opening stress intensity caused by the externally applied stress and a stress intensity of opposite sign caused by the clamping forces of the bridging ligaments. Due to the nature of the bridging analysis and for the sake of simplicity, it is assumed that during the propagation, the crack tip does not stop inside the ductile ligaments nor at the interface, but in the matrix. Thus, the effective stress intensity acting at the crack tip, K_{tip} , can be written as

$$K_{\text{tip}} = K_{\text{ext}} - K_{\text{bridge}} \quad (4.35)$$

where K_{ext} and K_{bridge} are the stress intensity factors induced by the external stress and bridging tractions, respectively. Rearranging eqn. (4.35), we have

$$K_{\text{ext}} = K_{\text{tip}} + K_{\text{bridge}} \quad (4.36)$$

The crack propagates when $K_{\text{tip}} = K_m$ or $K_{\text{ext}} = K_c$ where K_m and K_c are the fracture toughness of the matrix and composite, respectively. For a given matrix, K_m

is a constant. Thus the crack-growth resistance of the composite varies with K_{bridge} (eqn. 4.36). To obtain the effective stress intensity factor, a stress function proposed by Sedov [187] satisfying the present boundary conditions is utilized. The function has been given as:

$$\phi' = \frac{1}{\pi \sqrt{z^2 - a^2}} \int_a^z \frac{g(\xi) \sqrt{a^2 - \xi^2}}{z - \xi} d\xi \quad (4.37)$$

where a is defined in Fig. 4.71, $g(\xi) = \sigma_* - (\sigma_1 + \sigma_2 + \dots + \sigma_n)$ and $z = x + iy$. Following Westergaard [188], the Sedov's stress function can be related to the effective stress intensity factor (mode I) and the equilibrium crack opening field along the y -axis, $v(x, y)$, by the following equations

$$\sigma_y(x, y) = \operatorname{Re} \phi' + y \operatorname{Im} \phi'' \quad (4.38)$$

$$K_{\text{tip}} = \lim_{r \rightarrow 0} \sigma_y(r, \theta) \sqrt{2\pi r}, \quad \text{when } \theta = 0 \quad (4.39)$$

$$\text{and} \quad 2Gv(x, y) = \frac{\kappa + 1}{2} \operatorname{Im} \phi - y \operatorname{Re} \phi' \quad (4.40)$$

where r and θ are the polar coordinate with the origin at the crack tip, $\kappa = 3 - 4\nu$, ν

the Poisson's ratio, G the shear modulus, $\phi = \int_a^z \phi' dz$ and $\phi'' = \frac{d\phi'}{dz}$.

Substituting eqns. (4.37) and (4.38) into (4.39) and (4.37) into (4.40), we have

$$K_{\text{tip}} = K_{\text{ext}} - \frac{1}{\sqrt{\pi} a} \int_a^z (\sigma_1 + \sigma_2 + \dots + \sigma_n) \sqrt{\frac{a + \xi}{a - \xi}} d\xi \quad (4.41)$$

and

$$v(x) = v_{\text{ext}}(x) - \frac{\kappa + 1}{4G\pi} \operatorname{Im} \left\{ \int_a^x \int_a^z (\sigma_1 + \sigma_2 + \dots + \sigma_n) \frac{\sqrt{a^2 - \xi^2}}{\sqrt{x^2 - a^2} (x - \xi)} d\xi dx \right\} \quad (4.42)$$

where K_{ext} and $v_{\text{ext}}(x)$ are the contributions of the external stress to the effective stress intensity factor and the equilibrium crack face displacement, respectively, and

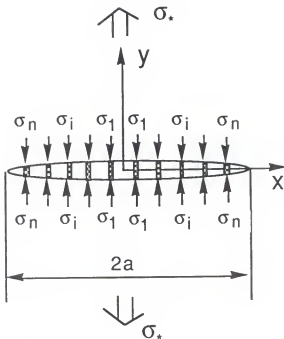


Fig. 4.71 A schematic of an internal bridged crack.

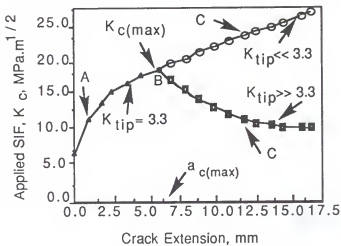


Fig. 4.72 Typical R-curve behavior of ductile-phase-toughened composites. Calculation parameters: The fracture toughness of the matrix is $3.3 \text{ MPa.m}^{1/2}$; Thickness of the Nb lamina $20 \mu \text{m}$; Decohesion length at the interface $5 \mu \text{m}$; Volume fraction of Nb 20 vol.%. The unit of the K_{tip} is $\text{MPa.m}^{1/2}$. The detailed crack opening profile and bridging tractions at points A, B and C in the figure are presented in Fig. 4.73.

$$K_{ext} = \sigma_* \sqrt{\pi a} \quad (4.43)$$

$$v_{ext}(x) = \frac{\kappa + 1}{4G} \frac{\sqrt{a^2 - x^2}}{\sqrt{\pi a}} K_{ext} \quad (4.44)$$

The second terms in the right hand side of eqns. (4.41) and (4.42) are the contributions of the bridging ligaments to the effective stress intensity factor (designated as K_{bridge}) and to the equilibrium crack face displacement (designated as $v_{bridge}(x)$), respectively. From Fig. 4.71, it is clear that the bridging stress is a function of the bridging ligament's position, x . Thus, by carrying out the integration in eqns. (4.41) and (4.42), the bridging contributions to the effective stress intensity factor and the equilibrium crack face displacement can be rewritten as

$$K_{bridge} = 2\sqrt{\frac{a}{\pi}} \sum_{i=1}^n \sigma(x_i) \left\{ \sin^{-1} \sqrt{\frac{a+x_i+t}{2a}} - \sin^{-1} \sqrt{\frac{a+x_i-t}{2a}} + \sin^{-1} \sqrt{\frac{a-x_i+t}{2a}} - \sin^{-1} \sqrt{\frac{a-x_i-t}{2a}} \right\} \quad (4.45)$$

and

$$v_{bridge}(x) = \frac{\kappa + 1}{4G\pi} 2\sqrt{a^2 - x^2} \sum_{i=1}^n \sigma(x_i) \left\{ \sin^{-1} \left(\frac{x_i+t}{a} \right) - \sin^{-1} \left(\frac{x_i-t}{a} \right) \right\} \quad (4.46)$$

where x_i is the position of the center of the i th bridging ligament, and t is the half thickness or radius of the bridging ligament for the ductile plate and fiber, respectively. Substituting eqns. (4.43) - (4.46) into (4.41) and (4.42), the effective stress intensity and the crack face displacement profile can be calculated for any combination of the externally applied stress and bridging tractions.

4.7.2 Computation of the Crack Growth Resistance

To utilize eqns. (4.41) and (4.42), the bridging stresses across the crack face must be determined from the equilibrium crack face displacement profile which in turn depends on the bridging and external stresses. Thus, an approach similar to the iterative

approach [134,135,189] has been taken to obtain the self-consistent crack face displacement profile. For the propose of illustration, the procedure to find the crack-growth resistance for a given crack of length $2a$ are outlined below.

1. Choose an external stress, σ_*^i , slightly larger than the fracture stress for the unreinforced matrix with a crack of length $2a$.
2. Compute the crack opening profile, $v_{ext}^i(x)$, due to the external stress σ_*^i using eqns. (4.43) and (4.44).
3. Assuming an equilibrium crack opening profile $v^j(x)$ using eqn. (4.44) with a stress σ^j much smaller than σ_*^i , calculate the corresponding bridging stress distribution $\sigma_{bridge}^j(x)$ using the ductile phase constitutive relations derived in Section 4.5.
4. Calculate the crack opening profile $v_{bridge}^j(x)$ due to the $\sigma_{bridge}^j(x)$ using eqn. (4.46).
5. Check eqn. (4.42). If $v^j(x) = v_{ext}^i(x) - v_{bridge}^j(x)$, then the assumed $v^j(x)$ is the equilibrium crack opening profile. If not, repeat step 3, 4 and 5 but with a new σ^{j+1} slightly larger than σ^j until eqn. (4.42) is satisfied or
 $v^j(x) - \{ v_{ext}^i(x) - v_{bridge}^j(x) \} < 0.1\% v^j(x)$.
6. After the equilibrium crack opening profile is found, K_{tip} is calculated using eqns. (4.41), (4.43) and (4.45). The σ_i in eqn. (4.45) is determined from $v(x)$ using the ductile phase constitutive relations derived in Section 4.5.
7. If $(K_m - K_{tip}) < 1\% K_m$, then the crack-growth resistance K_C is calculated from eqn. (4.36) or (4.43). If not, repeat steps 1 to 7 with a new external stress, σ_*^{i+1} , slightly larger than σ_*^i until the inequality is satisfied. For this study, $K_m = 3.3$ MPa.m $^{1/2}$ is used which is the fracture toughness of MoSi₂ matrix measured for the present MoSi₂/Nb system.

4.7.3 Typical R-Curve Behavior of Ductile-Phase-Reinforced Composites

A calculated curve of the crack-growth resistance vs. crack extension has been

shown in Fig. 4.72. For the present computation, laminated composites are assumed and the crack propagation is supposed to be normal to the ductile laminae. In addition, the initial crack length is assumed to be the distance between two consecutive ductile laminae. Then the crack-growth resistance is calculated correspondingly (see Section 4.7.2). This calculation rule is also followed in the rest of this chapter, unless otherwise mentioned. As expected, the crack-growth resistance increases initially as the crack extends (from the original crack size to point B), because more and more ductile laminae participate in bridging. However, as the crack extends more, this general trend may change because another competitive factor becomes pronounced, that is, the central ductile ligaments neck down or even fracture due to the large crack face displacement at the center of the crack. At a certain crack length (point B), the computation exhibits a bifurcation: one shows increasing K_c and the other decreasing K_c as the crack extends. Note that the initial curve before point B has $K_{tip} = 3.3$ MPa.m^{1/2}, while after point B the value of K_{tip} for the upper and lower curves are not equal. The reason for this discrepancy will be provided below from the examination of the equilibrium crack opening profile and bridging stress distribution as a function of the crack length.

The equilibrium crack opening profile and bridging stresses across crack face for different crack lengths are shown in Fig. 4.73 where (a), (b) and (c) correspond to the conditions marked as A, B and C in Fig. 4.72. As can be seen, for all conditions, the crack opening becomes much smaller with the presence of bridging ligaments than the unbridged crack. At small crack length (Fig. 4.73(a)), the maximum bridging stress is almost at the center of the crack. As the crack length increases, the maximum bridging stress moves toward the vicinity of the crack tip (Fig. 4.73(b) and (c)). When the crack is long, it is found that the profiles of the equilibrium crack opening and bridging stresses become very sensitive to the external stress at a certain level of loading (to be discussed more in Section 4.7.8), as shown in Fig. 4.73(c) (note $K_{ext} \propto$

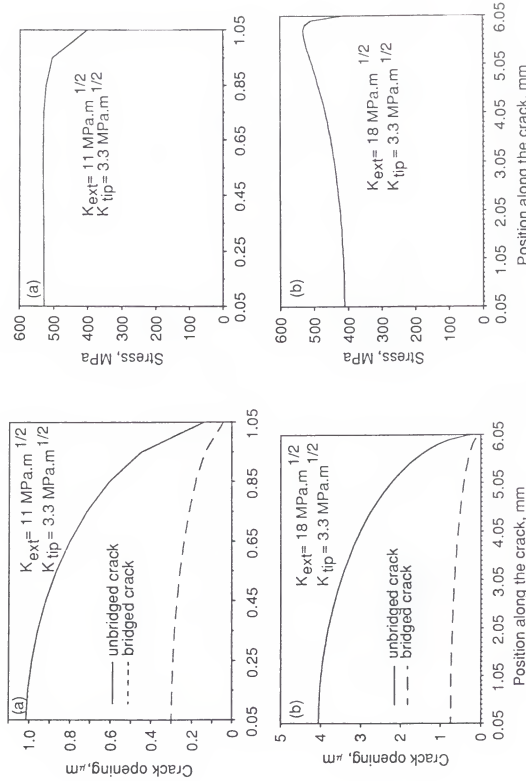


Fig. 4.73 Caption overleaf.

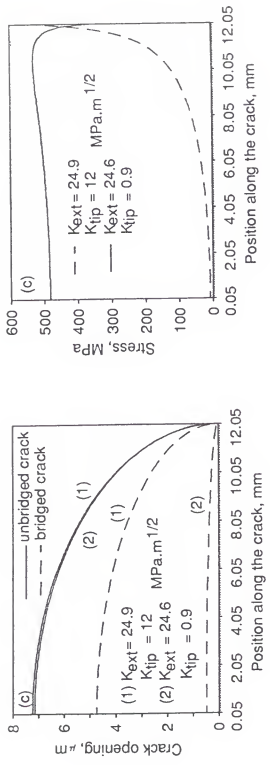


Fig. 4.73 The equilibrium crack opening profile and the corresponding bridging tractions. Crack length, $2a$, is 2.1 mm in (a), 12.1 mm in (b) and 24.1 mm in (c). Figures (a), (b) and (c) correspond to A, B and C in Fig. 4.72, respectively.

σ_0). Correspondingly, the effective stress intensity K_{tip} changes sharply from 0.9 to 12.0 MPa.m^{1/2} when K_{ext} increases only by 0.3 MPa.m^{1/2} (about 1% increase in K_{ext}). The sharp increase in the effective stress intensity is due to the dramatic decrease in the bridging stresses because of the necking of the central ligaments, as indicated in Fig. 4.73(c). The result implies that $K_{ext} = 24.6$ MPa.m^{1/2} at point C may not be dependable because a very small disturbance in the external stress could make K_{tip} jump from 0.9 to 12 MPa.m^{1/2}, a value much higher than the fracture toughness of the matrix (3.3 MPa.m^{1/2}). Furthermore, if the opening of the crack center is examined as a function of crack length as presented in Fig. 4.74, it is found that the opening of the crack center increases gradually as the crack extends from the original crack size to point B. However, a bifurcation occurs at point B. After point B, the upper curve where $K_{tip} >> K_m$ (3.3 MPa.m^{1/2}) exhibits a fast increase in the opening of the crack center, indicating that the ligament necking becomes dominant after a certain crack extension. In contrast, the lower curve where $K_{tip} << 3.3$ MPa.m^{1/2} has a opening smaller than that at point B, suggesting an impossible physical state because it implies that the crack closure happens when the crack extends. Therefore, the upper curve in Fig. 4.74 is taken as the real behavior of the composites. Correspondingly, the lower curve after point B in Fig. 4.72 computed from the larger crack opening ($K_{tip} >> 3.3$ MPa.m^{1/2}) is considered as the representative crack-growth resistance of the composite. Thus, point B in Fig. 4.72 is regarded as the point where the unstable crack propagation begins and the crack-growth resistance at point B is considered as the maximum crack-growth resistance, $K_c(max)$, available for the composite. The other two important parameters describing the characteristics of the R-curve are the initial slope of the curve and the crack length, $a_c(max)$, corresponding to the $K_c(max)$. The former dominates the crack-growth resistance when the crack is small, while the latter indicates the sensitivity of ductile phase toughening to the crack length.

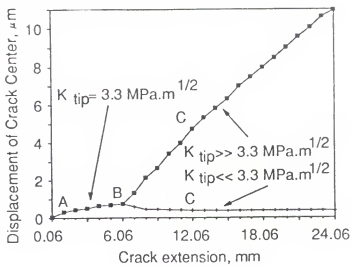


Fig. 4.74 The equilibrium displacement of crack center as a function of crack extension. The A, B and C correspond to those in Fig. 4.72 and the calculation parameters are the same as Fig. 4.72.

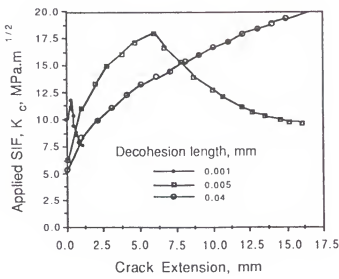


Fig. 4.75 R-curve behaviors of composites with different decohesion lengths at the interface. (20 vol% of Nb)

4.7.4 Prediction of the Effect of Matrix/Reinforcement Interface on Toughness

The crack-growth resistance curves of the composites with different interfacial decohesion length are presented in Fig. 4.75. It can be seen that the maximum crack-growth resistance increases with increasing decohesion length, while the initial slope of the crack-growth resistance is sharper for the short decohesion composites than for the long decohesion counterparts. Because of the sharper slope of the R-curve, the short-decohesion composite has a larger crack-growth resistance than the long-decohesion counterpart when crack is small. Decohesion length at the interface has been shown to be related to the fracture energy of the interface, i.e., the higher the fracture energy of the interface, the shorter the decohesion length (Section 4.5.2). Furthermore, it has been shown in Section 4.6.1 that the fracture energy of the chevron notched MoSi₂/Nb composites increased, while the peak load to fracture the same specimens decreased with decreasing the fracture energy of the interface, a paradox in choosing the bonding strength of the interface. The present theoretical analysis also suggests a trade-off in the selection of the interfacial properties, that is, if short cracks are the main concern of the composite, a relatively strong interface should be tailored. On the other hand, if the composite is to sustain large cracks, a relatively weak interface should be designed. Finally, it should be noted that a very weak interface (decohesion length = 0.04 mm) may not be desirable because the large toughening is reached only after extensive crack propagation.

4.7.5 Prediction of the Effect of Size of Ductile Phase on Toughness

If different sizes of Nb laminae are assumed to have the same intrinsic mechanical properties, then the corresponding R-curves of the composites are those presented in Fig. 4.76. It is noted that although the composites contain different sizes of ductile phases, the overall R-curve behaviors are very similar, i.e., the crack-growth resistances follow a similar locus as crack extends. However, the maximum crack-

growth resistance increases with increasing size of the ductile phase, indicating that large size of ductile phase is more capable of toughening when crack is large. This analysis is consistent with the experiments on the chevron notched composites where the initial crack length is about 1 mm, as shown in Section 4.6 and in Reference 132.

For engineering applications, the crack size is usually smaller than few millimeters. Thus, if we concentrate on the region of small crack size ($2a < 6$ mm) and enlarge that portion, we have Fig. 4.77. Because the calculation is carried out on the basis of constant volume fraction of ductile phase, the initial crack size (assumed to be equal to the distance between two consecutive ductile reinforcements) increases with increasing size of ductile phase. Before the crack grows to the initial crack size, the crack-growth resistance of the composite is regarded to be equal to the matrix toughness unless there is a residual compressive stress developed in the matrix and/or a strong toughening from the ductile phase shielding is present. The latter is usually small [23]. For the case of no residual stresses, therefore, the toughening comes earlier for small size of ductile reinforcement than for large size of the reinforcement, as shown in Fig. 4.77. This is better appreciated if the R-curve is converted to the fracture stress of the composites using the equation of

$$\sigma_f = \frac{K_c}{\sqrt{\pi a}} \quad (4.47)$$

The result is presented in Fig. 4.78. As can be seen, at the region of small crack size the composite containing small size of ductile phases has a much higher fracture stress than those containing larger ductile phases. For example, if the initial crack size is limited to 80 μm , then the composite containing 20 μm size of ductile phase has a fracture stress of about 460 MPa, while the counterpart with 125 μm size ductile phase has only a fracture stress of about 280 MPa. Therefore, analogous to the effect of the interface, the selection of the size of ductile phases depends on the major crack size to be dealt with.

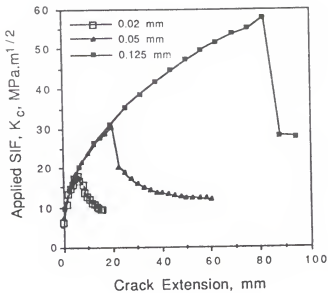


Fig. 4.76 R-curve behaviors of composites with different sizes of Nb laminae (20 vol% of Nb).

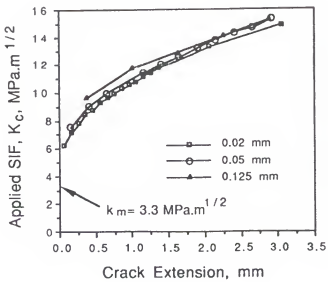


Fig. 4.77 An enlarged view of the R-curves at the region of the small crack size in Fig. 4.76.

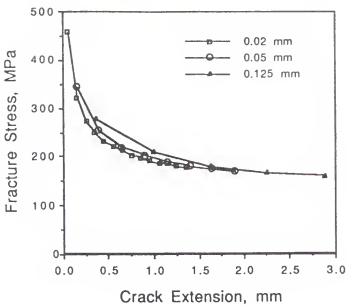


Fig. 4.78 Fracture stresses of the composites with different sizes of Nb laminae, calculated from the data in Fig. 4.77.

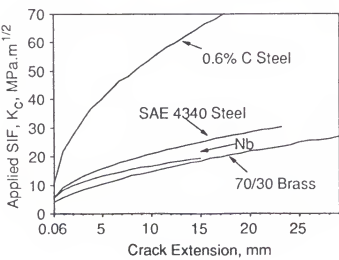


Fig. 4.79 R-curves of the composites containing different ductile laminae. Volume fraction of the ductile laminae are 20 % for all the composites.

4.7.6 Prediction of the Effect of the Intrinsic Properties of Ductile phase on Toughness

The intrinsic properties of the ductile phases used in the calculation are obtained from Reference 185 and have been listed in Table 4.13. The corresponding R-curves are presented in Fig. 4.79. It is noted that the best toughening is achieved by 0.6% C Steel which has the highest elastic modulus and yield strength among the ductile phases considered. 4340 steel has a similar elastic modulus and work hardening rate to 0.6% C Steel, but it exhibits a much lower toughening than 0.6% C Steel, indicating a strong influence of the yield strength. Comparison between 4340 steel and Nb suggests that higher elastic modulus has better toughening, because 4340 steel and Nb have similar yield strengths and work hardening rates but different elastic moduli. Effect of work hardening rate can be obtained by comparing 70/30 brass with Nb both of which have similar elastic moduli. Although 70/30 brass has a higher work hardening rate, it shows a lower toughening than Nb at small crack size but a large toughening after extensive crack propagation, indicating the yield strength has a better toughening than work hardening rate at small crack size.

Based on the above discussion, it can be summarized that the maximum crack-growth resistance increases as the yield strength, elastic modulus and work hardening rate of ductile phases increase. However, the yield strength and elastic modulus are more efficient in enhancing toughening than work hardening rate in the sense that the formers can provide high crack-growth resistance at a relatively short crack length while the latter provides large toughening only after extensive crack propagation. Similar results were also found by Ravichandran [135] and Cox [136].

4.7.7 Prediction of the Effect of Volume Fraction of Ductile Phase on Toughness

The R-curves of the composites with different volume fraction of ductile phase are presented in Fig. 4.80. As expected, high volume fraction of ductile reinforcement gives rise to not only a high maximum crack-growth resistance but also a sharp initial

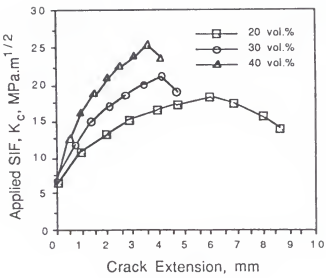


Fig. 4.80 Effect of volume fraction of ductile phase on the R-curve behavior of the composites containing Nb laminae with a thickness of 0.02 mm and a decohesion length of 0.005 mm at the interface.

Table 4.18 Comparison of Composite Toughness Calculated by Different Methods
(SSB and LSB)

	Effect of size of ductile phase (a) (Thickness of Nb, mm)	Effect of the interface (b) (Decohesion length, mm)	Effect of volume fraction (c)
	0.125	0.05	0.02
		0.001	0.005
		0.04	0.04
$K_c(\text{SSB})$ (MPa.m $^{1/2}$)	30.2	19.2	12.4
		6.7	12.4
		22.0	12.4
		18.2	18.2
$K_c(\text{max})$ (MPa.m $^{1/2}$)	57.7	30.4	17.8
		11.7	17.8
		>33	17.8
			21.5
			25.8

(a) Vol.% of Nb = 20%; Cohesion length are 0.0312, 0.0125 and 0.005 mm for 0.125, 0.05 and 0.02 mm Nb, respectively.

(b) Thickness of Nb = 0.02 mm; Vol. % of Nb = 20%.

(c) Thickness of Nb = 0.02 mm; Cohesion length = 0.005 mm.

slope of the R-curve. However, the maximum crack-growth resistance occurs at a smaller crack length when the volume fraction increases, indicating that the toughening becomes more sensitive to the crack length as the volume fraction increases.

At this point, a comparison can be made between the calculations based on the assumption of the small-scale bridging and the large scale bridging. The conclusions made in Section 4.5 are based on the assumption of small-scale bridging, and the fundamental equations in SSB have been shown in Section 2.3 (eqns. (2.6) and (2.7)). The results calculated using eqns. (2.6) and (2.7) are listed in Table 4.18 and are compared to the present large-scale-bridging calculations. Since the crack-growth resistance varies with the crack extension in the present large-scale-bridging calculations, the maximum crack-growth resistance $K_c(\max)$ is taken for the comparison. As expected, the two methods lead to different toughnesses, a result also found by Ravichandran [135]. For the comparison listed in Table 4.18, the large-scale-bridging exhibits a higher toughness. However, if the crack-growth resistance after passing the $K_c(\max)$ is used to compare with the steady-state toughness, it is found that $K_c(SSB)$ shows a higher toughness. For example, a composite containing 0.02 mm thick Nb laminae exhibits a crack-growth resistance of about $9 \text{ MPa.m}^{1/2}$ after passing $K_c(\max)$ (Fig. 4.76), in contrast with $12.36 \text{ MPa.m}^{1/2}$ calculated from the small-scale-bridging method. The discrepancy lies obviously in the different assumptions for the two approaches. However, since large-scale bridging is more appropriate for the ductile-phase-toughened composites, it is expected to provide a better estimation.

4.7.8 Prediction of the Effect of Properties of Matrix on Toughness

Effect of the matrix toughness on ductile phase toughening can be evaluated from Fig. 4.81 which shows how various stress intensity factors change with the externally applied stress for a given crack length. If a certain point of the external stress in Fig. 4.81 is taken as the stress to propagate the crack, then the corresponding

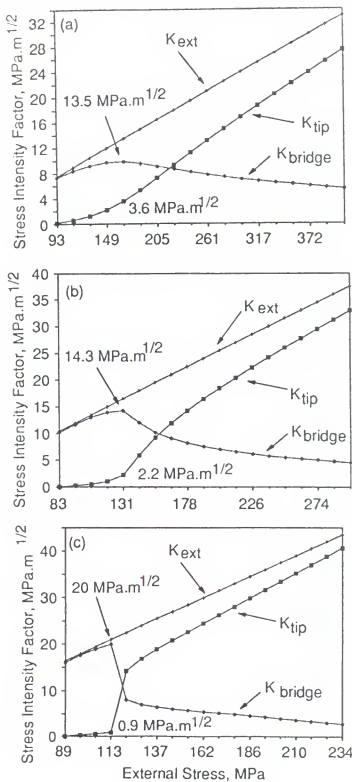


Fig. 4.81 Various stress intensity factors vs external stress at given crack lengths: (a) $a = 2.06 \text{ mm}$; (b) $a = 5.06 \text{ mm}$; and (c) $a = 10.06 \text{ mm}$. The composite contains 20 vol.% of Nb laminae with a thickness of 0.02 mm and a decohesion length of 0.005 mm at the interface.

values of K_{ext} , K_{tip} and K_{bridge} can be regarded as the crack-growth resistance of the composite, the fracture toughness of the matrix and the bridging contribution at the time of the propagation, respectively. The stress intensity numbers listed in the figure indicate the maximum bridging contribution available for the given conditions and the corresponding matrix toughness. Thus, from the Fig. 4.81 it is noted that the bridging contribution depends on the fracture toughness of the matrix. If the toughness of the matrix is low, the bridging contribution will account for most of the crack-growth resistance of the composite. However, when the toughness of the matrix is high ($K_m > 10 \text{ MPa.m}^{1/2}$), the bridging contribution becomes not only smaller in magnitude but a small portion of the crack-growth resistance as well. This result is believed to be related to the following scenario. When the matrix toughness is low, the crack opening must be small and most of the external load will be carried by the bridging ligaments before the crack propagates, leading to a large contribution from ductile phase. In contrast, when the matrix toughness is high, the crack opening has to be increased to produce enough stress intensity at the crack tip before the crack can propagate. As such, the bridging ligaments at the central portion of the crack will neck down, resulting in less contribution from the bridging ligaments.

The above discussion indicates that when the matrix has a high toughness ($K_m > 10 \text{ MPa.m}^{1/2}$), ductile phase toughening is not efficient unless a ductile phase with a high work hardening rate and a weak interface has been utilized. Both of these material properties prevent ductile ligaments from necking. In reality, however, almost all the brittle materials have toughness below $10 \text{ MPa.m}^{1/2}$, therefore a more important aspect is what material properties affect the transition of the bridging contribution from high percentage to low percentage of the crack-growth resistance, and how to control these properties for optimal ductile phase toughening. From Fig. 4.81, it is obvious that the transition is affected by the crack length, i.e., the longer the

crack length, the lower the matrix toughness at which the transition occurs. Besides, the transition also becomes sharper when the crack length increases.

The transition is also affected by the decohesion length at the interface. Comparison between Fig. 4.81 and 4.82 manifests that if the decohesion length is large, the transition becomes much gentler or might even shows no decrease in the magnitude of the bridging contribution (Fig. 4.82(a)). It is also noted that the transition occurs at a higher matrix toughness when the decohesion is long. For example, the matrix toughness at which the bridging contribution begins to decrease changes from 2.2 to 5.1 MPa.m^{1/2} when the decohesion length changes from 0.005 to 0.04 mm for a crack with $a = 5.06$ mm (Fig. 4.81(b) and 4.82(b)). The results suggest that when the matrix toughness is high, a relatively weak interface (thus a long decohesion length) would be desirable to enhance bridging contribution, otherwise the bridging contribution would be too sensitive to the size of the existing crack. On the other hand, if the matrix toughness is low, a relatively strong interface may be beneficial to limiting the bridging length and producing a higher crack-growth resistance at a shorter crack length.

Effect of the volume fraction of the ductile phase on the transition is presented in Fig. 4.83. Comparison between Fig. 4.81 and 4.83 reveals that the transition becomes sharper with increasing volume fraction of ductile phase, or in other words, it becomes more sensitive to the crack length. However, a much higher bridging contribution at the onset of the transition is reached by the high volume fraction of the ductile phase. For instance, 23.5 and 14.3 MPa.m^{1/2} of the bridging contributions is obtained at the onset of the transition for 40 and 20 vol.% of the ductile phase, respectively (Fig. 4.81(b) and 4.83(b)).

The effects of various material properties on the transition can also be deduced from the R-curves (Fig. 4.75, 4.76, 4.79 and 4.80). Increasing the matrix toughness will shift the R-curve upward and increase the initial slope of the curve, but move

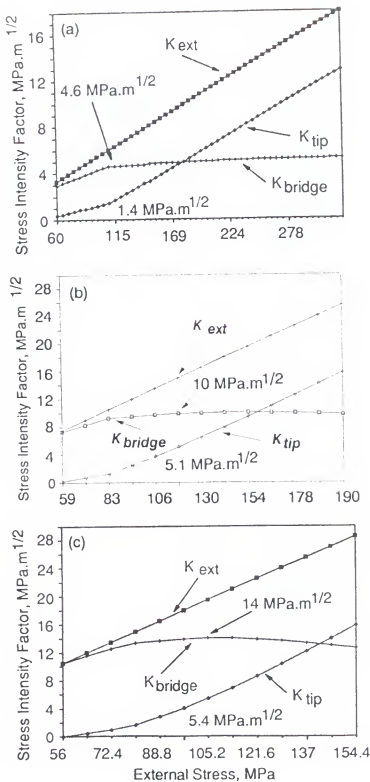


Fig. 4.82 Various stress intensity factors vs external stress at given crack lengths: (a) $a = 1.0 \text{ mm}$; (b) $a = 5.06 \text{ mm}$; and (c) $a = 11.06 \text{ mm}$. The composite contains 20 vol.% of Nb laminae with a thickness of 0.02 mm and a decohesion length of 0.04 mm at the interface.

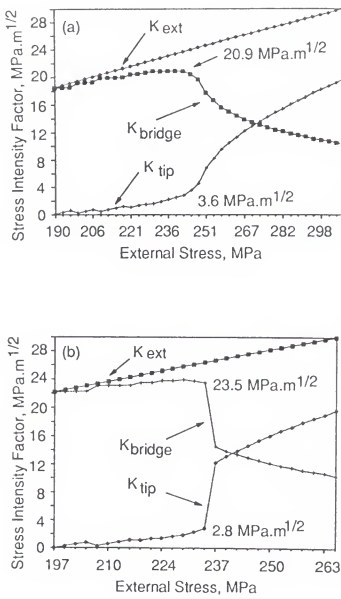


Fig. 4.83 Various stress intensity factors vs external stress at given crack lengths: (a) $a = 3.035 \text{ mm}$ and (b) $a = 4.035 \text{ mm}$; and (c) $a = 11.06 \text{ mm}$. The composite contains 40 vol.% of Nb laminae with a thickness of 0.02 mm and a decohesion length of 0.005 mm at the interface.

$a_c(\max)$ to a smaller crack size. Based on such reasoning, the selection of material properties can be made by referring to the R-curves. For example, if a matrix with a higher toughness than that shown in Fig. 4.75 is to be ductile-phase-toughened, the decohesion length of 0.001 mm is obviously not a good choice because the composite would be even more sensitive to the size of the existing crack. From Fig. 4.76, the transition is expected to be insensitive to size of the ductile phase, because different sizes of ductile phases follow a similar locus of the crack-growth resistance. Fig. 4.79 suggests that a high work hardening rate material such as 70/30 brass would be less sensitive to the matrix toughness and the crack size. In a word, the effects on the ductile phase toughening of the matrix toughness, the bonding strength of the interface, and the intrinsic properties, size and volume fraction of the ductile phase are interdependent with each other. The selection of these material properties should be based on the crack size being concerned and the matrix toughness.

In summary, from the analysis of the large-scale bridging, the following conclusions can be made:

1. Ductile-phase-toughened composites will exhibit a rising crack-growth resistance (R-curve) which can be characterized by three parameters: the maximum crack-growth resistance $K_c(\max)$, the corresponding crack length $2a_c(\max)$, and the initial slope of the R-curve. Crack-growth resistance is mainly determined by the initial slope of the R-curve when crack is small and is dominated by the maximum crack-growth resistance when crack is large.
2. The maximum crack-growth resistance increases with decreasing the fracture energy of the matrix/reinforcement interface. However, $2a_c(\max)$ increases as well, suggesting that $K_c(\max)$ is reached only after extensive crack propagation. On the other hand, the interface with a high fracture energy has a high initial slope of the R-curve. The duality of the interface suggests that a weak interface would be desirable if the

cracks concerned are long, and a strong interface would be beneficial if the cracks to be dealt with are short.

3. The overall R-curve behaviors of composites with different sizes of ductile phases are very similar; they follow a similar locus as crack extends. However, $K_c(\max)$ increases with increasing size of ductile phase, indicating that large size of ductile phases are more capable of toughening when cracks are large. When the cracks are small ($2a < 200 \mu\text{m}$) which is of great interest to the engineering applications, composites containing small size of ductile phases show a higher fracture stress than the counterparts with large size of ductile phases. This paradox is very similar to the choice of the interface, i.e., selecting these properties depends on the crack size concerned.

4. $K_c(\max)$ increases with increasing yield strength, elastic modulus and work hardening rate of ductile phases. However, the yield strength and elastic modulus are more efficient in enhancing toughening than work hardening rate in the sense that the formers can provide high crack-growth resistance at a relatively short crack length, while the latter provides large toughening only after extensive crack propagation.

5. High volume fraction of ductile reinforcement gives rise to not only a high $K_c(\max)$ but also a sharp initial slope of the R-curve. But $2a_c(\max)$ also becomes smaller when the volume fraction increases, indicating that the toughening becomes more sensitive to the crack length as the volume fraction increases.

6. When the matrix toughness is low, a ductile phase with high yield strength and elastic modulus and a relatively strong interface would be desirable to produce a high crack-growth resistance at a short crack length. If the matrix toughness is high, other material properties, such as weak interface and high-work-hardening-rate materials which prevent bridging ligaments from necking, should be chosen to enhance bridging contribution.

CHAPTER FIVE CONCLUSIONS

Ductile phase toughening in brittle matrices for high temperature structural applications has been investigated. Owing to the projected use temperatures, the system selected for the study was MoSi₂ matrix and Nb ductile reinforcements. The main conclusions from this study are as follows.

1. For controlling the matrix/reinforcement interaction, chemical compatibilities of various potential coating materials (mullite, Al₂O₃, and ZrO₂) with MoSi₂ and Nb were studied via microstructural and compositional analyses. Based on these analyses, Al₂O₃ was chosen as the final diffusion barrier coating because it is chemically compatible with both MoSi₂ and Nb, and it also has a thermal expansion coefficient close to those of both the matrix and reinforcement.
2. The techniques investigated for producing Al₂O₃ coating on Nb surface included (1) sol-gel processing; (2) physical vapor deposition; (3) hot dipping the reinforcement in molten aluminum, followed by anodizing Al to form Al₂O₃. The results indicated that a thick and dense Al₂O₃ coating is necessary for effective elimination of the interactions between Nb and the matrix of commercially pure MoSi₂. The results also showed that the best coating is provided with physical vapor deposition, followed by the sol-gel technique.
3. Effects of the matrix/reinforcement interface, the mechanical properties and size of the ductile phase on the flow behavior of constrained ductile phases were evaluated via tensile tests on a single Nb lamina imbedded in MoSi₂ matrix. An approximate model was proposed which, according to the small-scale-bridging

assumption, gave the following conclusions: the toughness of the composites is enhanced by a relatively weak bond at the matrix/reinforcement interface, by a large size of ductile reinforcements, and by a ductile phase with a high yield strength and high work hardening rate.

4. The role of the matrix/reinforcement interface in the fracture toughness of MoSi₂/Nb composites was assessed via four-point bend tests on chevron notched specimens. It has been established that whether or not a strong interfacial bonding is conducive to toughness depended on the criterion used to describe the toughness of the composites. If the peak load of the chevron notched specimen is used as an indicator of the toughness, a strong bonding would be desirable. On the other hand, if the total energy consumed to break a specimen is used as indicative of its toughness, then a relatively weak bonding is preferable.

5. Four-point bend tests were used to evaluate the effects of the size and orientation of ductile laminae on the toughness of the composites. The results indicated that toughness of the composites increased with increasing size of Nb laminae, and that ductile laminae offered two dimensional toughening. The fracture toughness in the two orientations (N- and T-orientations) has been increased to about 11 - 14 MPa.m^{1/2} from 3 MPa.m^{1/2} for the unreinforced matrix.

6. All the toughness evaluations and the examination of the interaction of cracks with ductile reinforcements in the present study indicated that (1) ductile phase toughening involved large-scale bridging, i.e., the bridging-length was at the same magnitude as the crack length, the specimen size or the distance from the crack to the specimen boundaries, and (2) the toughening of brittle matrix with ductile phase could be described by the equilibrium stress distribution across the crack face.

7. According to the aforementioned observations, a general approach has been proposed to compute the ductile phase toughening in the case of large-scale-bridging. The approach, which allowed for the prediction of the typical R-curve behaviors of

ductile-phase-toughened composites, encompassed the effects of the bonding strength of the matrix/reinforcement interface, the size of ductile phases, and the intrinsic mechanical properties of the ductile phases and matrix. From the analysis of the large-scale bridging, the following conclusions can be made: (1) Ductile-phase-toughened composites will exhibit a rising crack-growth resistance (R-curve) which can be characterized by three parameters, i.e., the maximum crack-growth resistance $K_c(\max)$, the corresponding crack length $2a_c(\max)$, and the initial slope of the R-curve. Crack-growth resistance is mainly determined by the initial slope of the R-curve when crack is small and by the maximum crack-growth resistance when crack is large. (2) The interface with a short decohesion length gives rise to a steeper initial slope of R-curve, while $K_c(\max)$ increases with the decohesion length at the interface. The duality of the interface suggests that a weak interface would be desirable if the crack concerned are long, but a strong interface would be beneficial if the cracks to be dealt with are short. (3) $K_c(\max)$ increases with increasing size of the ductile phase, indicating that large size of ductile phases are more capable of toughening when cracks are large. When the cracks concerned are small ($2a < 200 \mu\text{m}$) which is of great interest to the engineering applications, composites containing small size of ductile phases show a higher fracture stress than the counterparts with large size of ductile phases. This paradox is very similar to the choice of the interface, i.e., selecting these properties depends on the crack size concerned. (4) $K_c(\max)$ increases with increasing yield strength, elastic modulus and work hardening rate of ductile phases. (5) High volume fraction of ductile reinforcement gives rise to not only a high $K_c(\max)$ but also to a sharp initial slope of the R-curve. (6) When the matrix toughness is low, a ductile phase with high yield strength and elastic modulus and a relatively strong interface would be desirable to produce a high crack-growth resistance at a not very long crack length. If the matrix toughness is high, other material properties, such as weak

interface and high-work-hardening-rate materials which prevent bridging ligaments from necking, should be chosen to enhance bridging contribution.

APPENDIX
FINITE ELEMENT ANALYSIS OF STRESS DISTRIBUTION ACROSS THE
NECK OF THE CONSTRAINED DUCTILE PHASES

Finite element analysis (FEA) of the stress distribution across the neck and the contour of the decohesion region during the elastic deformation was implemented using the finite element software package ANSYS. Due to the symmetry, only one quarter of the specimen was analyzed using two-dimensional 4-node isoparametric elements with an assumption of plane strain deformation. A typical finite element model for the constrained Nb is shown in Fig. A. The displacement at the midplane of the neck was allowed only in the x-direction, and the bonded boundary of Nb to the matrix and the axial central plane were allowed to displace only in z-direction, as shown in Fig. A.

Results from the FEA for the case of constrained 1.0 mm Nb lamina with 2.28 mm decohesion length under a nominal axial stress of 150 MPa are presented in Figures B-D. Figure B compares the assumed contour of the decohesion region with the FEA result. The data show that the assumed contour deviates from the FEA result, leading to a smaller crack opening displacement compared to the finite element analysis. However, the difference is so small that it introduces negligible errors to the computation of the work of rupture. Evaluation of effective stress distribution across the midplane of the neck is shown in Fig. C. Clearly, the effective stress is not constant across the midplane, but increases from the free surface to the center of the neck. Although the assumed constant effective stress does not represent the real stress distribution, the mean axial stresses across the midplane are almost the same for the model and FEA, as shown in Fig. D. Thus, it is concluded that the assumed constant effective stress and contour of the decohesion region impose negligible errors on the calculation of σ - u curve and the work of rupture.

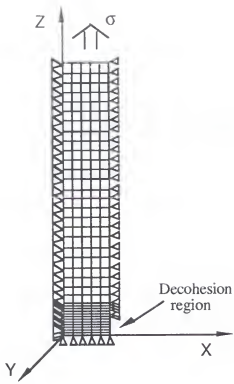


Fig. A Mesh and boundary conditions used for the analysis of constrained Nb.

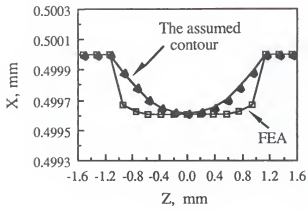


Fig. B A comparison between the assumed contour and finite element analysis of the decohession region during the stage of elastic deformation. X and Z are defined in Fig. A.

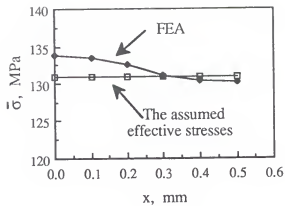


Fig. C Effective stress distribution at the midplane of neck.

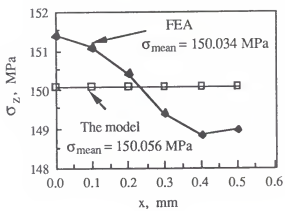


Fig. D A comparison of the axial stresses at the midplane of neck between the model and FEA. Note that mean axial stresses, σ_{mean} , are almost the same.

REFERENCES

1. P. F. Becher and G. C. Wei, *J. Am. Ceram. Soc.*, 1984, vol. 67, pp. C267-C269.
2. G. C. Wei and P. F. Becher, *Am. Ceram. Soc. Bull.*, 1985, vol. 64, pp. 298-304.
3. R. Hayami, K. Ueno, I. Kondou, N. Tamari and Y. Toibana, in *Tailoring MultiPhase and Composite Ceramics*, vol.20, edited by R. E. Tressler, G. L. Messing, C. G. Pantano and R. E. Newnham, Plenum Press, New York, 1986, pp. 663-674.
4. S. T. Buijan, J. G. Baldoni and M. L. Huckabee, *Am. Ceram. Bull.*, 1987, vol. 66, p. 347.
5. R. Lundberg, L. Kahlman, R. Pompe and R. Carlsson, *Am. Ceram. Bull.*, 1987, vol. 66, p. 330.
6. P. D. Shalek, J. J. Petrovic, G. F. Hurley and F. D. Gac, *Am. Ceram. Bull.*, 1986, vol. 65, pp. 351-356.
7. K. P. Gadjaree and K. Chyung, *Am. Ceram. Soc. Bull.*, 1986, vol. 65, pp. 370-376.
8. F. D. Gac, J. J. Petrovic, J. V. Milewski and P. D. Shalek, *Ceram. Eng. Sci. Proc.*, 1986, vol. 7, pp. 978-982.
9. P. C. Panda and E. R. Seydel, *Am. Ceram. Soc. Bull.*, 1986, vol. 65, pp. 338-341.
10. N. Claussen, K. L. Weisskopf and M. Ruhle, *J. Am. Ceram. Soc.*, 1986, vol. 69, 288-292.
11. N. Claussen, K. L. Weisskopf and M. Ruhle, in *Fracture Mechanics of Ceramics*, vol. 7, Plenum Press, New York, 1986, pp. 75-86.
12. P. F. Becher and T. N. Tiegs, *J. Am. Ceram. Soc.*, 1987, vol. 70, pp. 651-654.
13. P. F. Becher, T. N. Tiegs, J. C. Odle and W. H. Warwick, in *Fracture Mechanics of Ceramics*, vol. 7, Plenum Press, New York, 1986, pp. 61-73.

14. E. Fitzer and R. Gadow, Am. Ceram. Soc. Bull., 1986, vol. 65, pp. 326-335.
15. A. J. Caputo and W. J. Lackey, Ceram. Eng. Sci. Proc., 1984, vol. 5, pp. 654-667.
16. P. J. Lamicq, G. A. Bernhart, M. M. Dauchier and J. G. Mace, Am. Ceram. Soc. Bull., 1986, vol. 65, pp. 336-338.
17. J. W. Warren, Ceram. Eng. Sci. Proc., 1985, vol. 5, pp. 684-693.
18. R. T. Bhatt, in Tailoring Multiphase and Composite Ceramics, vol. 20, edited by R. E. Tressler, G. L. Messing, C. G. Pantano and R. E. Newnham, Plenum Press, New York, 1986, pp. 675-686.
19. J. J. Brennan, in Tailoring Multiphase and Composite Ceramics, vol. 20, edited by R. E. Tressler, G. L. Messing, C. G. Pantano and R. E. Newnham, Plenum Press, New York, 1986, pp. 549-560.
20. A. G. Evans and R. M. McMeeking, Acta Metall., 1986, vol. 34, pp. 2435-41.
21. C. A. Andersson and M. K. Aghajanian, Ceram. Eng. Sci. Proc., 1988, vol. 9, pp. 621-26.
22. S. Junz-Douglass, P. W. R. Beaumont and M. F. Ashby, J. Mater. Sci., 1980, vol. 15, pp. 1109-23.
23. L. S. Sigl, P. A. Mataga, B. J. Dalglish, R. M. McMeeking and A. G. Evans, Acta Metall., 1988, vol. 36, pp. 945-53.
24. P. A. Mataga, Acta Metall., 1989, vol. 37, pp. 3349-59.
25. B. Budiansky, J. C. Amazigo and A. G. Evans, J. Mech. Phys. Solids, 1988, vol. 36, pp. 167-87.
26. M. F. Ashby, F. J. Blunt and M. Bannister, Acta Metall., 1989, vol. 37, pp. 1847-57.
27. D. Broek, The Practical Use of Fracture Mechanics, Kluwer Academic Publishers, Boston, 1988.
28. A. A. Griffith, Phil. Trans. Roy. Soc. London, Ser. A, 1921, vol. 221, p. 163.
29. J. N. Goodier, in Fracture, vol. 2, edited by H. Liebowitz, Academic Press, New York, 1968, pp. 1-66.

30. G. R. Irwin, in Proc. 7th Sagamore Ordnance Mater. Res. Conf., vol. 4, Syracuse University Press, Syracuse, N.Y., 1961, pp. 63-78.
31. D. S. Dugdale, J. Mech. Phys. Solids, 1960, vol. 8, pp. 100-104.
32. J. R. Rice, in Fracture, vol. 2, edited by H. Liebowitz, Academic Press, New York, 1968, pp. 191-311.
33. J. R. Rice, J. Applied Mech., 1968, vol. 50, pp. 379-386.
34. K. Hellan, Introduction to Fracture Mechanics, McGraw-Hill Book Company, New York, 1984.
35. K. T. Faber and A. G. Evans, Acta Metall., 1983, vol. 31, pp. 565-76.
36. K. T. Faber and A. G. Evans, Acta Metall., 1983, vol. 31, pp. 577-84.
37. K. T. Faber and A. G. Evans, J. Am. Ceram. Soc., 1983, vol. 66, pp. c-94-c-96.
38. J. C. Swearengen, E. K. Beauchamp and R. J. Eagan, in Fracture Mechanics of Ceramics, vol. 4, Edited by R. C. Bradt, D. P. H. Hasselman and F. F. Lange, Plenum Press, New York, 1978, pp. 973-87.
39. D. H. Carter and G. F. Hurley, J. Am. Ceram. Soc., 1987, vol. 70, pp. c-76-c-81.
40. D. J. Green, P. S. Nicholson and J. D. Embury, J. Mater. Sci., 1977, vol. 12, pp. 987-89.
41. D. J. Green, P. S. Nicholson and J. D. Embury, J. Mater. Sci., 1979, vol. 14, pp. 1413-20.
42. A. K. Khaund and P. S. Nicholson, J. Mater. Sci., 1980, vol. 15, pp. 177-87.
43. H. Bethge, Phys. Stat. Sol., 1962, vol. 2, pp. 775-820.
44. G. T. Forwood and A. J. Forty, Phil. Mag., 1965, vol. 11, pp. 1057-82.
45. A. Briggs and D. H. Bowen, in Mass Transport in Oxides, edited by J. B. Wachtman and D. Franklin, NBS Special Publication 296, Washington, 1968, p.103.
46. E. M. Passmore, R. M. Spriggs and T. Vasilos, J. Am. Ceram. Soc., 1965, vol. 48, pp. 1-7.

47. K. A. D. Lambe, N. J. Mattingley and D. H. Bowen, 1967, A.E.R.E. Rep. R-5505, Ceramics Division Atomic Energy Research Establishment, Harwell.
48. R. A. J. Sambell, D. H. Bowen and D. C. Phillips, *J. Mater. Sci.*, 1972, vol. 7, pp. 663-75.
49. F. F. Lange and K. C. Radford, *J. Mater. Sci.*, 1971, vol. 6, pp. 1197-1203.
50. F. F. Lange, *J. Am. Ceram. Soc.*, 1971, vol. 54, pp. 614-20.
51. D. R. Biswas, *J. Mater. Sci.*, 1980, vol. 15, pp. 1696-1700.
52. A. K. Khaund, V. D. Krstic and P. S. Nicholson, *J. Mater. Sci.*, 1977, vol. 12, pp. 2269-73.
53. F. F. Lange, *Phil. Mag.*, 1970, vol. 22, pp. 983-92.
54. A. G. Evans, *Phil. Mag.*, 1972, vol. 26, pp. 1327-44.
55. A. G. Evans and L. J. Graham, *Acta Metall.*, 1975, vol. 23, pp. 1303-12.
56. D. J. Green, *J. Am. Ceram. Soc.*, 1983, vol. 66, pp. C-4-C-5.
57. F. F. Lange, *J. Mater. Sci.*, 1982, vol. 17, pp. 247-54.
58. F. F. Lange, U. S. Patent 4,316,964 (1982).
59. F. F. Lange, B. I. Davis and D. O. Raleigh, *J. Am. Ceram. Soc.*, 1983, vol. 66, pp. C-50-C-51.
60. J. S. Moya and M. I. Osendi, *J. Mater. Sci.*, 1983, vol. 2, pp. 599-601.
61. N. Claussen and J. Jahn, *J. Am. Ceram. Soc.*, 1980, vol. 63, pp. 228-29.
62. S. Prochazka, J. S. Wallace and N. Claussen, *J. Am. Ceram. Soc.*, 1983, vol. 66, pp. C-125-C-127.
63. Q. M. Yuan, J. Q. Tan and Z. G. Jin, *J. Am. Ceram. Soc.*, 1986, vol. 69, pp. 265-67.
64. Q. M. Yuan, J. Q. Tan, J. Y. Shen, X. H. Zhu and Z. F. Yang, *J. Am. Ceram. Soc.*, 1986, vol. 69, pp. 268-69.

65. G. Hoagland, G. T. Hahn and A. R. Rosenfield, *Rock Mech.*, 1973, vol. 5, pp. 77-105.
66. N. Claussen, *J. Am. Ceram. Soc.*, 1976, vol. 59, pp. 49-51.
67. M. P. Borom, A. M. Turkalo and R. H. Doremus, *J. Am. Ceram. Soc.*, 1975, vol. 58, pp. 385-91.
68. R. W. Davidge and T. J. Green, *J. Mater. Sci.*, 1968, vol. 3, pp. 629-34.
69. F. F. Lange, *J. Mater. Sci.*, 1982, vol. 17, pp. 235-39.
70. P. F. Becher, *Acta Metall.*, 1986, vol. 34, pp. 1885-91.
71. A. G. Evans and R. M. Cannon, *Acta Metall.*, 1986, vol. 34, pp. 761-800.
72. C. A. Andersson and T. K. Gupta, *Ceram. Eng. Sci. Proc.*, 1986, vol. 7, pp. 1150-57.
73. N. Claussen and M. Ruhle, *Adv. Ceram.*, 1981, vol. 3, p. 137.
74. M. Ruhle, N. Claussen and A. H. Heuer, *Adv. Ceram.*, 1984, vol. 11, p. 352.
75. M. V. Swain, *Fract. Mech. Ceram.*, 1983, vol. 6, p. 355.
76. A. G. Evans, *Acta Metall.*, 1978, vol. 26, pp. 1845-53.
77. D. R. Clarke, *Acta Metall.*, 1980, vol. 28, pp. 913-24.
78. D. W. Rice and R. C. Phanka, *J. Am. Ceram. Soc.*, 1979, vol. 62, pp. 559-63.
79. R. W. Rice and S. W. Freiman, *J. Am. Ceram. Soc.*, 1981, vol. 64, pp. 350-54.
80. R. G. Hoagland and J. D. Embury, *J. Am. Ceram. Soc.*, 1980, vol. 63, pp. 404-10.
81. A. G. Evans and K. T. Faber, *J. Am. Ceram. Soc.*, 1981, vol. 64, pp. 394-98.
82. J. W. Hutchinson, *Acta Metall.*, 1987, vol. 35, pp. 1605-19.
83. Y. Fu and A. G. Evans, *Acta Metall.*, 1982, vol. 30, pp. 629-34.
84. N. Claussen, J. Steeb and R. F. Pabst, *Am. Ceram. Soc. Bull.*, 1977, vol. 56, pp. 559-62.

85. C. Cm. Wu, S. W. Frieman, R. W. Rice and J. J. Mecholsky, *J. Mater. Sci.*, 1978, vol. 13, pp. 2659-70.
86. A. G. Evans and K. T. Faber, *J. Am. Ceram. Soc.*, 1984, vol. 67, pp. 255-60.
87. J. L. Pentecost, in *High-Temperature Inorganic Coatings*, edited by J. Huminik, Reinhold Publishing Corporation, New York, Chapman and Hall, Ltd., London, 1963, p. 26.
88. R. F. Cook, C. J. Fairbanks, B. R. Lawn and Y. W. Mai, *J. Mater. Res.*, 1987, vol. 2, pp. 345-56.
89. P. L. Swanson, C. J. Fairbanks, B. R. Lawn, Y. W. Mai and B. J. Hockey, *J. Am. Ceram. Soc.*, 1987, vol. 70, pp. 279-89.
90. B. D. Flinn, M. Ruhle and A. G. Evans, *Acta Metall.*, 1989, vol. 37, pp. 3001-3006.
91. L. Xiao, Y. S. Kim, R. Abbaschian and R. J. Hecht, *Mater. Sci. Eng.*, 1991, vol. A144, pp. 277-85.
92. M. A. Przstupa and T. H. Courtney, *Metall. Trans. A*, 1982, vol. 13, pp. 881-87.
93. G. Tradiff, Jr., *Eng. Fracture Mech.*, 1973, vol. 5, pp. 1-10.
94. M. S. Newkirk, H. D. Lesher, D. R. White, C. R. Kennedy, A. W. Urquhart and T. D. Claar, *Ceram. Eng. Sci. Proc.*, 1987, vol. 8, pp. 879-85.
95. J. L. Chermant and F. Osterstock, *J. Mater. Sci.*, 1976, vol. 11, pp. 1939-51.
96. P. F. Becher, C. H. Hsueh, P. Angelini and T. N. Tiegs, *J. Am. Ceram. Soc.*, 1988, vol. 71, pp. 1050-61.
97. P. F. Becher, *J. Am. Ceram. Soc.*, 1991, vol. 74, pp. 255-69.
98. F. D. Gac, J. J. Petrovic, J. V. Milewski and P. D. Shalek, *Ceram. Eng. Sci. Proc.*, 1986, vol. 7, pp. 978-82.
99. J. V. Milewski, U. S. Patent 4,513,030 (1985).
100. J. V. Milewski, *Adv. Ceram. Mater.*, 1986, vol. 1, p. 36.
101. P. D. Shalek, J. J. Petrovic, G. F. Hurley and F. D. Gac, *Am. Ceram. Soc. Bull.*, 1986, vol. 65, pp. 351-56.

102. K. M. Prewo and J. J. Brennan, *J. Mater. Sci.*, 1980, vol. 15, pp. 463-68.
103. K. M. Prewo and J. J. Brennan, *J. Mater. Sci.*, 1986, vol. 21, pp. 3590-3600.
104. K. T. Faber, *Ceram. Eng. Sci. Proc.*, 1984, vol. 5, pp. 408-39.
105. Z. B Ahmad, M. F. Ashby and P. W. R. Beaumont, *Scripta Metall.*, 1986, vol. 20, pp. 843-48.
106. L. R. F. Rose, *J. Mech. Phys. Solids*, 1987, vol. 35, pp. 383-405.
107. L. R. F. Rose, *International J. Fracture*, 1982, vol. 18, pp. 135-44.
108. D. B. Marshall, B. N. Cox and A. G. Evans, *Acta Metall.*, 1985, vol. 33, pp. 2013- 2021.
109. D. Lewis, in *International Encyclopedia of Composites*, vol. 1, edited by S. M. Lee, VCH Publishers, New York, 1990, pp. 267-277.
110. N. Claussen, K. L. Weisskopf and M. Ruhle, *J. Am. Ceram. Soc.*, 1986, vol. 69, pp. 288-92.
111. F. D. Gac and J. J. Petrovic, *J. Am. Ceram. Soc.*, 1985, vol. 68, pp. C-200-C-201.
112. A. G. Evans, *ASTM STP 907*, American Society for Testing and Materials, Philadelphia, 1989, pp. 267-291.
113. T. L. Jessen, J. J. Mecholsky and R. H. Moore, *Am. Ceram. Soc. Bull.*, 1986, vol. 65, pp. 377-381.
114. J. J. Mecholsky, T. L. Jessen and R. H. Moore, *Ceram. Eng. Sci. Proc.*, 1985, vol. 6, pp. 657-662.
115. L. Xiao and R. Abbaschian, *Mater. Sci. Eng.*, 1992, vol. A155, pp. 135-45.
116. H. C. Cao, B. J. Dagleish, H. Deve, C. Elliott, A. G. Evans, R. Mehrabian and G. R. Odette, *Acta Metall.*, 1989, vol. 37, pp. 2969-77.
117. H. E. Deve, A. G. Evans, G. R. Odette, R. Mehrabian, M. L. Emiliani and R. J. Hecht, *Acta Metall. Mater.*, 1990, vol. 38, pp. 1491-502.
118. T. C. Lu, A. G. Evans, R. J. Hecht and R. Mehrabian, *Acta Metall. Mater.*, 1991, vol. 39, pp. 1853-62.

119. L. Xiao and R. Abbaschian, in Advanced Metal Matrix Composites for Elevated Temperatures, edited by M. N. Gungor, E. J. Lavernia and S. G. Fishman, ASM International, Mater. Park, Ohio, 1991, pp. 33-40.
120. L. Xiao, in Developments in Ceramic and Metal-Matrix Composites, edited by K. Upadhyaya, A Publication of TMS, 1992, pp. 359-69.
121. L. Xiao, in Developments in Ceramic and Metal-Matrix Composites, edited by K. Upadhyaya, A Publication of TMS, 1992, pp. 115-24.
122. V. V. Krstic, P. S. Nicholson and R. G. Hoagland, *J. Am. Ceram. Soc.*, 1981, vol. 64, pp. 499-503.
123. L. S. Sigl and H. F. Fischmeister, *Acta Metall.*, 1988, vol. 36, pp. 887-97.
124. A. V. Virkar and D. L. Johnson, *J. Am. Ceram. Soc.*, 1977, vol. 60, pp. 514-19.
125. M. I. Mendelson and M. E. Fine, *J. Am. Ceram. Soc.*, 1974, vol. 57, pp. 154-59.
126. C. K. Elliot, G. R. Odette, G. E. Lucus and J. W. Scheckard, in High-Temperature/High-Performance Composites, edited by F. D. Lemkey, A. G. Evans, S. G. Fishman and J. R. Strife, MRS, Pittsburgh, Penn., 1988, pp. 95-102.
127. E. Fitzer, in Whisker- and Fiber-Toughened Ceramics, edited by R. A. Bradley, D. E. Clark, D. C. Larsen and J. O. Stiegler, ASM International TM, 1988, pp. 165-83.
128. P. Hing and G. W. Groves, *J. Mater. Sci.*, 1972, vol. 7, pp. 427-434.
129. R. W. Rice, *Ceram. Eng. Sci. Proc.*, 1981, vol. 2, pp. 661-701.
130. J. J. Mecholsky and Z. Chen, unpublished work.
131. D. Han and J. J. Mecholsky, *Mater. Sci. Eng.*, 1991, vol. A144, pp. 293-302.
132. H. Doty and R. Abbaschian, unpublished work.
133. K. T. Venkateswara Rao, G. R. Odette and R. O. Ritchie, *Acta Metall. Mater.* 1992, vol. 40, p. 353.
134. K. S. Ravichandran, *Scripta Metall. Mater.*, 1991, vol. 25, pp. 2645-2650.

135. K. S. Ravichandran, *Acta Metall. Mater.*, 1992, vol. 40, pp. 1009-1022.
136. B. N. Cox, *Acta Metall. Mater.*, 1991, vol. 39, pp. 1189-1201.
137. B. N. Cox and C. S. Lo, *Acta Metall. Mater.*, 1992, vol. 40, pp. 69-80.
138. B. N. Cox, D. B. Marshall and M. D. Thouless, *Acta Metall.*, 1989, vol. 37, pp. 1933-43.
139. A. B. Gokhale and G. J. Abbaschian, in *Binary Alloy Phase Diagrams*, edited by T. B. Massalski, Am. Soc. Metals, Metals Park, Ohio, 1986, p. 1631.
140. J. M. Yang, W. Kai and S. M. Jeng, *Scripta Metall.*, 1989, vol. 23, pp. 1953-8.
141. Y. Unakoshi, T. Hirano, T. Sakagami and T. Yamane, *Scripta Metall.*, 1989, vol. 23, pp. 87-90.
142. Y. Unakoshi, T. Sakagami, T. Hirano and T. Yamane, *Acta Metall. Mater.*, 1990, vol. 38, pp. 909-15.
143. P. J. Meschter, *Metall. Trans.*, 1992, vol. 23A, pp. 1763-1772.
144. R. W. Bartlett, J. W. McCamont and P. R. Gage, *J. Am. Ceram. Soc.*, 1965, vol. 48, pp. 551-8.
145. E. Fitzer and J. Schwab, *Metall.*, 1955, vol. 9, pp. 1062.
146. J. H. Westbrook and D. L. Wood, *J. Nucl. Mater.*, 1964, vol. 12, pp. 208-15.
147. D. E. Clark, W. J. Dalzell and D. C. Folz, *Ceram. Eng. Sci. Proc.*, 1988, vol. 9, pp. 1111-8.
148. B. E. Yoldas, *J. Mater. Sci.*, 1975, vol. 10, pp. 1856-60.
149. J. J. Lannutti, Master's Thesis, University of Florida, 1984.
150. R. M. Burns and W. W. Bradley, *Protective Coatings for Metals*, Reinhold Publishing Corporation, New York, 1955, pp. 556-65.
151. L. Xiao and R. Abbaschian, in *Advanced Metal Matrix Composites for Elevated Temperatures*, edited by M. N. Gungor, E. J. Lavernia and S. G. Fishman, ASM International, Ohio, 1991, pp. 21-31.

152. J. J. Mecholsky and L. M. Barker, in *Chevron-Notched Specimens: Testing and Stress Analysis*, ASTM STP 855, edited by J. H. Underwood, S. W. Freiman, and F. I. Baratta, ASTM, Philadelphia, Penn., 1984, pp. 324-36.
153. D. G. Munz, J. L. Shannon, Jr., and R. T. Busey, *Int. J. Fracture*, 1980, vol. 16, pp. R137-41.
154. J. C. Newman, Jr., in *Chevron-Notched Specimens: Testing and Stress Analysis*, ASTM STP 855, edited by J. H. Underwood, S. W. Freiman and F. I. Baratta, ASTM, Philadelphia, Penn., 1984, pp. 5-31.
155. L. M. Barker and F. I. Baratta, *J. Testing and Evaluation*, 1980, vol. 8, pp. 97-102.
156. D. Munz, *Eng. Fracture Mech.*, 1981, vol. 15, pp. 231-6.
157. J. L. Shannon, Jr. and D. G. Munz, in *Chevron-Notched Specimens: Testing and Stress Analysis*, ASTM STP 855, edited by J. H. Underwood, S. W. Freiman and F. I. Baratta, ASTM, Philadelphia, Penn., 1984, pp. 270-80.
158. J. D. Cotton, Y. S. Kim and M. J. Kaufman, *Mater. Sci. Eng.*, 1991, vol. A144, pp. 287-291.
159. J. P. A. Lofvander, J. Y. Yang, C. G. Levi and R. Mehrabian, in *Advanced Metal Matrix Composites for Elevated Temperatures*, edited by M. N. Gungor, E. J. Lavernia and S. G. Fishman, ASM International, Ohio, 1991, pp. 1-10.
160. S. Maloy, A. H. Heuer, J. Lewandowski and J. Petrovic, *J. Am. Ceram. Soc.*, 1991, vol. 74, pp. 2704-706.
161. R. B. Schwarz, D. R. Srinivasan, J. J. Petrovic and C. J. Maggiore, presented at the First High Temperature Structural Silicide Workshop, NIST, Gaithersburg, Md., November 4-6, 1991.
162. E. M. Savitsky, V. V. Baron and M. I. Bychkova, *Trudy Inst. Met. im. A. A. Baikova, Acad. Nauk. SSSR*, 1963, vol. 12, pp. 179-88.
163. E. M. Savitsky, V. V. Baron, M. I. Bychkova, S. A. Bakuta and E. I. Gladyshevskiy, *Russian Metallurgy*, 1965, vol. 2, p. 91.
164. T. C. Lu, Y. G. Deng, C. G. Levi and R. Mehrabian, in *Advanced Metal Matrix Composites for Elevated Temperatures*, edited by M. N. Gungor, E. J. Lavernia and S. G. Fishman, ASM International, Materials Park, Ohio, 1991, pp. 11-19.

165. H. Okamoto, A. B. Gokhale and R. Abbaschian, in *Binary Alloy Phase Diagrams*, edited by T. B. Massalski, ASM International, Materials Park, Ohio, 1990, p. 2767 and p. 1632.
166. I. Barin, O. Knacke and O. Kubaschewski, *Thermochemical Properties of Inorganic Substances*, Springer-Verlag, Berlin, Heidelberg, New York, 1977.
167. E. Fitzer and F. K. Schmidt, *High Temp. High Pressures*, 1971, vol. 3, pp. 445-460.
168. F. Roux and A. Vignes, *Rev. Phys. Appl.*, 1970, vol. 5, p. 393.
169. I. Barin, O. Knacke and O. Kubaschewski, *Thermodynamical Properties of Inorganic Substances*, Springer-Verlag, Berlin, Heidelberg, New York, 1977.
170. L. Xiao and R. Abbaschian, *Metall. Trans.*, 1992, vol. 23A, pp. 2863-72.
171. W. J. Dalzell, Master's Thesis, University of Florida, 1988.
172. *Metals Handbook*, vol. 2, 8th ed., ASM, Metals Park, Ohio, 1964, pp. 620-7.
173. G. C. Wood, in *Oxides and Oxide Films*, vol. 2, edited by J. W. Diggle, Marcek Dekker, Inc., New York, 1973, pp. 167-279.
174. W. H. Sutton and E. Feingold, *Mater. Sci. Res.*, 1966, vol. 3, p. 577.
175. C. T. Lynch and H. M. Burte, in *Metal Matrix Composites*, ASTM STP 438, Amer. Soc. Test. Mater., Philadelphia, Penn., 1968, pp. 3-25.
176. B. J. Dalgleish, K. P. Trumble and A. G. Evans, *Acta Metall.*, 1989, vol. 37, p. 1923.
177. J. Cook and J. E. Gordon, *Proc. Royal Soc. A*, 1964, vol. 282, pp. 508-20.
178. J. I. Bluhm, *Eng. Fracture Mech.*, 1975, vol. 7, pp. 593-604.
179. T. T. Shih, *J. Testing and Evaluation*, 1981, vol. 9, pp. 50-5.
180. F. C. Lea, *Hardness of Metals*, Charles Griffin and Company, Ltd, London, 1936, pp. 91-105.
181. *Metals Handbook*, vol. 1, 8th ed., ASM, Metals Park, Ohio, 1966.
182. E. G. Thomsen, C. T. Yang and S. Kobayashi, *Mechanics of Plastic Deformation in Metal Processing*, The Macmillan Company, New York, 1965.

183. P. W. Bridgman, Studies in Large Plastic Flow and Fracture, 1st ed., McGraw-Hill Book Comp., Inc., New York, NY, 1952.
184. E. G. Thomsen, C. T. Yang and S. Kobayashi, Mechanics of Plastic Deformation in Metal Processing, The Macmillan Company, New York, 1965.
185. G. E. Dieter, Jr., Mechanical Metallurgy, McGraw-Hill Kogakusha, Ltd., Tokyo, 1961.
186. H. G. Tattersall and G. Tappin, J. Mater. Sci., 1966, vol.1, pp. 296-301.
187. L. I. Sedov, A Course in Continuum Mechanics, vol. 4, Volters-Noordhoff, Groningen, 1972.
188. H. M. Westergaard, J. Appl. Mech., 1939, vol. 61, p. A-39.
189. B. N. Cox, D. B. Marshall and M. D. Thouless, Acta Metall., 1989, vol. 37, pp. 1933-43.

BIOGRAPHICAL SKETCH

Lingang Xiao finished his college education at Fuzhou University, China, in 1980. After that he worked as a research assistant for two years, and then became a lecturer teaching the courses of physical metallurgy, technology of heat treatment, and metallurgical engineering at the same university until 1988. Beginning from 1983 he also enrolled as a part-time graduate student, and obtained his M. Eng. degree in mechanical engineering in 1987. He published seven papers related to the work conducted in pursuing his M. Eng. degree.

He joined the Department of Materials Science and Engineering, University of Florida, in 1989. Within four years at the University of Florida, under the guidance of Dr. R. Abbaschian he obtained an M.S. degree and a Ph.D. degree in materials science and engineering with a minor in mechanics and engineering science; achieved a high GPA (3.87 for major and 4.00 for minor); published 14 papers and had 11 presentations; and finally won the 1992 ASM International Graduate Student Paper Contest.

I certify that I have read this study and that in my opinion it conforms to acceptable standards of scholarly presentation and is fully adequate, in scope and quality, as a dissertation for the degree of Doctor of Philosophy.



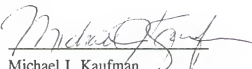
Reza Abbaschian, Chairman
Professor of Materials Science
and Engineering

I certify that I have read this study and that in my opinion it conforms to acceptable standards of scholarly presentation and is fully adequate, in scope and quality, as a dissertation for the degree of Doctor of Philosophy.



Robert T. DeHoff
Professor of Materials Science
and Engineering

I certify that I have read this study and that in my opinion it conforms to acceptable standards of scholarly presentation and is fully adequate, in scope and quality, as a dissertation for the degree of Doctor of Philosophy.



Michael J. Kaufman
Associate Professor of Materials
Science and Engineering

I certify that I have read this study and that in my opinion it conforms to acceptable standards of scholarly presentation and is fully adequate, in scope and quality, as a dissertation for the degree of Doctor of Philosophy.



Jack J. Mecholsky
Professor of Materials Science
and Engineering

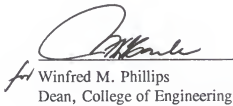
I certify that I have read this study and that in my opinion it conforms to acceptable standards of scholarly presentation and is fully adequate, in scope and quality, as a dissertation for the degree of Doctor of Philosophy.



Bhavani. V. Sankar
Associate Professor of Aerospace,
Mechanics, and Engineering
Science

This dissertation was submitted to the Graduate Faculty of the College of Engineering and to the Graduate School and was accepted as partial fulfillment of the requirements for the degree of Doctor of Philosophy.

December 1992



Winfred M. Phillips
Dean, College of Engineering

Madelyn M. Lockhart
Dean, Graduate School